MINISTRY OF EDUCATION, RESEARCH, YOUTH AND SPORT

THE ANNALS OF "DUNAREA DE JOS" UNIVERSITY OF GALATI

Fascicle IX
METALLURGY AND MATERIALS SCIENCE

YEAR XXX (XXXV),
December 2012, no.4

ISSN 1453-083X

2012
GALATI UNIVERSITY PRESS

Table of Content

THE ANNALS OF "DUNAREA DE JOS" UNIVERSITY OF GALATI.
FASCICLE IX. METALLURGY AND MATERIALS SCIENCE
N^0. 4 – 2012, ISSN 1453 – 083X

THE BEHAVIOR OF REFRACTORY IN INTERACTION WITH METALLURGICAL SLAG

Florentina POTECAŞU[1], Marcela MUNTEAN[2], Mariana IVAN[3]
[1]Faculty of Metallurgy and Material Science, "Dunărea de Jos" University of Galaţi
[2]Politehnica Bucharest University, Bucharest
[3]ArcelorMittal Galaţi
email: mihaela_potecasu@yahoo.com

ABSTRACT

The aim of this paper is to present the studies concerning the refractory behavior to metallurgical slag corrosion. The corrosion resistance at high temperatures using the static method on samples containing chamotte respectively, alumina were performed. The corrosion degree of refractory plastics mass was done by corrosion determination, the corrosion rate and macroscopic image analysis measurements. The analysis of samples subjected to macroscopic measurements showed better behavior in terms of corrosion resistance for alumina samples.

KEYWORDS: refractory plastic mass, cast iron, slag, chemical corrosion

1. Introduction

The most requested parts in direct contact with the cast iron and metallurgical slag is the tape hole of the furnace and cast iron gutters to transport its cast iron ladles. The maintenance and correct operation of tap hole cast iron has a great importance for the normal operation of the furnace in complete safety. It is necessary that the amount of plastic used to seal the outlet to provide, besides a good seal also a wear protective of carbon mass of the crucible and the tap hole. A measure for assessing the refractory plastic masses behavior during utilisation is the chemical corrosion resistance. A mass with high chemical corrosion resistance protects the surrounding area but also provide a corresponding flow to technology.

The corrosion resistance, in this case is considered the property of refractory products do not degrade under chemical action of the cast iron and slag. The corrosion intensity of refractory lining depends on the chemical nature of the refractory material and corrosive material that reacts with the first. An important role have the temperature, which enhances the corrosion process.

The chemical etching of the refractory by the cast iron or steel occurs after a solid-liquid reaction, quite slow and less important than the reaction of the refractory with slag. For this reason, the studies are directed, particularly, to the system slag - refractory material. There are many studies on chemical corrosion of refractories.

In the following will be presented a few examples of the corrosion process, which refers to the refractories Al2O3-SiC-C systems.

1.1. A review of the corrosion mechanism study

The study of refractory etching by slag is one of particular importance [1]. The refractory resistance could be more weakened by the dissolving action in liquid slag. The slag etching on refractory in contact can occur in two ways:

- corrosion - refractory wear and tear caused by chemical etching of slag;
- erosion - caused by mechanical action, namely detachment and involvement of the slag material by the slag refractory material [1].

The slag infiltration and metal in refractory grains, mechanical erosion caused by moving liquid slag and the slag chemical etching, all that contribute to loss of the refractory masonry [2].

The chemical corrosion can be defined, as is known [3] that refractory wear by mass loss, ie the thickness of refractories exposed as a result of chemical etching by a corrosive liquid. The refractory and liquid will react at the interface, reaching chemical equilibrium in the contact area between the refractory and corrosive liquid.

With the chemical reactions during corrosion, physical changes occur that could accelerate the corrosion process. The corrosion is the refractory

wear by the loss of thickness and mass of the exposed refractory due to chemical etching by the melt, in a process where refractory and melt react, chemically balanced in the contact zone between the refractory and melt.

This is a key point because the corrosion reactions continues until it reaches a steady state.

For the corrosion analysis and to anticipate the chemical strategies to reduce the corrosion and wear rate, some authors [3] propose us of phase equilibrium diagrams. In this context there are two possible approaches: the first is to see the corrosion asa a chemical and physical process without detailed application of equilibrium phase diagrams, called "phenomenological approach" and the second approach involves using information from the phenomenological approach and to use phase equilibrium diagrams. This last option is necessary for a full understanding of refractory corrosion [3].

Juergen Pötschke and Thomas Deinet think the refractories in contact with molten slag and steel shows a wide variation of behavior in terms of corrosion resistance. The corrosion is based on the Marangoni convection.

References provides details on this topic [4]. The diffusion process and controlled chemical reactions between the three phases - slag, refractory and steel - lead to a concentration gradient affecting the interfacial free energy of steel and slag, minimization of them.

This causes a strong flow transmitted by convection from the boundary between phases, which causes a significant reduction and improvement layer diffusion and mass transfer. A model was developed to predict the corrosion rate.

This paper presents a contribution to understanding the experiments and their quantitative expression. As a first approximation, the corrosion rate in mm/h can be estimated by the difference between the refractory and slag saturated concentration and the initial composition, regardless slag type and steel composition. These studies can develop depending on the slag composition of steel and steel mills specific conditions [5].

Local corrosion was studied on alumina-graphite refractory interface and slag by immersion tests and direct observation technique using high temperature X-ray. Combining these investigations with microscopic studies, it was developed a mechanism for local corrosion.

The mechanism is based on cyclic dissolution of alumina and graphite in slag, respectively molten metal phases. It was found that during the dissolution of refractory with alumina slag film movement induced Marangoni effect and the evolution of gas bubbles can accelerate the dissolution process [6].

William Smothers and A.R. Cooper studied the situations when is mutual penetration of two interacting phases (refractory material and liquid slag) beyond the border pan, in the adjacent plan [9]. They have revealed that dissolution of solid phase in a liquid phase (slag in the present situation), decreases the rate of diffusion through the liquid phase to exceed the solubility limit in oxide components of the refractory material.

The corrosion occurs due to heterogeneous chemical reactions between liquid phases (slags and other melts) and refractories. The reaction products can be in one of the following situations: to move, in generally, in the slag or melt, to form new compounds to diffuse into the surface lining or refractory lining [9].

2. Materials and methods

The corrosion resistance study at high temperatures using the static method (STAS 5193/1-83) on a set of samples containing alumina or chamotte were analyzed. To evaluate the corrosion degree of refractory plastics mass, the corrosion coefficient, the corrosion rate and macroscopic image analysis measurements of samples were done.

Two types of refractory masses, noted A and B were subjected to analysis The proportion of raw materials, the chemical – oxide composition and physico-mechanical properties of the samples are presented in Tables 1 and 2.

Table 1. *Raw materials composition*

Material used	Material quantity [%]	
	A	B
Sand	25.0	-
Fire clay	15.0	-
Alumina	-	39.5
Reactive alumina	-	0.5
Clay	30.0	30.0
Coke breeze	10.0	10.0
Graphite	10.0	10.0
Silicon carbide	10.0	10.0
Phosphoric acid	27.65	27.65
Novolac	2.9	2.9
Hexamethylen tetramine	0.9	0.9
Tehnocell	1.0	1.0
Meraklon	0.5	0.5
Ceramic fiber	-	1.0

In Tables 3 and 4 are presented the variation limits of the chemical composition for blast furnace slag and cast iron analyzed.

Table 2. *Chemical and oxide composition, physical and mechanical properties*

Experimental masses	Composition					Physical and mechanical properties		
	SiO_2	Al_2O_3	SiC	C	Fe_2O_3	Apparent density	Apparent porosity	Compressive strength
	[%]					[g/cm^3]	[%]	[N/mm^2]
A	48.28	17.22	9.30	17.41	1.26	2.03	28	12
B	19.50	47.95	9.30	17.41	0.86	2.36	20	16

Table 3. *The chemical composition for blast furnace slag, [%]*

CaO	SiO_2	Al_2O_3	MgO	MnO	FeO
43 ÷ 44	34.1 ÷ 35	12.5 ÷ 13.5	5.86 ÷ 6.26	0.66 ÷ 1.49	0.54 ÷ 0.66

Table 4. *The chemical composition for cast iron, [%]*

C	Mn	Si	S	P
3.90	0.4 ÷ 0.7	0.4 ÷ 0.7	> 0.003	0.08÷ 0.10

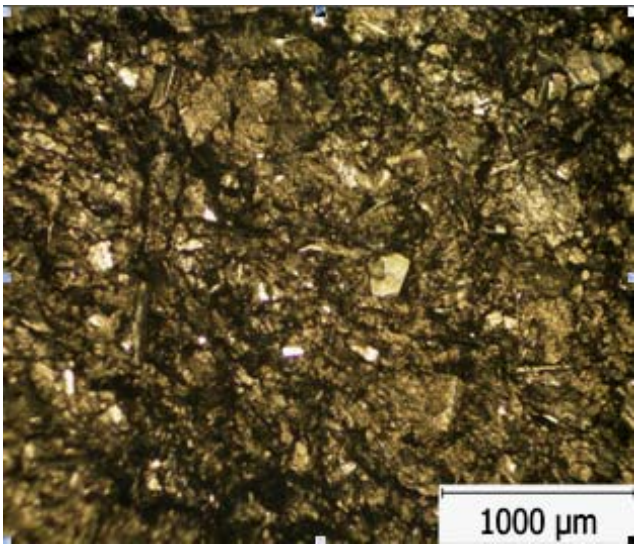

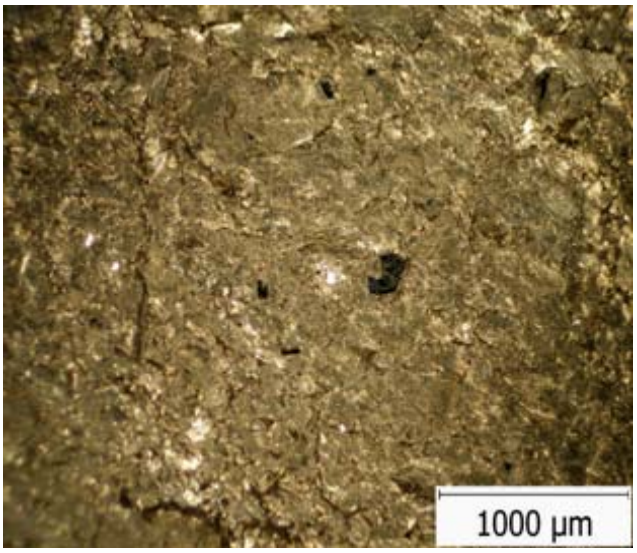

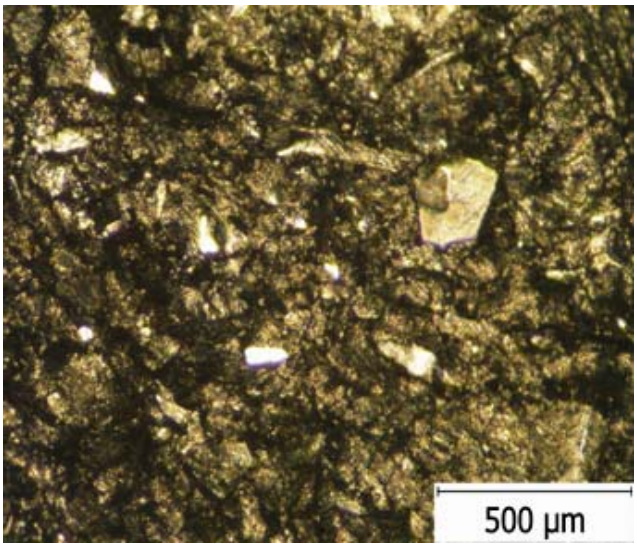

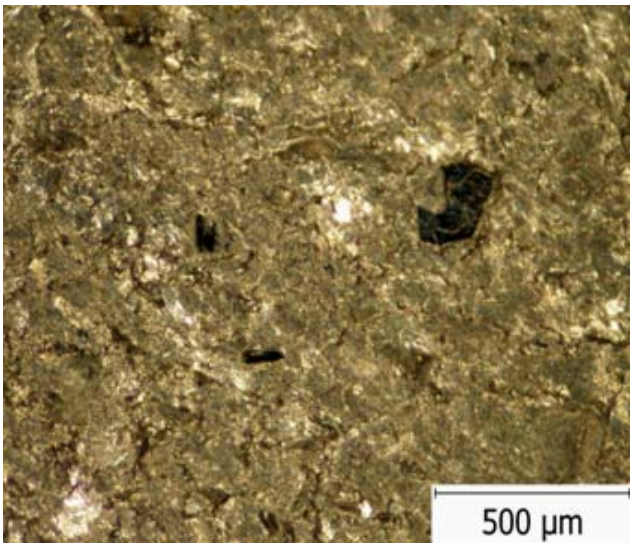

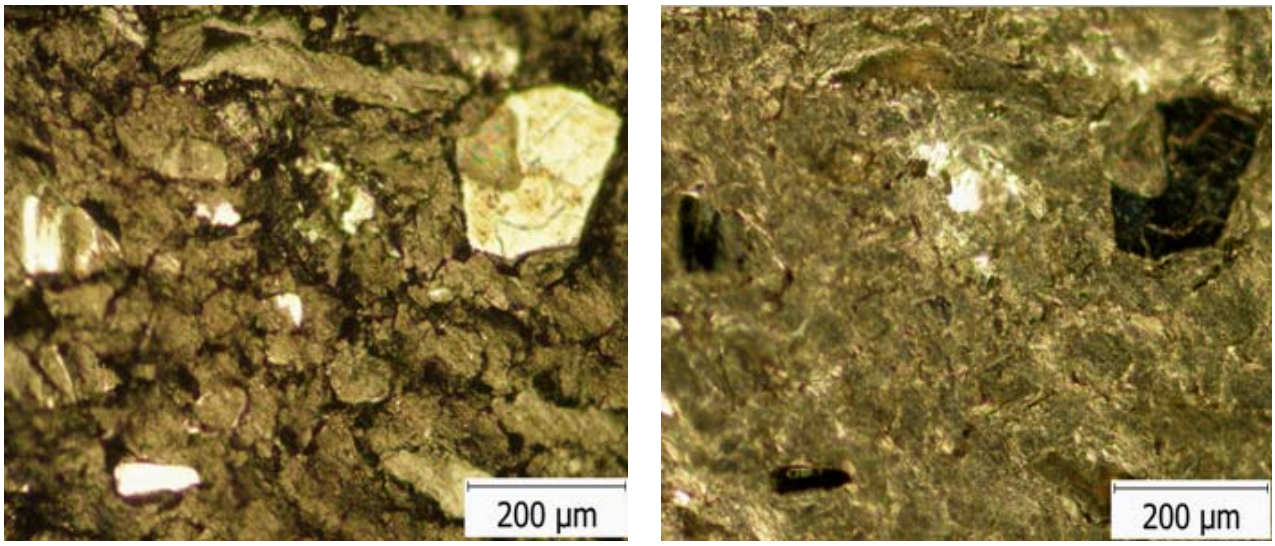

a b

Fig. 1. *The optical micrographs of sample A for polished surface in bright field (a) and dark field (b) at various magnifications*

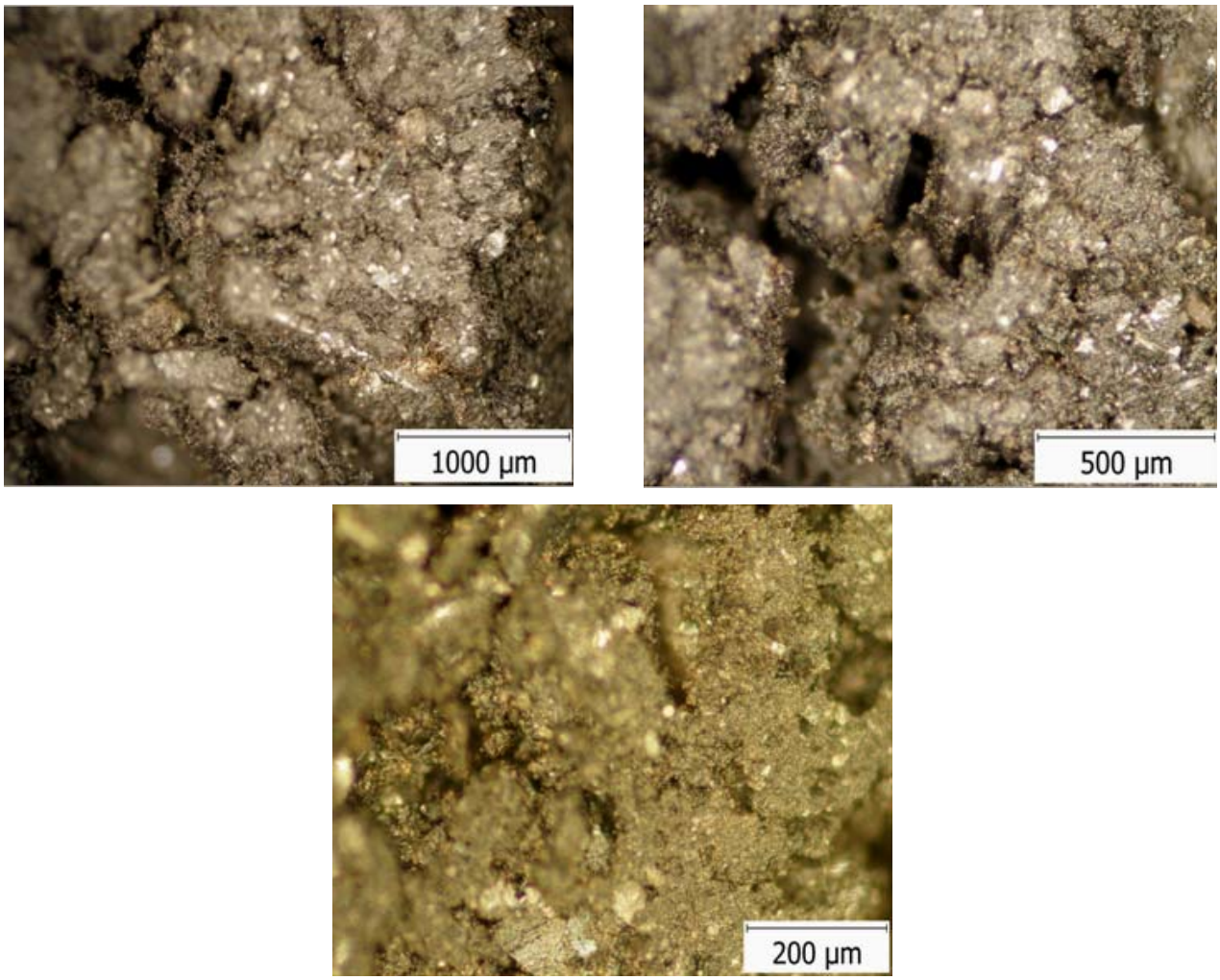

Fig. 2. *The optical micrographs of sample A for breaking surface in dark field at various magnifications*

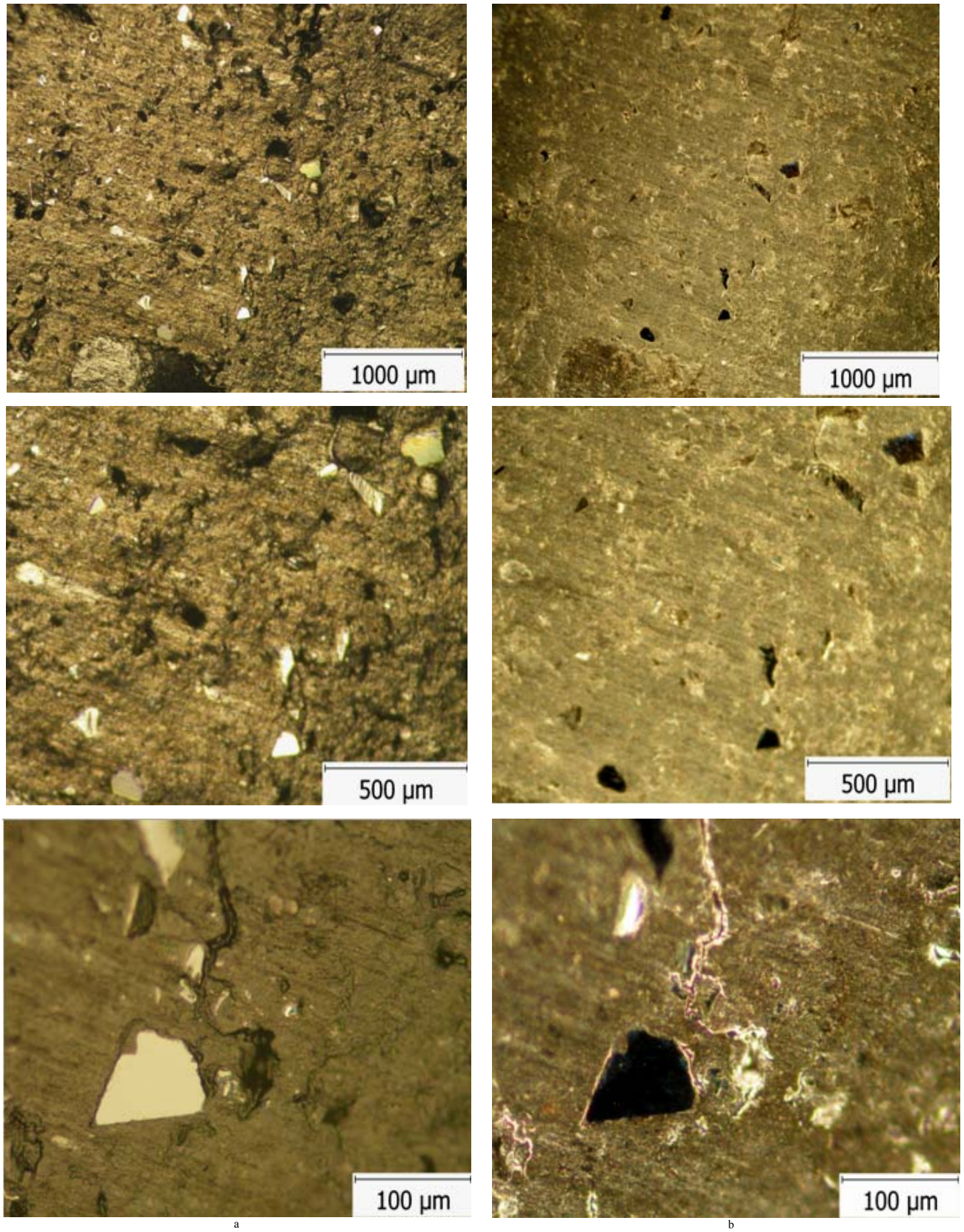

a b

Fig. 3. *The optical micrographs of sample B for polished surface in bright field (a) and dark field (b) at various magnifications*

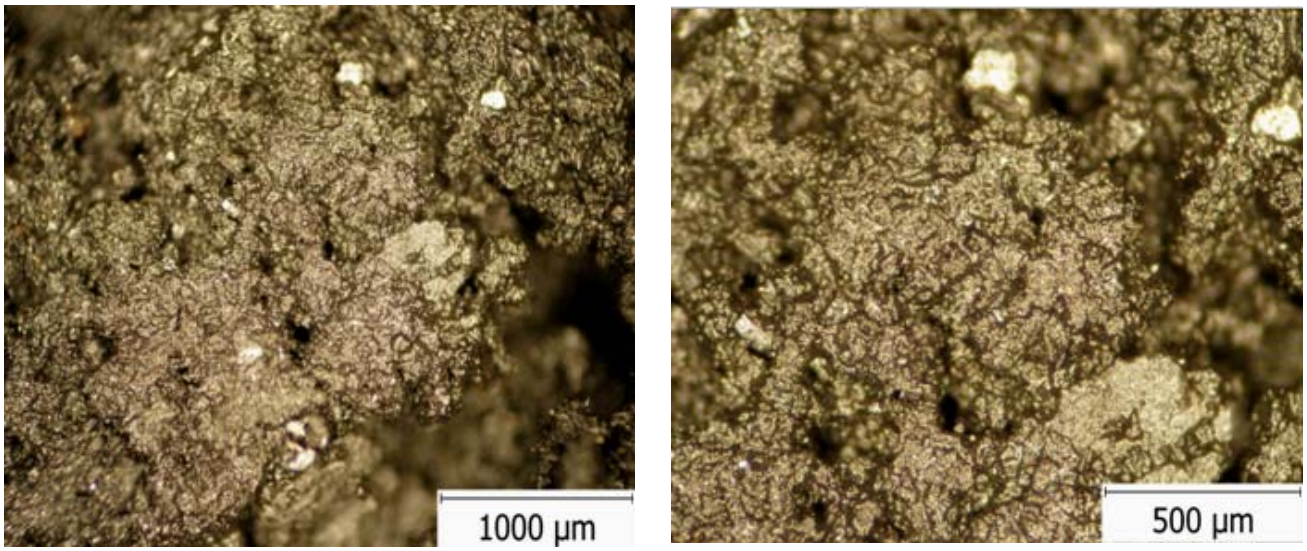

Fig. 4. *The optical micrographs of sample B for breaking surface in dark field at various magnifications*

In Figures 5, 6, 7, 8 are presented the specimens appearance after the corrosion measurements.

Fig. 5. *Fire-clay containing sample, subjected to the action of iron* ***(A1)***

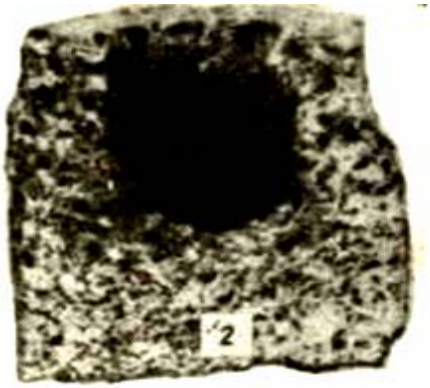

Fig. 6. *Alumina -containing sample, subjected to the action of iron* ***(B2)***

Fig. 7. *Fire-clay containing sample, subjected to the action of slag* ***(A3)***

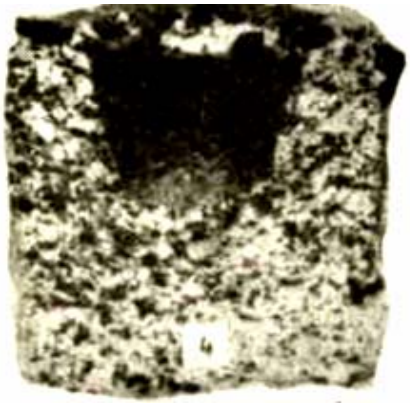

Fig. 8. *Alumina -containing sample, subjected to the action of slag* ***(B4)***

Table 5. *Texture description of samples*

Sample	Basic materials	Homogeneity	Compactness	Grain size	Grain distribution
A	Chamotte, quarz, silicon carbide	homogeneous	porous	coarse	iregular
B	bauxite, quartz, silicon carbide	homogeneous	compact	fine	uniform

The four sets of samples were tested: two corresponding to the mass composition A and two corresponding to mass composition B. The corrosion measurements are summarized in Table 6.

Table 6. *The corrosion measurements for analyzed samples*

Sample	The main component	Corrosive factor
A1	chamotte	iron
B2	alumina	iron
A3	chamotte	slag
B4	alumina	slag

3. Results and discussion

The corrosion degree of refractory plastics mass was done by determining:

1) corrosion coefficient, I [%];
2) corrosion rate, Vc [mm/s].
3) macroscopic image analysis

The resulting values from the determinations are summarized in Tables 7 and 8. In Figures 5, 6, 7, 8 in samples with cast iron (A1 and B2) it was found that samples having the chamotte refractory as aggregate it were deformed, while those who had used high purity alumina remained undistorted (Figures 5, 6).

Table 7. *The corrosion coefficient of analyzed samples*

Sample	Initial surface, S_o	Final surface, S_f	Final diameter, D_{if}	Coefficient α	Initial volume, V_o	Final volume, V_f	Corrosion coefficient, I
	[mm^2]		[mm]		[mm^3]		[%]
A1	600	704	34	1.20	14130.00	30294.72	214.40
B2	600	651	32	1.20	14130.00	28297.68	200.27
A3	600	1092	44	1.30	14130.00	50227.44	355.47
B4	600	651	32	1.20	14130.00	28297.68	200.27

Table 8. *The corrosion rate of analyzed samples*

Sample	Initial radius, R_o	Final radius, R_f	Time keeping, T_c	Corrosion rate, V_c
	[mm]		[s]	[mm/s]
A1	15	17	7200	27.78×10^{-3}
B2	15	16	7200	13.89×10^{-3}
A3	15	22	7200	97.22×10^{-3}
B4	15	16	7200	13.89×10^{-3}

In the structure of alumina samples (Fig. 6 and 8) can distinguish two zones: one impregnated with slag and an area unchanged. The impregnated area, with thickness up to 1 mm grain consists of slightly glazed with iron and silicon carbide crystals unchanged diffused in glazed mass, mixed with metal droplets. The unimpregnated area consists of large portions (about 2 mm diameter) of glassy appearance and black crystals with sharp angles of silicon carbide. Samples with chamotte, after slag etching resistance (Fig. 5 and 7) were deformed, if the sample containing slag, there are three areas (Fig. 5):

- *working area*, with up to 6 mm thickness is coated with slag;

- *the least modified area* of about 1.2 mm thickness is brighter than working area, but mass was melted and compacted;

- *unchanged area* is loose, opaque and fragile.

The sample containing alumina is instead much less etched by slag (Fig. 8). The silicon carbide refractory mass does not change during heat treatment.

4. Conclusions

Following the corrosion measurements and the corrosion degree of refractory plastics mass it was found that:

⇨ Cast iron action on the refractory material is less intense than slag action. Replacing of chamotte in the mass composition with alumina increased the corrosion resistance of refractory mass at slag corrosion.

⇨ The alumina sample in composition (noted B) resulted in a smaller corrosion coefficient and corrosion rate is lower than the chamotte sample composition (noted A).

⇨ The analysis of samples subjected to macroscopic measurements showed better behavior in terms of corrosion resistance for alumina samples.

⇨ The results from tests of corrosion measurements are related to chemical and mineralogical composition, texture and compactness, sample B has a homogeneous structure with uniform grain distribution and more compact than sample A, having strengths higher corrosion than sample A

⇨ The alumina sample in composition (noted B) is better as chemical stability, resulting corrosion coefficient values lower and corrosion rate is lower than the chamotte sample (noted A). This conclusion is confirmed by the macrostructural analysis performed in the the fracture surface. It can appreciate that in the set B, the alumina particles are in higher percentage amount, finely dispersed and were physical barriers to crack propagation. This led to the dispersion hardening phase samples (a significant increase in compressive strength) and on the other side have block the sample degradation by delaying the formation of a network of cracks intercomunicante.

References

[1]. Joardar A. - *Refractory lining, Steel Industry, Slag corrosion (Slag attack)*, Test of Refractory, June, 25, (2009).

[2]. Stubbles J. - *Steel Industry Consultant, The basic Oxigen Steelmaking (BOS) Process*, American Iron and Steel Institute, (2012).

[3]. Brosnan D. A. - *Corrosion of Refractories*, Refractories Handbook edited by Charles A, Schacht, Marcel Dekker, New York, NY 10016, Clemson University.

[4]. Deinet T., Pötschke J. - *Corrosion of AMC Bric*ks, Proc. 44th Int. Coll. on Refractories, 26/27 Sept., (2001), Aachen.

[5]. Pötschke J., Deinet T., Routschka G., Simmat R. - *Properties and Corrosion of AMC-Refractories, Part II: Corrosion by Steel/Slag. Proc*. UNITECR'03, Cancun, Mexico (2003) S. pp 84–87.

[6]. Pötschke J., Deinet T. - *The Wear of Refractories by Steel/Slag*. Proc. UNITECR'05, Orlando, USA, (2005).

[7]. Pötschke J., Deinet T. - *Premature corrosion of refractories by steel and slag*, Steelmaking, Millenium Steel, (2005).

[8]. Mukai K., Toguri J., Yoshitomi - *Corrosion of Alumina–Grafite Refractories at the Slag - Metal Interface*, Canadian Metallurgical Quaterly, no. 4, October/december, (1986), pp. 265-275 (11).

[9]. Smothers W., Cooper A. R. - *Kinetics of Refractory Corrosion,* The American Ceramic Society, (1981), Published Online, (2008).

[10]. Ivan M., Muntean M., Potecaşu F. - *Special Refractory masses for aplication in the iron and steel making area*, Revista Română de Materiale / Romanian Journal of Materials, (2012), 42 (1), 46 – 53.

[11]. Ivan M. - *Utilizarea produselor refractare în siderurgie*, Editura Standardizarea, Bucureşti, (2009), pp. 252 -253.

THE ANNALS OF "DUNAREA DE JOS" UNIVERSITY OF GALATI.
FASCICLE IX. METALLURGY AND MATERIALS SCIENCE
N^0. 4 – 2012, ISSN 1453 – 083X

AN ISOTHERMAL MODEL FOR EVALUATING STRESS AND STRAIN IN THE POLYMERIC BLOCK OF THE BLOCK-ON-RING SYSTEM

Constantin GEORGESCU[1], Doina BOAZU[2], Ioan ŞTEFĂNESCU[1], Lorena DELEANU[1]
[1]Machine Design and Graphics Department, "Dunarea de Jos" University of Galati
[2]Faculty of Mechanical Engineering, "Dunarea de Jos" University of Galati
email: constantin.georgescu@ugal.ro

ABSTRACT

This paper presents results of simulating an isothermal frictional contact between a polymeric block and a steel ring. The model takes into account the elasto-plastic behavior of the polymeric materials and the friction coefficient of the two triboelements in dry regime as determined from tests done on a block-on-ring system. The results given by the model are compared to some characteristics of the actual test ring (geometry of the wear track). The mechanical characteristic of the polymer material were modeled in accordance to the results obtained from the traction tests.

KEYWORDS: isothermal model, friction, stress and strain distribution, block-on-ring tester

1. Introduction

Finite element models have been successfully used to analyze contacts, but this takes a considerable amount of time and a high computational cost [2]. Some of these techniques yield closed-form solutions, which generally involve some simplifying assumptions. Many of them are limited to a certain range of geometries or loading conditions. Special two and three - dimensional elements have been developed for stress and displacement analyses in tribological contacts [4, 5, 12, 13, 14].

Wear and friction, introduced as supplementary processes in the contact models, make the model closer to the actual one as friction modify the stress and strain values [1, 6-9, 10, 11].

2. The fem model of the bloc-on-ring system with friction

In order to evaluate the contact in this particular problem of block-on-ring contact with friction, the authors used the program COSMOS/M version 2.9 [16].

The aim of this paper is to point out the behavior of polybuthylene therephthalate (PBT) in a contact with friction and to evaluate the stress and strain fields for different contact loads.

The hypotheses characterizing this model are:

- the material loss due to wear process is not taken into account. This is a first step in modeling the contact and the hypothesis is good enough for a starting analysis as the authors did tests on a performant tribometer and the wear parameter have low values as compared to, for instance, test done with blocks made of PTFE [3, 4];
- the model is isothermal (the temperature is kept constant at 20°C for the ring and the block);
- the material ring is hardened steel (elastic behavior) and could be considered rigid as compared to the block material (polymer);
- the block and ring materials are considered homogeneous and isotropic;
- the mechanical properties of the steel ring have been selected from the program library for a steel with the hardness close to that of the rings and for PBT, there were selected representative points from the experimentally obtained strain-stress curve, using the equipment TESTOMETRIC M350-5AT [17], having a force cell of 5 kN, as recommended by EN ISO 527-2, in the Laboratory of Polymeric Materials Research (Faculty of Mechanical Engineering, "Dunarea de Jos" University of Galati).

The elements that have been used in this simulation, were:

- the modeling of the block was done with the help of elements PLANE2D plane stress, with 4 nodes having a side of 0.1 mm (thus, the block model contains 5,050 elements); the block width is 4 mm;

- the ring modeling used rigid elements type BEAM2D with 2 nodes, the ring width is 10 mm;
- the contact modeling between the block and the ring used contact elements type GAP, node to line with automatically generated friction and the value of the friction coefficient is set here at 0.2 as determined from experimental tests.
- the values for the mechanical properties were determined from tensile tests done on bone samples made of PBT and Poisson coefficient was set at ν = 0.4) as given in literature [15].

The FEM model is presented in Fig. 1.

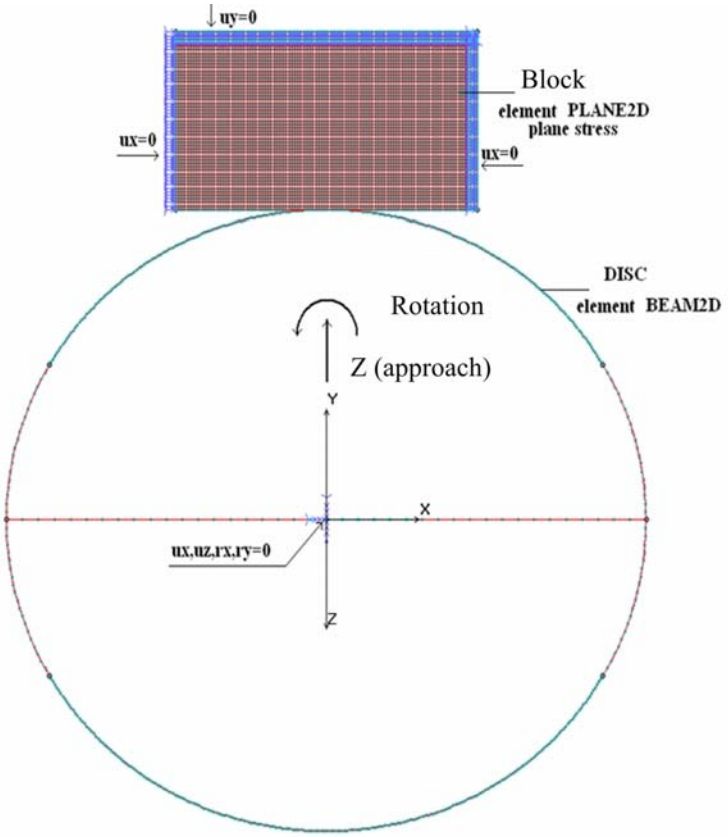

Fig. 1. *The model for the block-on-ring system*

The calculation was done cvasi-statically (the friction coefficient being considered independent on the sliding speed.

The materials' models:

- non-linear elasto-plastic model (von Mises isotropic) and it was used the information from the strain-stress curve experimentally determined for PBT;
- linear model for the ring material BEAM2D (hardened steel).

This contact model is a non-linear one, even if the structure has small deformations. The equilibrium is attended by incremental increase of the normal force, imposing the displacement on the force direction.

In order to solve the contact problem, it was used the method Newton-Raphson; generally, there are needed 6...7 iterations on each step for getting a convergence with the help of this method [2, 5].

In order to get the contact points and the stresses in this zone, the method of Total Lagrangian was used (the plastic deformations are small). The incremental values is automatically set, activating the clause "autostep". The cases taken into discussion in this paper are given in Table 1. The values of the contact width on the PBT blocks were obtained by measuring at room temperature (20...22°C).

3. Results and discussions

Analyzing the values in Table 1, one may notice that the results obtained from FEM modeling are in good agreement with those experimentally determined.

Figures 2...7 present the stress distributions for the following stresses: von Mises, main stresses σ_1 and σ_2, shear stress in plane xy and the strain distributions for the cases of F=5 N and F=20 N.

Table 1

Case	F	Imposed displacement of the block, Z	Calculated width of the contact	Measured width of the wear track (experimentally)
	[N]	[mm]		
1	1	0.0341	1.5	1.6
2	2,5	0.0151	1.79	1.3
3	5	0.0185	2.12	2.1
4	10	0.0539	2.94	2.8
5	20	0.1108	3.43	3.5

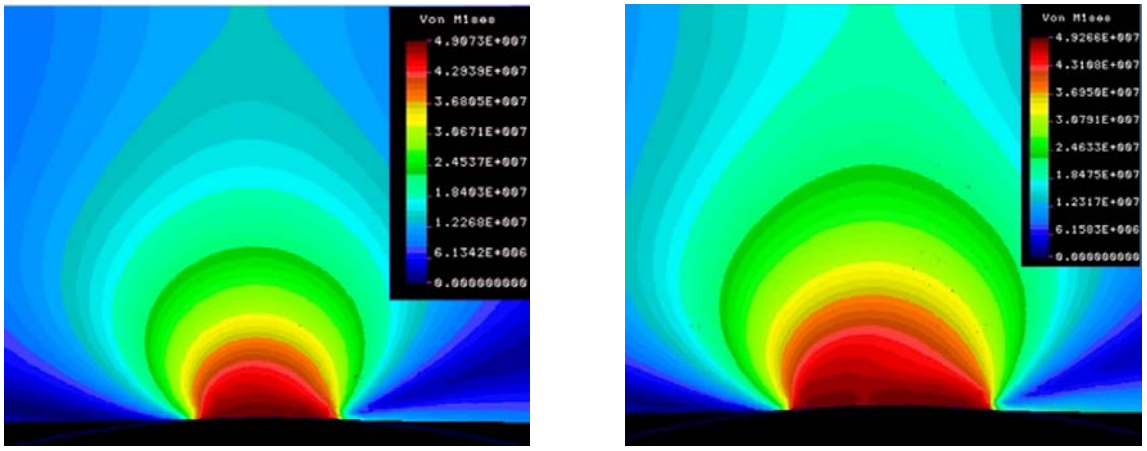

a) F = 5 N c) F = 20 N

Fig. 2. *The influence of the normally applied load on the distribution of von Mises stresses*

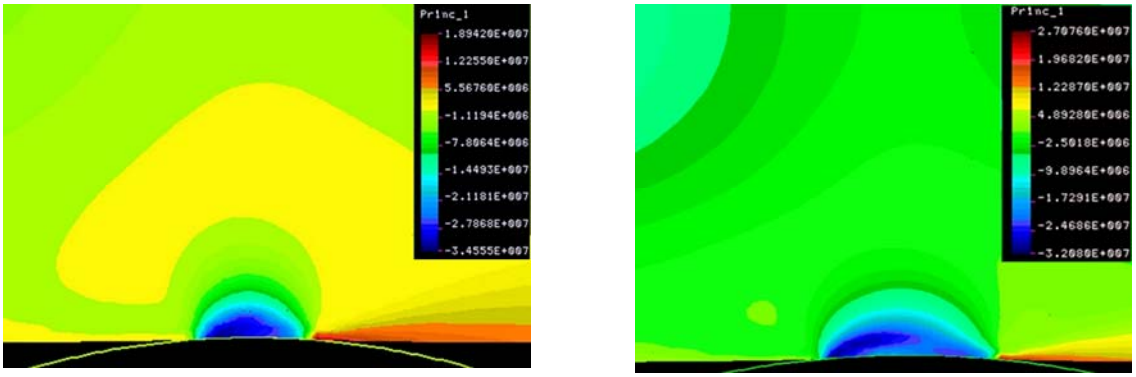

a) F = 5 N c) F = 20 N

Fig. 3. *The influence of the applied load on the main stress 1 (σ_1)*

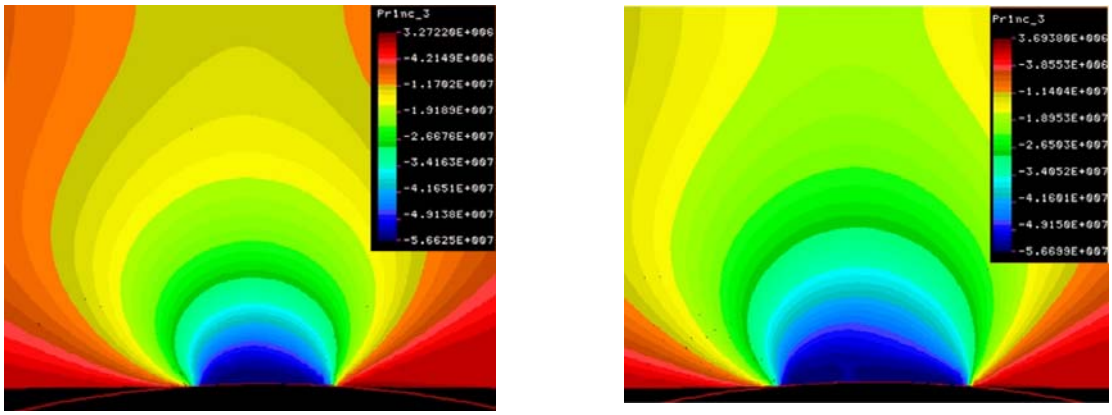

a) F = 5 N c) F = 20 N

Fig. 4. *The influence of the applied load on the distribution of the main stress 3 (σ_3)*

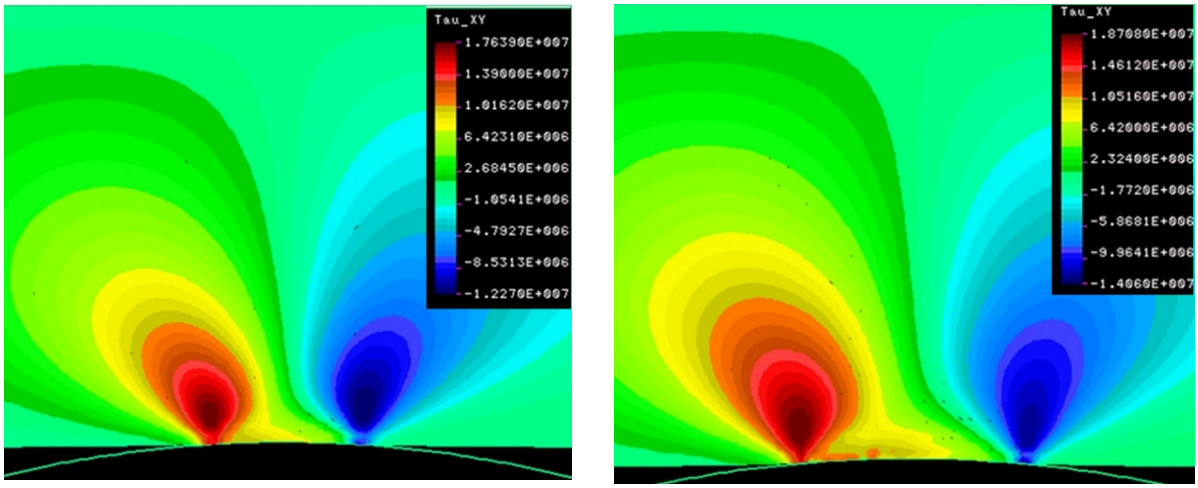

a) F = 5 N c) F = 20 N

Fig. 5. *The influence of the applied load on the shear stress (τ_{xy})*

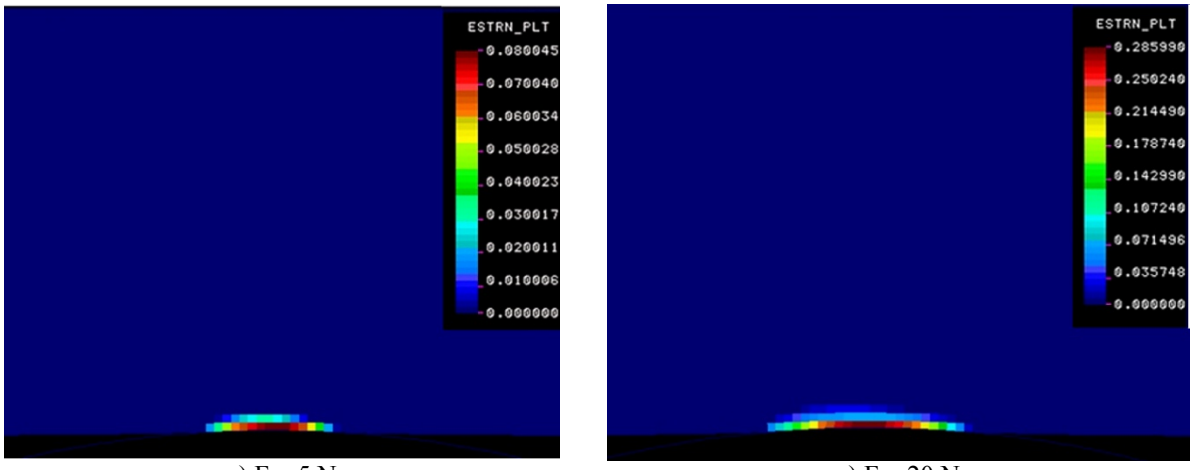

a) F = 5 N c) F = 20 N

Fig. 6. *The influence of the applied load on the total plastic strain distribution*

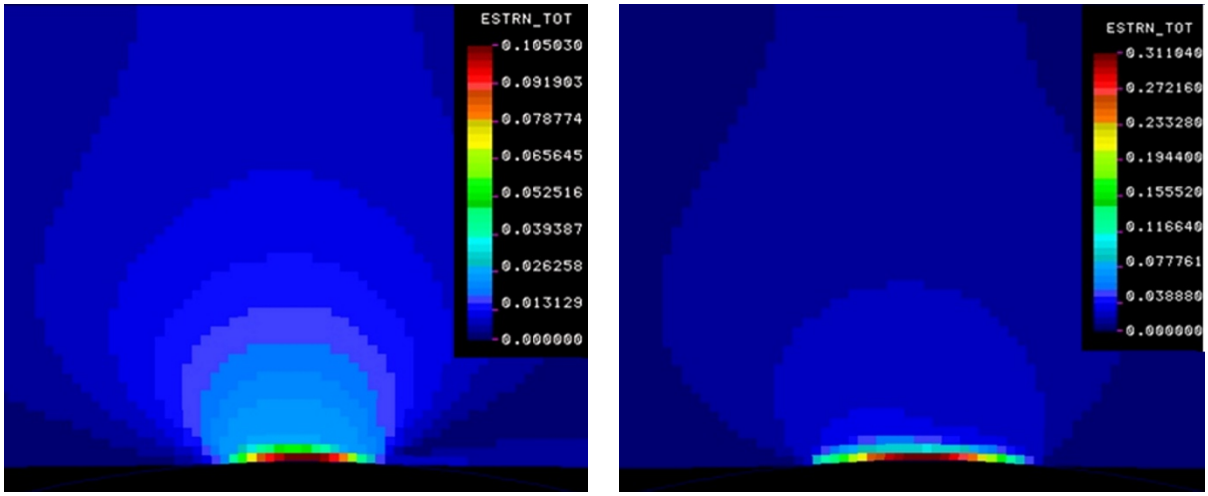

a) F = 5 N c) F = 20 N

Fig. 7*. The influence of the applied load on the distribution of the total deformation*

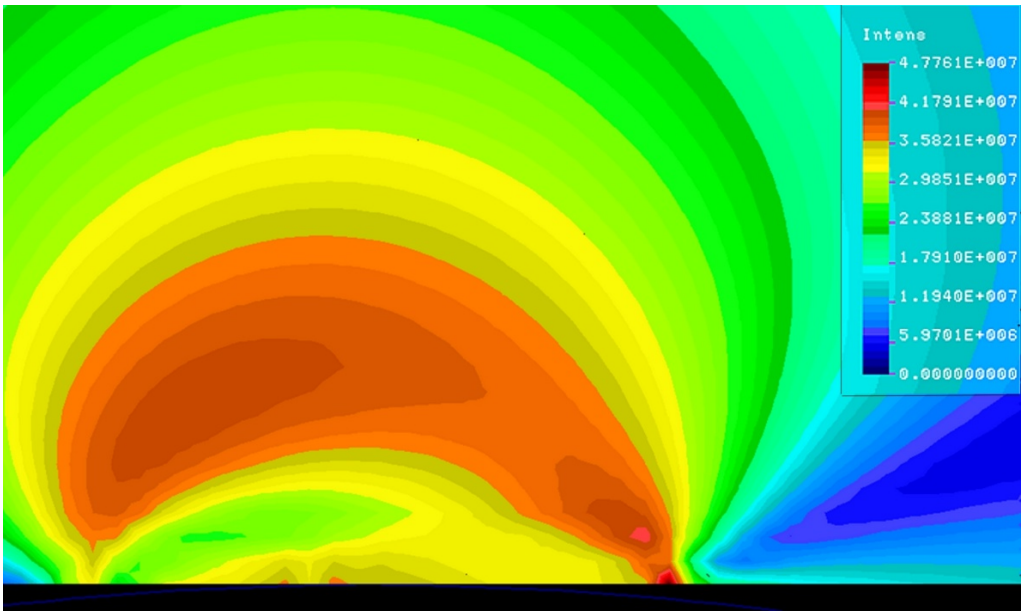

Fig. 10. *The distribution of the values for the parameter STRESS INTENSITY (the difference between the maximum main stress and the minimum main stress, σ_1-σ_3)*

Figure 8 gives maximum values of von Mises stresses characterizing the block made of PBT as a function of normally applied load. One may notice that von Mises stress asymptotically approaches the yield limit experimentally established for the polymer.

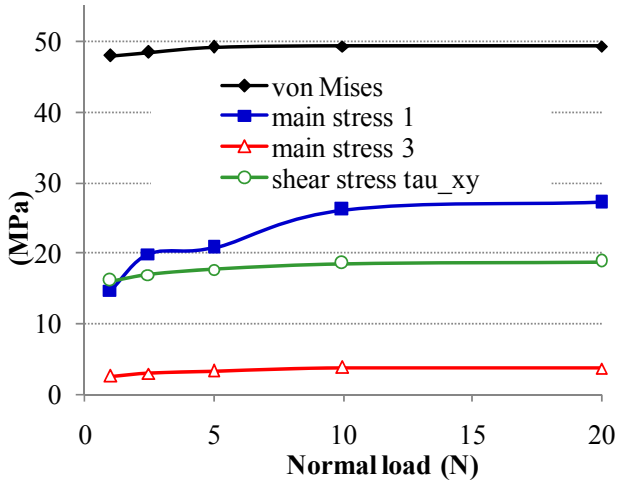

Fig. 8. *The maximum values of stresses in the polymeric block, as a function of the applied load*

Due to the elasto-plastic nature of the block, the maximum von Mises stresses could overpass the yield limit of the material (47.3 MPa, as determined from tensile tests). For the studied loading interval, the program running evidenced an almost linear dependence of the maximum total strains and the maximum plastic strains with the normally applied load (Fig. 9).

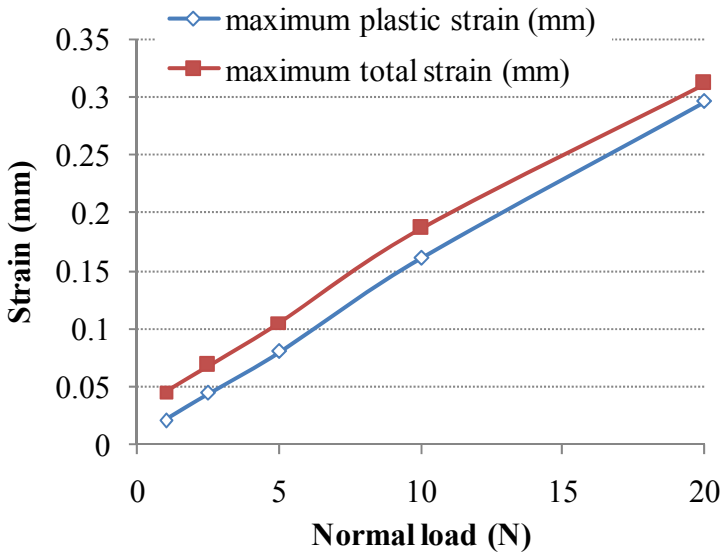

Fig. 9. *The maximum strain in the polymeric block, as a function of the applied load*

Figure 9 presents the dependence of the maximum total strain and of the plastic strain on the normally applied load. The value of the total maximum deformation is very close to maximum plastic one.

This FEM modeling could help the designer to evaluate a frictional contact even without doing laboratory tests.

The conclusion from this figure is that the material could support high loads because of its elasto-plastic nature.

4. Conclusions

After running the model for several normally applied forces, the authors have drawn the following conclusions.

The zones with plastic deformations are small as compared to the block size for all analyzed cases. The deformations are transmitted toward the clock interior, along the direction of the normal force. The shape of the block in the contact zone has the tendency of becoming that of a shoe, this explaining the distribution of stress and good behavior of the polymer at high forces (Figs. 6 and 7).

The block material could support high loads due to local plastic deformations that do not allow the generation of local high stress peaks.

The shear stresses (τ_{xy}) have high values, theoretically close to the shear limit (here considered approximately 20% of the tensile limit for many thermoplastic polymers [3, 4].

The distribution of the parameter STRESS INTENSITY (the difference between the main stresses σ_1 and σ_3) is relevant for evaluating the damaged zone of the contact, especially when the friction is introduced (Fig. 10, for F=20 N). The zone when this parameter reaches maximum values is that where the material could be broken and then dislodge through wearing.

This model is useful for reducing the design time and the time for evaluating the contact.

A FEM model will behave closer to the actual one if there are introduced parameters that have been experimentally determined. The presented model used the information obtained from tensile tests, introducing points from the stress-strain curve as obtained from actual tests and information obtained from tribological tests (here, the friction coefficient).

References

[1]. Benabdallah H. S., Olender D. - *Finite element simulation of the wear of polyoxymethylene in pin-on-disc configuration*, Wear, 261 pp. 1213-1224, (2006).

[2]. Boazu D., Gavrilescu I. - *Contactul mecanic. Analiză cu elemente finite*, Editura EUROPLUS, Galaţi, ISBN 978-973-7845-40-5, (2006).

[3]. Brown J. - *Handbook of Polymer Testing* - Short-Term Mechanical Tests, ISBN 978-1-85957-324-2, (2002).

[4]. Brydson J.A. - *Plastics Materials,* 7th Edition, Butterworth-Heinemann, ISBN 0-7506-4132-0, (1999).

[5]. Frunză G., Spînu S. - *Fundamentele teoriei plasticităţii. Aplicaţii în mecanica contactului elasto-plastic*, Ed. Universităţii "Ştefan cel Mare", Suceava, ISBN 978-973-666-336-9, (2010).

[6]. Godet M., Berthier Y., Lancaster J., Vincent L. - *Wear modelling: using fundamental understanding or practical experience?,* International Conference on Wear of Materials, Orlando, USA, (1991).

[7]. Kim N. H., Won D., Burris D., Holtkamp B., Gessel G.R., Swanson P., Sawyer W.G. - *Finite element analysis and experiments of metal/metal wear in oscillatory contacts*, Wear, 258, pp. 1787-1793, (2005).

[8]. Kónya L., Váradi K., Friedrich K., Flöck J. - *Finite element heat transfer analysis of a peek-steel sliding pair in a pin-on-disk configuration*. Tribotest J., 8–1 (September), pp. 3–26, (2001).

[9]. Kónya L., Váradi K. - *Wear stimulation of a polymer-steel sliding sliding pair considering temperature- and time-dependent material properties,* in Friedrich K., Schlarb A.K. (editors), Tribology of Polymeric Nanocomposites – *Friction and Wear of Bulk Materials and Coatings,* Tribology and Interface Engineering Series, 55, Elsevier, ISBN: 978-0-444-53155-1, Part I: Bulk Composites with Spherical Nanoparticles, pp. 17-148, (2008).

[10]. Mukras S., Kim N.H., Sawyer W.G., Jackson D.B., Bergquist L.W. - *Numerical integration schemes and parallel computation for wear prediction using finite element method*, Wear, 266, pp. 822-831, (2009).

[11]. Kral E.R., Komvopoulos K. - *Three-Dimensional Finite Element Analysis of Subsurface Stress and Strain Fields Due to Sliding Contact on an Elastic-Plastic layered Medium*, Transactions of the ASME, vol. 119, no. 4 pp. 332-341, (1997).

[12]. Moratal D. (editor), **-** *Finite Element Analysis*, Sciyo, Croatia, ISBN 978-953-307-123-7, (2010).

[13]. Pödra P., Andersson S. - *Simulating sliding wear with finite element method*, Tribol. Int., 32, pp. 71-81, (1999).

[14]. Yan W., O'Dowd N. P., Busso E. P. - *Numerical study of sliding wear caused by a loaded pin on a rotating disc*, J. Mech. Phys. Solid, 50, pp. 449–470, (2002).

[15]. Zhil'tsova T. V., Neto V. F., Fonseca A., Oliveira M. S. A. - *Numerical Simulation of a PBT Component with Molded-in Metal Insert,* PMI 2008 – 3nd International Conference on Polymers & Moulds Innovations, University College Ghent, Belgium, pp. 1-6, (2008).

[16]. *** COSMOS/M version 2.9.

[17]. *** winTest™ Analysis universal testing software.

THE ANNALS OF "DUNAREA DE JOS" UNIVERSITY OF GALATI.
FASCICLE IX. METALLURGY AND MATERIALS SCIENCE
N^0. 4 – 2012, ISSN 1453 – 083X

METHOD OF DETERMINING THE MAIN FEATURES OF MAGNETIC FERROMAGNETIC MATERIALS

Livia GHEORGHIEŞ, Ovidiu DIMA
"Dunarea de Jos" University,
email: lgheorg@ugal.ro

ABSTRACT

The purpose of this paper is to present a method for determining the main magnetic features such as magnetic induction B, magnetization M, the coercive magnetic field Hc, permeability μ, using hysteresis cycle chart.

The method can be used for:

-determining the amounts of phase with the existing magnetic properties of ferrous alloys,

-determination of delta ferrite in austenitic steels and the weld seam weld bonding of these steels,

-pointing to the deformation of martensitic transformation in cold austenitic stainless steels and proper calibration, intensity estimation of martensitic transformation and the amount of martensite in the structure.

KEYWORDS: magnetic properties, hysteresis cycle, the martensitic transformation

1. Introduction

Knowing the characteristics of magnetic materials is important for achieving their selection and use of equipment and technology in the industry [1].

The purpose of this paper is to present a method for determining the main magnetic features such as magnetic induction B, magnetization M, the coercive magnetic field Hc, permeability μ, the hysteresis cycle obtained using the chart on the screen of an oscilloscope.

A ferromagnetic sample can be considered as consisting of fields of magnetization with magnetic moments oriented randomly, so the total magnetic moment is zero proof figure 1a [3], [4]. If the evidence of such an external magnetic field is applied, the fields tend to be guided by the direction field, which produces a total magnetic moment nonzero figure 1b.

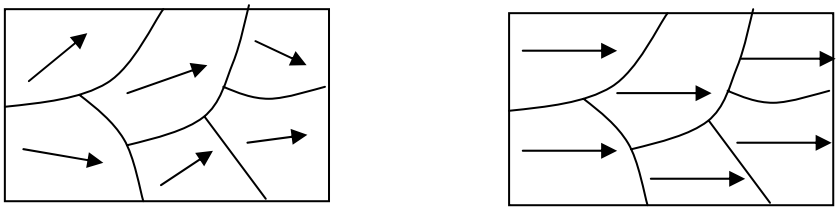

a) H=0, M=0 b) $\vec{H}\neq 0$, $\vec{M}\neq 0$

Fig. 1. *View on orientation magnetic domains*

Magnetic moment of unit volume is called magnetization $\vec{M} = \frac{d\vec{m}}{dV}$, and is measured as the magnetic field H in A/m. Between magnetic induction B, magnetic field H and magnetization M is the following relationship:

$$\vec{B} = \mu_0 \left(\vec{H} + \vec{M} \right) = \mu \vec{H} \quad .$$

Dependence of B and H of M is a linear function of ferromagnetic materials that, with increasing field, tending to increase the

magnetization saturation value Ms, OC curve figure 2 [2].

Decreasing to zero field is found that magnetization decreases only up to the Mr, called remanent magnetization and to cancel the magnetization, demagnetize the sample, should apply a magnetic field of opposite sign first -Hc value. The field is called the coercive field Hc. Growing up in this new field so again reach saturation value -Ms, the magnetizației the point on the curve D and the decrease is obtained, -Mr, with the new sense of the field. Purpose of reversing the field again and raised her son to obtain the saerple demagnetization +Hc saturation value and then to +Hmax. Magnetizației variation curve corresponds to a change in the field from +Hmax. to -Hmax. and again to +Hmax. cycle is called hysteresis, figure 2. Using a magnetic field produced by an AC frequency of 50Hz, the sample will be magnetized and demagnetized with this frequency. If by any means whatsoever is applied to X plates of an oscilloscope with a voltage proportional to the magnetic field applied e_x sample and the Y plates of the oscilloscope e_y apply a voltage proportional to the magnetization, then the oscilloscope screen will appear that the sample characteristic hysteresis cycle.

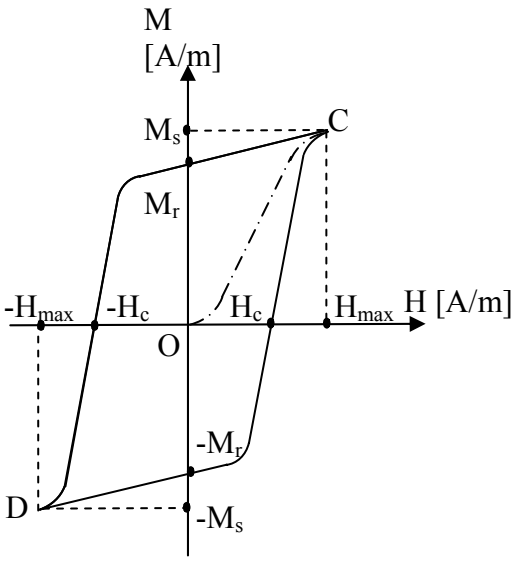

Fig. 2. *Shape of hysteresis cycle*

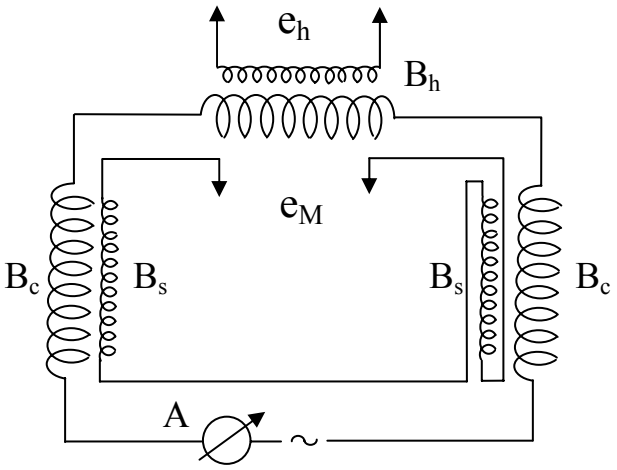

Fig. 3. *Electrical schema of experimental measurements*

2. Layout

Schematic diagram of the facility is shown in figure 3. Supply circuit is made from an AT to have an adjustable voltage. Bc identical coils are solenoids that produce their center on their axis of symmetry, a known magnetic field intensity H.

(H = 1.2 x104 / m, for a current of 1A through their turns). The two coils are connected in opposition probe Bs and Bc are placed inside the solenoids in their center, each having 5200 turns each. Coreless transformer is Bh, the mayor crossed the stream causing the solenoids magnetic field Bc. Thus to obtain a transformer secondary voltage:

$$e_H = -\frac{d\Phi}{dt} = -\mu_0 S \frac{dH}{dt} \quad , \quad \Phi = B.S = \mu_0 H.S$$

where: μ_0 is the magnetic permeability of vacuum, S is the average size of the transformer secondary turns Bh and H is the magnetic field created by electricity transformer primary of the circuit.

This voltage is directly proportional to e_H with current and hence the circuit is proportional to the magnetic field Bc:

$$e_H = C_1 \frac{dH}{dt} \quad , \quad C_1 = -\mu_0 S \quad .$$

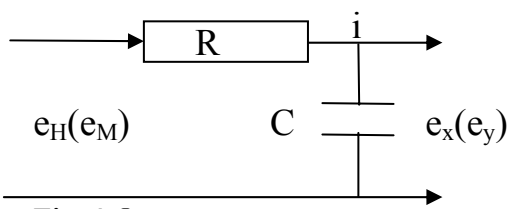

Fig. 4. *Integration circuit*

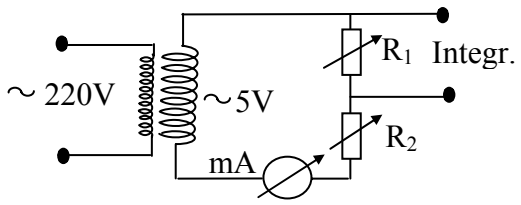

Fig. 5. *Electrical transformer and integrated circuit*

To have the X terminals of the oscilloscope voltage proportional to field strength magnetic e_x, will have to be integrated voltage e_H. Voltage integrated circuit for e_H is composed of an electrical resistor with resistance R and a capacitor with capacitance C, figure 4. Figure 5 is shown coupling an integrated circuit in a transformer.

Choose R so R>> Xc, where Xc = 1/ω.C is capacitive reactance of the capacitor . In these circumstances, the electric current in the circuit can be approximated by i = e_H / R. How voltage across the capacitor is collected e_x = Q / C where Q is the way electric charge accumulated on any plates of the capacitor is related to the intensity of electric current in the circuit through the relation $Q = \int idt$.

Follows:

$$e_x = \frac{Q}{C} = \frac{\int idt}{C} = \frac{\int \frac{e_H}{R} dt}{C} = \frac{1}{R.C} \int e_H \, dt$$

$$e_x = \frac{1}{R.C} \int C_1 \frac{dH}{dt} dt = K_1.H \text{ , where } : K_1 = \frac{C_1}{R.C}$$

Since R>> Xc, electric voltage e_x (that is integrating well e_H), is much lower than the voltage e_H, choose R / Xc = 100-1000, and sometimes provides an amplification of the tensions at the entrance to the oscilloscope.

X terminals connected to the oscilloscope, e_x voltage will cause a horizontal line with length proportional to the amount of magnetic field intensity H. In the absence of a ferromagnetic sample probe within any of the coils, the voltage across pick Y is zero. The two voltages obtained from the two probe coils are equal in magnitude and opposite in phase, the probe coils are identical but connected in opposition. The two coils are crossed by flows Bs magnetic $\Phi_1 = \mu_0$.NHS, $\Phi_2=\mu_0$.NHS respectively, where N is the number of turns and S turns average surface coil probe. $B_0=\mu_0 H$. Since these flows can be written as: $\Phi_1=NSB_0$ $\Phi_2 = NSB_0$ respectively. Total flow becomes $\Phi_t = \Phi_1 - \Phi_2 = 0$.

When the coils in a probe, eg a coil probe, place a ferromagnetic sample with relative magnetic permeability μ_r and section and flows through is **s** the two coil magnetic probe are: $\Phi_1'=N.B_0$ (S-s) + NBS, respectively $\Phi_2'= NSB_0$, B= μ.H = $\mu_0.\mu r$.H. Given the link between magnetic field intensity H, the sample relative magnetic permeability μ_r its magnetization is M = H (μ_r-1).

Total magnetic flux becomes: $\Phi'_t = \Phi_1' - \Phi_2$ Φ'_t = N.B_0 (S-s) + NBS-NSB_0 = Ns (B-B_0), or:

$\Phi't = NsH\ \mu_0\ (\mu r-1) = Ns\ \mu_0$. M.

Because the magnetic field varies in time, be produced by an alternating current, and that the sample magnetization M varies over time and consequently in the total magnetic flux Φ'_t. The two coil circuit a voltage probe appears induced e_M.

$$e_M = -\frac{d\Phi_t^1}{dt} = -N.s.\mu_0 \frac{dM}{dt} = C_2 \frac{dM}{dt} \quad .$$

$$where \ : \ C_2 = N.s.\mu_0 \quad .$$

Integrating and this voltage can be applied to Y plates of an oscilloscope e_Y voltage directly proportional to the sample magnetization M. $e_Y=K_2$.M, where K_2 is a constant. Applied e_Y voltage oscilloscope entry Y, will cause a vertical line on the screen, whose length is proportional to the magnetization M. The composition of the two voltages e_X and e_Y is obtained on the oscilloscope of the sample studied hysteresis cycle M = f (H) .

2.1. Calibration facility

Calibration facility can be done using a sample whose magnetic characteristics were determined following previously on other plants or process described below.

a) Calibration of horizontal. Since the coercive field of the sample is measured horizontally, the magnetization is zero, it must be known accurately represent the magnetic field in units of a division on the oscilloscope. If the screen has 50 divisions, knowing the value of the field of reading an ammeter electric current intensity, determine the division.

The hysteresis cycle of the test chart is read corresponds to the number of divisions that Hc, multiplying it with the value in A / m, of a division in determining the value of Hc in A / m

b) vertical calibration. This can be done using an adjustable AC and u_C = Um.sin(ω.t) known type which can be regarded as being generated by a time-varying magnetic flux form:

$$\Phi_C = -\int u_C dt = -\int U_m . \sin(\varpi . t) dt$$

$$\Phi_C = \frac{U_m}{\varpi} . \cos(\varpi . t) = \Phi_{Cm} . \cos(\varpi . t)$$

where: Φ_{Cm} maximum flow calibration.

If the maximum length Φ_{Cm} corresponds lm=50mm, then the flow corresponds to a certain length Φ_Y, l_Y spot oscilloscope vertical deviation.

But $\Phi_Y=\Phi_t=\mu_0$N.s.M=$\Phi_{C.m}l_Y/l_m$., Follows:

$$M = \frac{\Phi_{C.m}}{\mu_0.N.s} . \frac{l_Y}{l_m} = \frac{U_m}{\varpi.\mu_0.N.s} . \frac{l_Y}{l_m}$$

Maximum voltage is related to the actual value

$$U_m = \sqrt{2}.U_{ef} \text{ , } M = \frac{\sqrt{2}.U_{ef}}{\varpi.\mu_0.N.s} . \frac{l_Y}{l_m} .$$

For our installation we: U_{ef}=16V, ω=314 s^{-1} for ν=50Hz, $\mu_0=4\pi\ 10^{-7}$H/m, N=5200 turns, l_m=50mm.

We can write M=$K_2.l_y/l_m$, where

$$K_2 = \frac{\sqrt{2}.U_{ef}}{\varpi.\mu_0.N.s} . \frac{l_Y}{l_m} = 0,22 \ A.m / mm$$

Measuring l_Y in millimeters vertically Mr. and Ms, and knowing. section sample **s** can be determined and the residual saturation magnetization of the sample studied. Knob vertical amplifier must remain in the same position during the measurement and calibration. The equipment allows the determination of the coercive field H_C magnetizaţiei residual saturation of the M_r and M_S with an error of about 8% satisfaction measurements for samples with the same series and cross section of the same material. You can also determine the maximum magnetic permeability $\mu_{max} = B / H = \mu_0 \Delta M/\Delta H$,

M> H in the coercive field because at this value of the displacement field occurs irreversibly block wall that delimits the areas of evidence leading to a marked rise in ferromagnetic magnetizaţiei it. Energy losses in the magnetization are proportional to the area enclosed by the hysteresis cycle.

Thus the density of energy loss will be:

$$w = \mu_0 \oint \vec{M} \, .d \, \vec{H}$$

Energy losses per unit volume, a hysteresis cycle is calculated as the product of magnetic permeability of vacuum μ_0 and area of hysteresis cycle M= f (H) expressed in units of physical quantities M and H.

3. Working mode

Carry istalation in figure 3. It connects to an adjustable voltage source, an autotransformer. Adjust autotransformer with a suitable amount of electric current through the coils B_C, 1A or 2A is recommended. Connect the voltage output from integrated circuit boards deviation X, Y of the oscilloscope respectively.

Hysteresis cycle falls on the oscilloscope for parts handling it centered vertically and buttons that amplifications potentiometers on the oscilloscope's horizontal. Plot to scale on graph paper on screen hysteresis cycle. Read the Graphic Divisions for X_C, Xmax, Yr, Y_S appropriate physical quantities H_C, Hmax, M_r, and M_S respectively.

Hysteresis cycle area is evaluated by counting the squares of graph paper. Hmax is determined by applying three simple rule worth knowing that a 1A current intensity magnetic field strength value is $1.2x10^4$ A/m.

H_C is determined by applying three simple rule given that the corresponding graph is linear horizontal scale:

H_{max}……X_{max}(mm)
H_C… ……X_C(mm) $H_C=H_{max}.X_C/X_{max}$

The sectional area of the sample **s** were calculated in m^2. Magnetizations remanent and saturation is calculated with:$M_{r(S)}=K_2Y_{r(S)}$ /s where: K_2=0,22 A.m/mm.

Magnetization M_0, mm corresponding to a vertical axis of the graph is determined using the formula: $M_0 = K_2./s$.

H_0 of the magnetic field intensity corresponding to mm on the horizontal axis of the graph is finished by applying three simple rule:

H_{max}……X_{max}(mm)
H_0……1(mm) $H_0=H_{max}./X_{max}$

Calculate: $s_0=H_0.M_0$ (în A^2/m^2) for $1mm^2$ cycle area and then the hysteresis cycle area: $A_{ciclu}=p.s_0$ where p- number mm^2 in the cycle graph area.

The density of energy losses in the magnetization arising from the relationship: $w=\mu_0.A_{ciclu}$ and is expressed as: w/m^2.

Plot the tangent to the graph figure 6, in the vicinity of the coercive field, $-H_C$ and calculate its slope tg $\alpha=\Delta M/\Delta H$, so:

$\Delta M=M_0$ x number of squares in which the vertical tangent.

$\Delta H=H_0$ x number of squares in which the horizontal tangent

Maximum magnetic permeability of the sample is determined by the relationship:

$\mu_{max}=\mu_0.\ \Delta M/\Delta H$ (H/m).

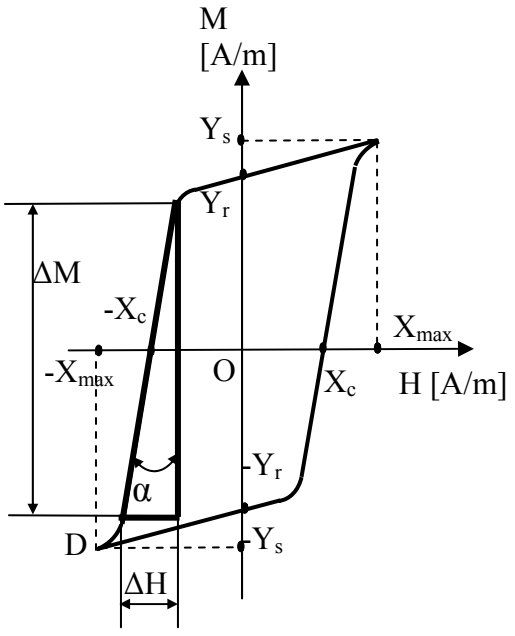

Fig. 6. *Hysteresis cycle and determination of magnetic permeability*

4. Conclusions

The method can be used for:

-determining the quantities of phase with the existing magnetic properties of ferrous alloys,

-determining the amount of delta ferrite in austenitic steels and the weld seam weld bonding of these steels,

-martensitic transformation highlighting the cold deformation austenitic stainless steels and proper calibration, intensity estimation of martensitic transformation and the amount of martensite in the structure.

References

[1]. N. Tiagu, C. Gheorghies - *Fizica corpului solid. Aplicatii practiCe,* Ed. Ars Docendi, Bucuresti, (2003).

[2]. S. Condurache-Bota - *Carte de lucrari practice de Fizica generala,* Ed. CERMI, Iasi, (2011).

[3]. O. Dima - *Cercetaro privind comportarea la coroziune a unor oteluri inoxidabile si a imbinarilor lor sudate in medii industriale agresive.* Universitatea Dunarea de Jos Galati, (2007).

[4]. O. Dima O. Mitoşeriu C. Gheorghieş - *Influenţa deformării plastice la rece asupra proprietăţilor magnetice şi de rezistenţă la coroziune şi abraziune a unor oţeluri inoxidabile austenitice..* Conferinţa ştiinţifică UGALMAT 2005, *Tehnologii şi materiale avansate* Universitatea Dunărea de Jos Galaţi.

THE ANNALS OF "DUNAREA DE JOS" UNIVERSITY OF GALATI.
FASCICLE IX. METALLURGY AND MATERIALS SCIENCE
N^0. 4 – 2012, ISSN 1453 – 083X

MEASUREMENT AND ANALYSIS OF VIBRATIONS ON A COLD ROLLING MILL FOR STEEL STRIP

Stefan DRAGOMIR, Nicolae DIACONU, Marian BORDEI
"Dunărea de Jos" University of Galati
email:mbordei@ugal.ro

ABSTRACT

In this paper the authors made measurements and registration of vibration by using accelerometers posted on the top backup rolls. This is a new way for predict the damage in the rolling mill equipment and the precision of laminated strip. Also is need this technology for monitoring the strip shape combined with a complex system of control for technological parameter of rolling mill process All these monitoring systems is necessary because the demands on the quality of rolled strip is happened in real time.

KEYWORDS: prediction, monitoring, strip shape, mill chattering

1. Introduction

The control of rolling mill process, consist in two ways. The first way is to analyze the rolling mill that deformed the material and second is to continuous recorded of drive and work parameters. It is the way to know where is the future damage that can to appear in the mill machine system and the possibility to prevent the malfunction and the default for the sheet dimension (rolled strip thickness differences).

Dynamic analysis of plate and strip mills is in the idea of reducing the weight of these assemblies, the failure to avoid excessive size and time required for certain parts dynamic. This analysis is done by comparing the initial vibration signal (at the commissioning of the mill) with the vibration signal measured after a certain time of operation.

Monitoring of parameters is practically the feedback from those who participate in the iterative process of optimizing the operation of the mill process. The measurement and calculation procedures described below apply known.

The innovations elements are accessibility, flexibility, speed and power. Necessary hardware features dynamic measurements can be grouped as follows: size mechanical transducers (strain gauge, force cells, displacement transducers, accelerometers, etc.).

The whole transfer function or functions derived from measurements of time recorded even if they were obtained by simultaneous acquisition can be used for graphical representation of distortions.

In case of transfer functions can be simulated deformations that occur under the action of forces other than those actually used for measurement. For example, disposing of transfer functions measured with the excitation pulse can simulate and plot the likely deformations under the action of a certain frequency sinusoidal forces. They can also be identified frequencies at which parts deformation is at maximum. Of all the research results made the current problem is to analyze the conditions for scientific working of rolling mills, the identification and quantification disturbing factors and finally, modern design, for increasing resistance, reliability, reduce consumption, ensure continuity processes and product quality finished [1]. All this led to the development of a general concept for the establishment of dynamic influences on complex machinery and quantification of the dynamic forces. The modern analysis of the tensions leads to the design with a minimum of approximation and uncertainty of sub-assemblies of equipment [2].

One of the main measures in the design and optimization systems for machinery important action is to determine the size of dynamic moments that may occur during operations.

2. Experimental procedure

2.1. Measurement of vibrations on the cold rolling mill machine

The equipment for measurement of vibration is described, with the main orientation for viewing and

analysis of three-dimensional deformations of complex structures subjected to vibration stresses. The measurements were made with transducers placed upright, horizontal and axial position-on cylinders support in the operator side.

We have not registered print and sudden wave variations in the thickness of rolling strip. During the measurement we are recording signals during normal operation of the vibration sources in rolling mill machine work.

The conditioning has functions to convert the transducer output voltage in the standard signal (the voltage is between ± 1V and ± 10V with low impedance) to conduct or offsetting characteristics transducer linearity and limit the frequency of the field required. For acquisition board we use A / D conversion (National Instruments AT-MIO-16E2), computer (PC compatible). The last three components are part of the experiment, using Lab VIEW application. Without going into details of the transducers may be worth noting that virtually no restrictions on the type of sensors used or the manufacturer.

Minimum necessary to perform the full range of dynamic measurements is two channels of input and output channel.

Analog output channel can be used to generate the excitation signal and the two signal input channels to measure real and that the excitatory response [4]. By using multiple input channels and therefore more transducers, the exact same results are obtained but in a shorter time (shorter working time is not proportional to the increasing number of channels). Excitation signal generated by computer can be designed to cover a whole range of frequency and type can be selected by scanning sinusoidal noise type with limited bandwidth or pulse.

Vibrations of the functional parts of the mill frame are investigated by simultaneous recording of signals with two transducers (Fig.1). One of them is mounted on the backup roll (drive side) and the other is mounted on the other backup roll (operator size).

The vibration parameters (displacement, frequency and acceleration) are done automatically, without supervision. Partial results are saved periodically. If processing speed is very low we can eliminate disturbances that exceed the useful signal amplitude. The results are stored as average power spectra. Obtaining power spectra may take a while the order of minutes or hours.

Due to the modularity and compatibility of National Instruments products, system acquisition can be completed with programmable filters, galvanic isolators, analog multiplexers, bridges and other load cells.

Acquired signals are standard signals in the ± 10V voltage, single or differential, which enables connection to most types of existing sensors and signal conditioner. Acquisition system may include, besides the signal generator and digital PID controllers, DSP processors, in a series of products the company National Instruments Motion Control for controlling the operation of sources of vibration, hydraulic or electro [5].

For the first date the experiments were made on a laboratory cold rolling mill for steel strip in two phases, from February to October 2012 - with performance equipment and up-to-date acquisition equipment like: line of data acquisition: transducers, preamplifiers, filters, analog-digital converter; modal analyzer, with data acquisition in Lab VIEW programming environment. It was realized 115 different charts [5], have been made by this equipment. To make the measurements of: displacement, accelerations and frequency, transducers were fixed upper and lower cylinders support of considered rolling mills by the vertical and horizontal direction. (Fig. 1).

The experiment that we made, lead to particular trends of mechanical properties and may be utilized for optimization of work parameters steel in a cold strip rolling mill, reflecting the specific requirements for a relation between strength and plastic properties of laminated carbon steel.

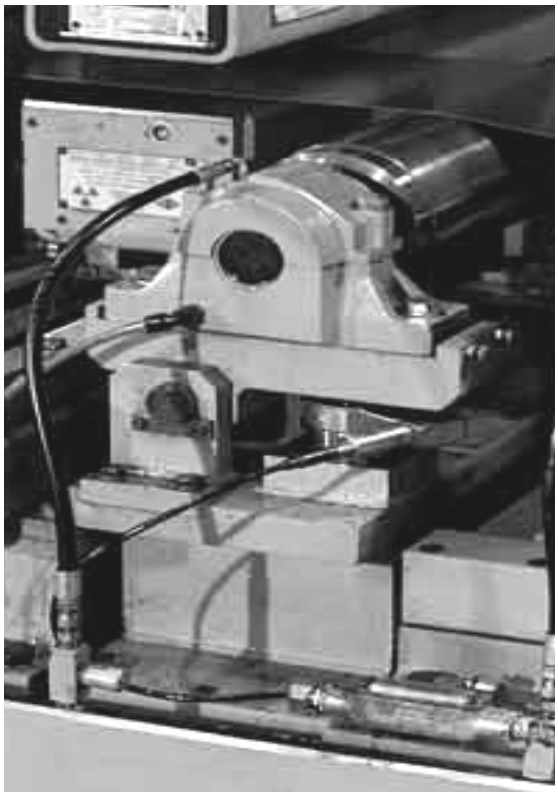

Fig. 1. *Accelerometers mounted on back-up of the cold rolling mill, (in the equipment laboratory), for vibration measurement*

Other experiments were performed on the cold rolling mill machine for steel strip (LBR1-Arcelor Mittal S.A). It observe that in the last cages of the milling tandem respectively four and five, there are the recorded the lowest values for displacements, acceleration and frequency vibrations. These values represent the latest stage in the achievement of the finished milling product [5].

The measurements were performed on 28 cold rolled carbon steel strips, after which the change was made on the working cylinders. The frequency of vibrations are influenced by the speed of rotation of the cylinders, rolling force, the tension between frames, emulsion used - the characteristics of vibrations and they were recorded during mentioned periods of time - On the surface of the last 5 rolls rolled- before the change of working cylinders, we see traces and printings were noticed belonging to these cylinders.

3.3. Results and discussions

The measurements that are made on the laboratory equipment and in parallel on a real cold milling machine, showing the amplitude, accelerations and frequency spectrum of vibrations that occurred in the rolling mill process. The accelerometers are mounted on the lower and upper cylinders support, on the operator and the drive side.

Vibration measurement in cold rolling mill has been carried out with accelerometers being mounted on the work and bottom roll chocks. Strip thin was 0.4mm. Such result is obtained if we suppose that upper housing do not represent symmetrical stack part. Thick strip stable rolling was available at the high speed without chatter.

Rolling mill machine had the same technical condition and almost the same rolling parameters (steel type, work rolls, loads, speed between entering and exit from mill machine).

Even with a little output thickness deviations (aprox.0.1mm) strip mechanical properties are preserving. It influences on damping properties of steel strip in the roll bite. Harder strip corresponds to less damping.

Work rolls bending influence only high frequency to 980Hz [6]. Strip variable stiffness in the roll bite may be considered like an excitation parameter in the mill machine. Experiments with the mill drives rotation under the working loads and speed without strip between the works rolls shown that vibration signals is in another patterns

It will be noticed by comparing these data that the highest value of movements was on cylinder upper support (Action part). This is due because of the existence of some vibrations coming from the chain of cinematic shareholders.

The acceleration measured and recorded maximum (shareholders) was about 4.4m/s^2 and from the operator side was about 3.8m/s^2 [5].

After measured and recorded of accelerations we can say:

- the highest amplitude of vibrations has been emphasized in area of drive mechanism.

- the vibrations caused the appearance of some wavy parts on the surface band (exemplified for a sheet with thickness output of 0.3mm and width of 1660mm (in the Arcelor Mittal milling area-LBR1) with up to about 20-40 mm distances between pikes of waves. At mill speeds between 600-1150m/min, the vibration frequencies measured not exceeding 460Hz.

Vibrations in the range of frequencies 5-90 Hz corresponding couplings, gearing, box gears, flaws in the camps.

Vibrations in the range of 125-300 Hz frequencies corresponding to common problems like games in interspaces positioning system, wear in the camps, lubricant used.

Frequency in range of 100-300 Hz is characteristic for positioning system and those interspaces, for the quality of surface of working cylinders. It is noticed a growth of vibrations amplitude of cold rolling mill machine in this range of frequencies.

Frequency in range of 500-900 Hz, show a wear stressed of decks of cylinders support, of their camps (with games in the interspaces), determined the marks in the wave shape due the printing that existing on the surface of rolled strips.

This can lead to the interpretation of surface defects that occurred due to some reasons presented to a point but correlated with the state of wear rolling mill in general, the working cylinders support, the lubricant used.

Experiments in tandem operation revealed: the tendency of growth of vibrations amplitude at high speeds lamination where arise as to increase the speed of rolling with about 50% per rolling mills, registered a magnitude vibrations Growth of around 35% per frame [7].

On the other hand, the band widths with narrow and heavy manifest the same tendency of increasing amplitude vibrations, unlike bands with great width and thickness, where the effect of damping vibrations is considerably higher.

Measures to reduce the load in stage design are:

-choice of cinematic scheme rationale without links liabilities;

-the establishment of real physical processes that occur in equipment with consideration and the mass distribution, game engine and electric characteristics;

- use computer modeling to determine the parameters of simulation-optimal, cinematic and dynamic;
- rational location of the drive mechanisms;
- use of transmission without long or complicated parts.
- design adequate for action and work parts of rolling mill machine.

4. Conclusions

As a major conclusion of the investigation on the basis of which have some researches contracts concluded with ARCELOR MITTAL S.A. and completed - is a pressing need reduction and possible elimination vibrations in order to increase reliability of all the rolling and the production of endless bands in accordance with standards International.

In conditions which do not take into account the effect of varying tasks, and in particular of the dynamic errors appear to dimensioning of machinery components, with repercussions all over the reliability and quality production.

In the researcher made was the following:

1. Under the action tasks variables (interior and exterior system), the chain of cinematic equipment to distort, charging the forces and resistance of the materials from which they are made the components, by installing the phenomenon of fatigue. This is the most frequent cause of the deterioration of equipment subassemblies.

2. Main sources demands are dynamic forces of inertia period starting and braking; games in components from inside the spaces of the cinematic chain entrapment - working; wear subassemblies; faulty execution and assembly, fault of positioning system; the usage of the decks cylinders; hardening band;

4. We can appreciate that the most important dynamic effect, in the cold rolling mill, is mainly due to the positioning system, with take in consideration the kinematic chain, which will transmit the necessary torque and rotational speed of the engine through the gearbox and coupling rods from working cylinders. The experiment should be supplemented by additional vibration analyses explaining other types of damage that can appear in work for rolling mill machine.

5. Work rolls surface temperature is an essentially parameter vibration existence

Vibration frequency harmonics may be used for diagnostic of friction forces. Stands synchronization control is a real method to control the vibration parameters in cold rolling mill machine in work.

References

[1]. Dragomir S. - *Monitoring of iron sheet deformation in the rolling mill process by using CVC system,* Publicată in: XII International Metallurgy Materials Congress, Istambul, Turkie, pag.843 – 847, (2005).

[2]. Portman. N. - *Application of neural networks in rolling mill automation*, Iron and Steel Eng., vol.72, no.2, pp.33-36. (1995).

[3]. Farley, T.W.D., et al. - *Understanding mill vibration phenomena*, Proc. of Int. Conf. "Vibration in rolling mills", Inst. Of Materials, Minerals and Mining, London, UK, 9 November, pp. 5-10, (2006).

[4]. Roberts, W. L. - *Four-h mill-stand chatter of the fifth-octave mode*. In: Iron and Steel Engineer Year Book (1978).

[5]. Dragomir S, Diaconu N, Bordei M. - *Control Process for a Cold Rolling Mills by vibrations and torque.* Anale fasc IX Metalurgie No. 2, (2012).

[6]. Kimura, Y., Sodani, Y., Nishiura, N., Ikeuchi, N. and Mihara, Y., - *Analysis of chatter in Tandem Cold Rolling Mills*, ISIJ International, Vol. 43, No.1,pp. 77-84. (2003).

[7]. Hu, P.H., Ehmann, K.F. - *Regenerative effect in rolling chatter*, *Journal of manufacturing Process*, Vol.3, No.2, pp.88-93, (2001).

THE ANNALS OF "DUNAREA DE JOS" UNIVERSITY OF GALATI.
FASCICLE IX. METALLURGY AND MATERIALS SCIENCE
N^0. 4 – 2012, ISSN 1453 – 083X

IMPROVEMENT OF CASTING TECHNOLOGY BY USING OF EXOTHERMIC FEEDER HEAD AND SIMULATION THE SOLIDIFICATION ALLOY

Beatrice TUDOR
„Dunărea de Jos" University of Galaţi,
email: beatrice.tudor@yahoo.com

ABSTRACT

This paper presentes an simulation program use of feeders exothermic and insulating plates. High quality castings is considerably improved by using solidification simulation flow and cast.

KEYWORDS: feeder exotermic, simulation flow, thermal gradient

1. Introduction

To improve the quality of large castings by prevents the appearance of defects in their walls during solidification process can used the exothermic feeders. Also the solidification process can be improved by computer simulation.

Achieving a high temperature gradient between the feeder head and part (thermal nodes are powered) can be obtained by using exothermic mixtures (as powdery or made up).

2. Improvement of casting technology by exothermic feeder head

The exothermic feeder head is provided with a coating mixture that in contact with liquid metal releases heat, as a result of the exothermic reaction between its components.

Exothermic feeders used are of two kinds:

- low-temperature gradient (50-100K) performed as plates and inserts.
- high-temperature gradient (400-500K) carried the metalothermic load.

The heat released by exothermic mixture is base don exothermic reactions (reduction-oxidation). This type of reactions can be divided into three categories:

- Goldschmidt's reaction, i.e. aluminium oxidation under the action of an oxide (iron oxides)
- aluminium oxidation under the action of oxygen from atmosphere or under the action of chemical combinations that produce oxygen
- combustion of the organic materials (charcoal, sawdust etc).

Goldschmidt's reaction occurs according to the following equation:

$$2Al + Fe_2O_3 = 2Fe\ Al_2O_3 + Q \quad (1)$$
$$2Al + 3\ FeO = 3Fe + Al_2O_3 + Q \quad (2)$$

Material for exothermic feeders heads are divided into five groups:

- Active components which come directly into the oxidation process like aluminum powder, aluminum chips and, ferrosilicon powder;
- Oxidizing components (that provides oxygen needed to carry out the exothermic reactions) like iron oxides, manganese oxides, iron ore, piroluzit, hematite, sodium nitrate or potassium nitrate, chlorides and fluorides;
- Catalysts (special additives for oxidation process control) like fluorides of alkali metals, cryolite and cupola powder;
- Inert components (that ensuring slowing of exothermal reaction and the lowering of temperature exothermic reaction) like quartz sand, chamotte powder, wood flour etc.
- Binder like bentonite, sodium silicate, clay, dextrin and, resins.

The components of exothermic mixture (i.e. the substances that participate in the exothermic reactions and the substances that are thermally inert) cause the reactions with thermal effect. As result this has influence on the ignition temperature and on the burning rate of the mixture.

For these reasons, these exothermic mixtures are chosen depending on the nature alloy (iron, steel, nonferrous alloys), the geometry of the parts and also on the casting conditions.

In addition, the exothermic mixtures must also meet others characteristics:

- exothermic coating must be sufficiently resistant to mechanical action generated of liquid metal flow;
- after reaction finishing the exothermal shell must have the good thermal insulation properties;
- the products of exothermic reactions cannot develop other chemical reactions with the cast metal;
- exothermic mixtures to deliver at a low cost.

Additionally to exothermic feeders heads can be used the exothermic powders.

These are placed above alloys after casting. Their role is to protect the surface of casting alloy to atmosphere contact and provide a supplementary heat input.

Exothermic materials used to realize exothermic heads are chosen depending on the alloy. For the steel parts the composition of these materials are given in Table 1.

Table1. *Exothermic material for carving large pieces of steel*

Product name	Mass content, %					MnO, in slag, %
	Aluminum powder	Slag furnace	Manganese ore	Fluorine	Sodium silicate	
EXO-1	14	46	12	10	18	4.30
EXO-2	14	40	20	8	18	6.21
EXO-3	14	34	30	4	18	6.32
EXO-4	14	28	40	4	14	7.81
EXO-5	14	20	50	4	12	13.2

Exothermic mixtures are classified according to the nature binder:

a. Exothermic mixtures with resins

Last time "FOSECO" made a series of exothermic mixtures for feeders heads used for different alloys. These improve a higher removal index (75-80%).

The four types of mixtures named Feedex in given in Table 2.

Table2. *Types of mixtures Feedex created by "FOSECO"*

Type of mixture	Water content, %
Feedex 3	4
Feedex4	5
Feedex 50	10
Feedex 93	7...9

b. Exothermic mixtures of dextrin

Exothermic mixtures with dextrin have lower hygroscopicity. As result the bushings made of these mixtures can be maintained until the molding up to 2 ... 3 days. The utilization of these mixtures is limited because dextrin is a poor material.

c. Exothermic mixtures with sodium silicate

The bushings made of exothermic mixtures with sodium silicate are less hygroscopicity and can be maintained so long (within 6 days), if the humidity not exceed 2%.

d. Exothermic powder mixtures to cover the upper surface of the feeders

The addition of the exothermic powders on feeder surface is the most simple and common practical solution. On liquid alloy surface develops a strongly exothermic reaction (the heat released is in accordance with the composition of the mixture and with its amount). On alloy surface is created a slag layer that minimizes the heat loss by radiation (the heat released by radiation by surface of feeder is 15 ... 20%).

A prescription for the exothermic mixture that can be placed on the surface alloy is following (mass %): 10 % aluminum powder; 4% iron ore; 3% manganese ore; 3% cryolite, 80% chamotte powder.

For improving the efficiency of the exothermic heads used for large castings the insulating boards can be used. They are made of the same material like exothermal heads.

Insulation board is presented in Figure 1.

Fig. 1. *Example of insulation board*

3. Simulation of the solidification alloy

Other solution to improve the quality of large castings by prevents the appearance of defects in their walls can be the solidification process by computer simulation. MAGMA program is used in this application. Following is presented some images of the variation of the solidification front and the temperature areas.

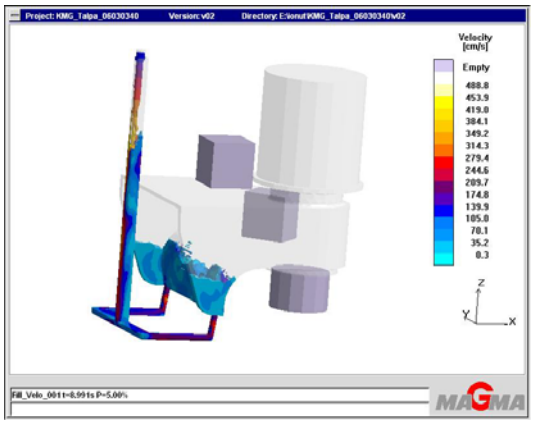
Velocity [cm/s]
Empty
488.8
453.9
419.0
384.1
349.2
314.3
279.4
244.6
209.7
174.8
139.9
105.0
70.1
35.2
0.3

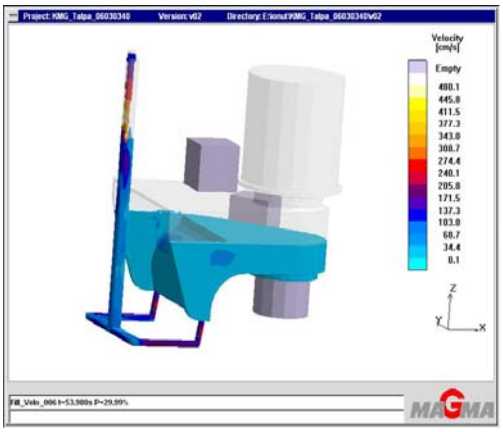
Velocity [cm/s]
Empty
480.1
445.8
411.5
377.3
343.0
308.7
274.4
240.1
205.8
171.5
137.3
103.0
68.7
34.4
0.1

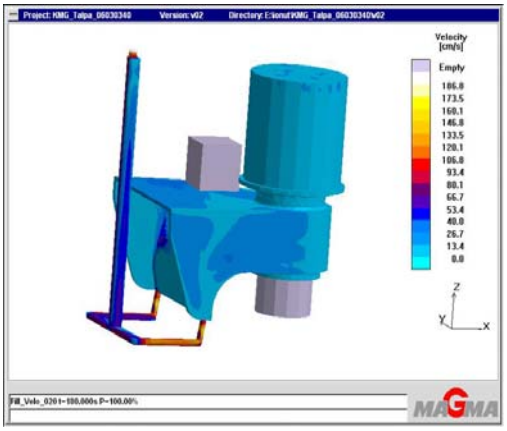
Velocity [cm/s]
Empty
186.8
173.5
160.1
146.8
133.5
120.1
106.8
93.4
80.1
66.7
53.4
40.0
26.7
13.4
0.0

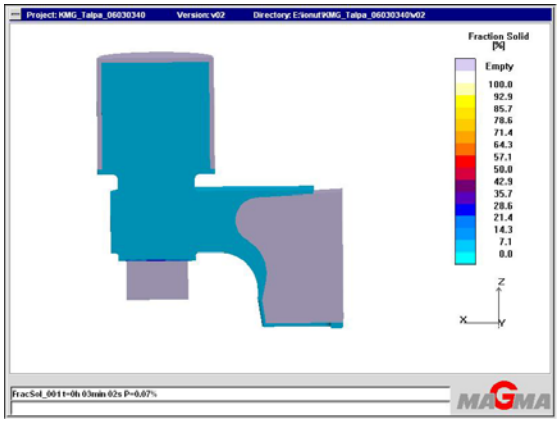
Fraction Solid [%]
Empty
100.0
92.9
85.7
78.6
71.4
64.3
57.1
50.0
42.9
35.7
28.6
21.4
14.3
7.1
0.0

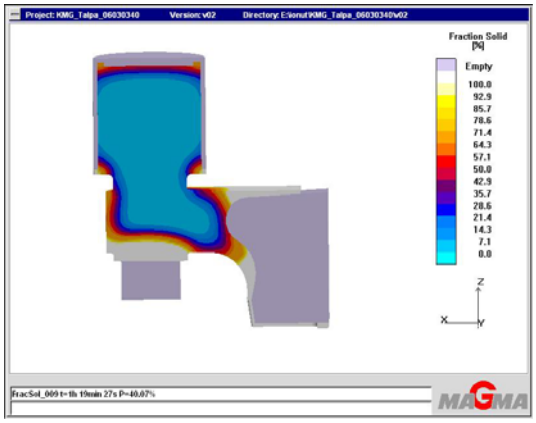
Fraction Solid [%]
Empty
100.0
92.9
85.7
78.6
71.4
64.3
57.1
50.0
42.9
35.7
28.6
21.4
14.3
7.1
0.0

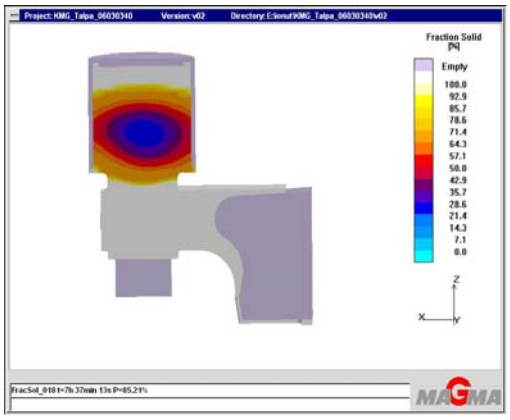
Fraction Solid [%]
Empty
100.0
92.9
85.7
78.6
71.4
64.3
57.1
50.0
42.9
35.7
28.6
21.4
14.3
7.1
0.0

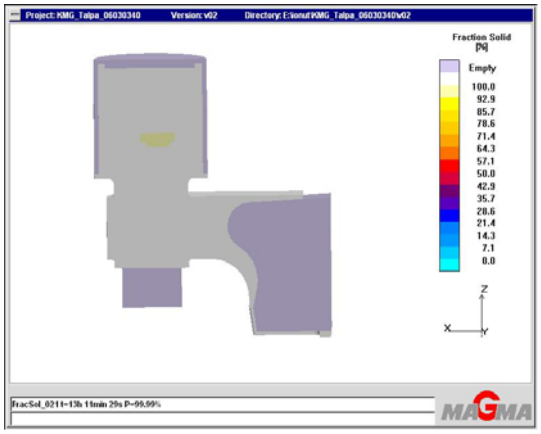
Fraction Solid [%]
Empty
100.0
92.9
85.7
78.6
71.4
64.3
57.1
50.0
42.9
35.7
28.6
21.4
14.3
7.1
0.0

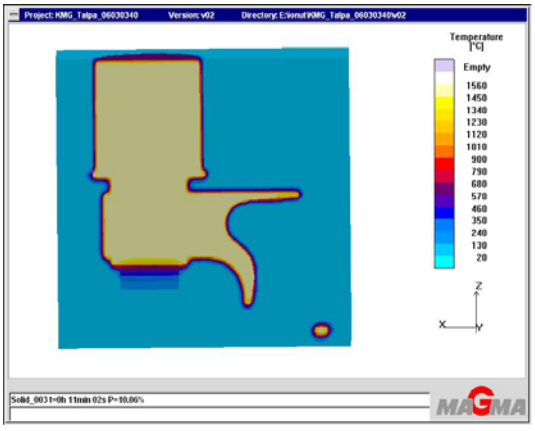
Temperature [°C]
Empty
1560
1450
1340
1230
1120
1010
900
790
680
570
460
350
240
130
20

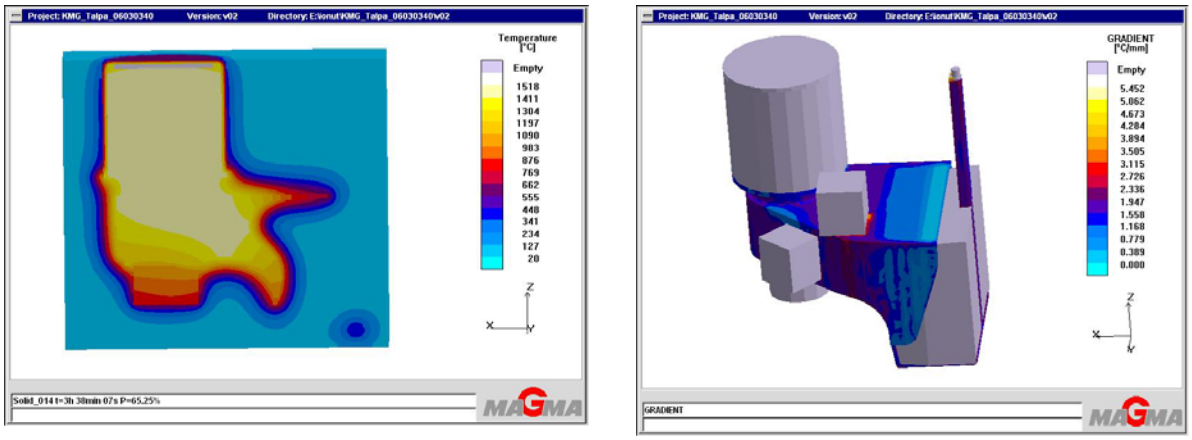

Fig. 2. *Variation of the solidification front and the temperature areas*

Flow simulation and solidification simulation using computer program MAGMA lead to efficient casting process.

Also the implementation of this program leads to the optimal placement of feeders with minimization of the heat loss.

4. Conclusion

The using of the exothermic feeders for large steel castings increases the removal index;

The insulating boards that surround the feeder lead to a smaller loss of heat transferred to the walls shape. The alloy of feeder is maintain longer as liquid.

The application of these methods leads to a healthier walls surface of castings and to a lower processing time.

The solidification simulation using MAGMA program leads to improve the quality of large castings by prevents the appearance of defects in their walls. Also the metal consume is reduced.

As a consequence of the utilization of the simulation program, of exothermic feeders and also of insulating plates can be obtained the better quality of castings and shortening of the time for labor.

References

[1]. J. Campbell - *Castings The new metallurgy of cast metals*, Butterworth Heinemann, (2003).
[2]. J. Brown –*Foseco Ferrous Fondryman's Handbook*, Butterworth Heinemann, (2000).
[3]. E.N. Budonov - *Experienţe privind modernizarea producţiei de piese turnate a firmei Fritz Winter*, Germania, în Liteinoe Proizvodstvo, nr. 5, pag.1-5, (2005).
[4]. E.N. Budonov - *Noile tendinţe ale dezvoltării tehnologiilor de turnare în 2007* în Liteinoe Proizvodstvo, nr. 12, pag.1-7, (2006).

THE ANNALS OF "DUNAREA DE JOS" UNIVERSITY OF GALATI.
FASCICLE IX. METALLURGY AND MATERIALS SCIENCE
N^0. 4 – 2012, ISSN 1453 – 083X

RESEARCH ON THE PRODUCTION OF SINTERED POWDER 316

Simona BOICIUC, Florentina POTECASU
„Dunarea de Jos'' University of Galati
email: simonaboiciuc@yahoo.com

ABSTRACT

The 316 austenitic stainless steel powders are typically used in applications requiring good corrosion resistance, mechanical strength at high and very low temperatures, good ductility, wear resistance, associated in some cases with adequate porosity. The paper presents some experimental research on the production of sintered 316 stainless steel powders and their characterization in terms of microstructure and wear resistance.

KEYWORDS: powder metallurgy, 316 stainless steel, abrasive wear

1. Introduction

The increasing development of the technology for obtaining parts by powder metallurgy and extend their scope of application is due to the advantages presented [1, 2, 3, 7, 8]:

- full use of raw materials compared to other manufacturing processes that use the material at a rate of 50%;
- low energy consumption;
- obtain complex shapes parts of high accuracy and good surface quality, eliminate mechanical processing needed for other manufacturing processes;
- high reproducibility, even for complicated parts in terms of shape;
- flexibility in design and manufacturing;
- isotropic properties due to the structure;
- superior mechanical properties: high hardness, up to 60-65 HRC, utlimate and impact strength, good wear resistance and elongation properties, resistance to fatigue;
- fine and controlled structure;
- obtain new unique properties, these properties are related to pore structure and are represented by the self-lubricating and filtering abilities.
- low cost of large series fabrication compared to forging, casting or cutting technologies.

The technological process of manufacturing sintered parts includes the following phases:

- obtain powdered materials;
- make homogenous the powder or powder mixture having the desired chemical composition;
- obtained by pressing or other means the tablets of metal powders;
- presintering and sintering of powder tablets at high temperatures in a protective atmosphere;
- secondary operations: calibrating the sintered parts, machining or other finishing processes of the sintered parts, oil or easily fusible alloys impregnation of the sintered parts;
- reception and control of the sintered products.

Special attention has been paid in recent years to obtain products of high corrosion-resistant steels with ferritic or austenitic structure.

The 300 series austenitic alloys are typically used in applications requiring good corrosion resistance, mechanical strength at high very low temperatures, good ductility, wear resistance, associated in some cases with an adequate porosity (filters) [4, 5, 6].

The 316 austenitic stainless steel powders are designed for manufacturing various parts in machine manufacturing industry (valves, gears), in petrochemical industry (filters, test probes), energy industry, food, medicine, photographic industry.

With austenitic stainless steels, nickel along with chromium, is the main alloying element. The influence of Ni is opposed to that exercised by Cr, so that with increased Ni content there is an extension of the γ range and a narrowing until progressive disappearance of the range α and $\alpha + \gamma$.

Nickel is dissolved in Fe γ and extends the life range by acting on the descent of the temperatures of the critical transformation points.

According to specialized references [9, 10] nickel causes in stainless steels Cr - Ni two important phenomena:

*extension of austenitic range and increased austenite stability;

*stabilization of phase σ (FeCr) at high temperatures and its occurrence at lower concentrations in chrome, as compared with stainless steels alloyed only with chromium.

In case of a steel containing a major amount of Ni (8-13%), the mixed range (α + γ) occurs with a low carbon content and high temperatures (1400 °C) and the austenitic field becomes very large.

Nickel also contributes to better corrosion performance: resistance to corrosion in air, sea water and acids.

Molybdenum increases the corrosion resistance (pitting) in H_2SO_4 solutions, chloride and organic acids. This paper presents some experimental research on the production of sintered powder 316 stainless steel products and their characterization in terms of microstructure and wear resistance.

2. Experimental conditions

To obtain a sintered parts a powder of 316 austenitic stainless steel with the following chemical composition was used: 0.03%C; 17.1%Cr; 12.09%Ni; 0.51%Si; 2.5%Mo; 0.84%Mn; 0.012%S; 0.03%P; rest Fe.

Fig. 1. shows the aspect of 316 austenitic stainless steel powder.

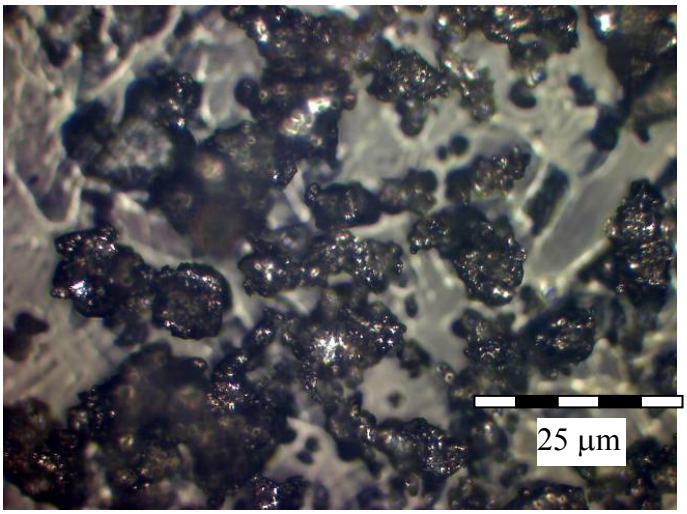

Fig. 1. *Aspect of 316 austenitic stainless steel powder*

Looking at Figure 1 it can be seen that 316 stainless steel powder has an irregular shape specific to water atomisation.

Microhardness determined on the polished section of the particles under a load of 50 g was $HV_{0.05}$ = 939.6 MPa.

The pressing process used was cold pressing, with universal machine for mechanical tests.

The 316 powder compaction pressures used were 540, 628, 726, 863 MPa**.**

Compact samples are cylindrical with dimensions of approximately 8 x 6 mm.

Powder tablet sintering was carried out in an electric oven. Sintering temperature was 1150 ° C and the exposure time to this temperature was 60 minutes. Samples were placed in a ceramic cylinder, where graphite was added.

Graphite has an important role in the cooling stage to prevent air intake in the cylinder, thus providing protection to the atmosphere. After sintering, all samples were cooled slowly.

The main purpose of sintering is to reduce porosity. Sintering process is often accompanied by changes in material, some of them desirable, others not: changes occur in the mechanical strength, hardness; particle size and shape are affected, there is variation in pore shape and size, the chemical composition and crystalline structure may change too due to the appearance of the chemical reaction processes in solid phase.

Microscopic analysis of sintered samples was performed by a Neophot 2 microscope with computer data acquisition.

$HV_{0.1}$ microhardness determined on sintered powder tablets was conducted on a PMT-3 microhardness meter of 100g load.

316 stainless steel sintered samples were subjected to wear test on a rotary disk with sand paper. The method consists in successive pressing, under identical conditions, two samples of size 8 x 6 mm, onto a rotating disk covered with 120 grit sand paper. A radial displacement mechanism of the

specimen with 0.5 mm / rev provide spiral running on the rotating disc surface. A device for applying a load of 6.229 N provides perpendicular pressing of the specimen on the sandpaper to 0.123 N/mm^2 pressure. At a disk speed of 25 rev/min, a lenght of 11.6 m was run.

3. Results and discussions

Microscopic analysis of the pressed tablets performed by Neophot 2 microscope reveals the presence of pores and their shape (Fig.2).

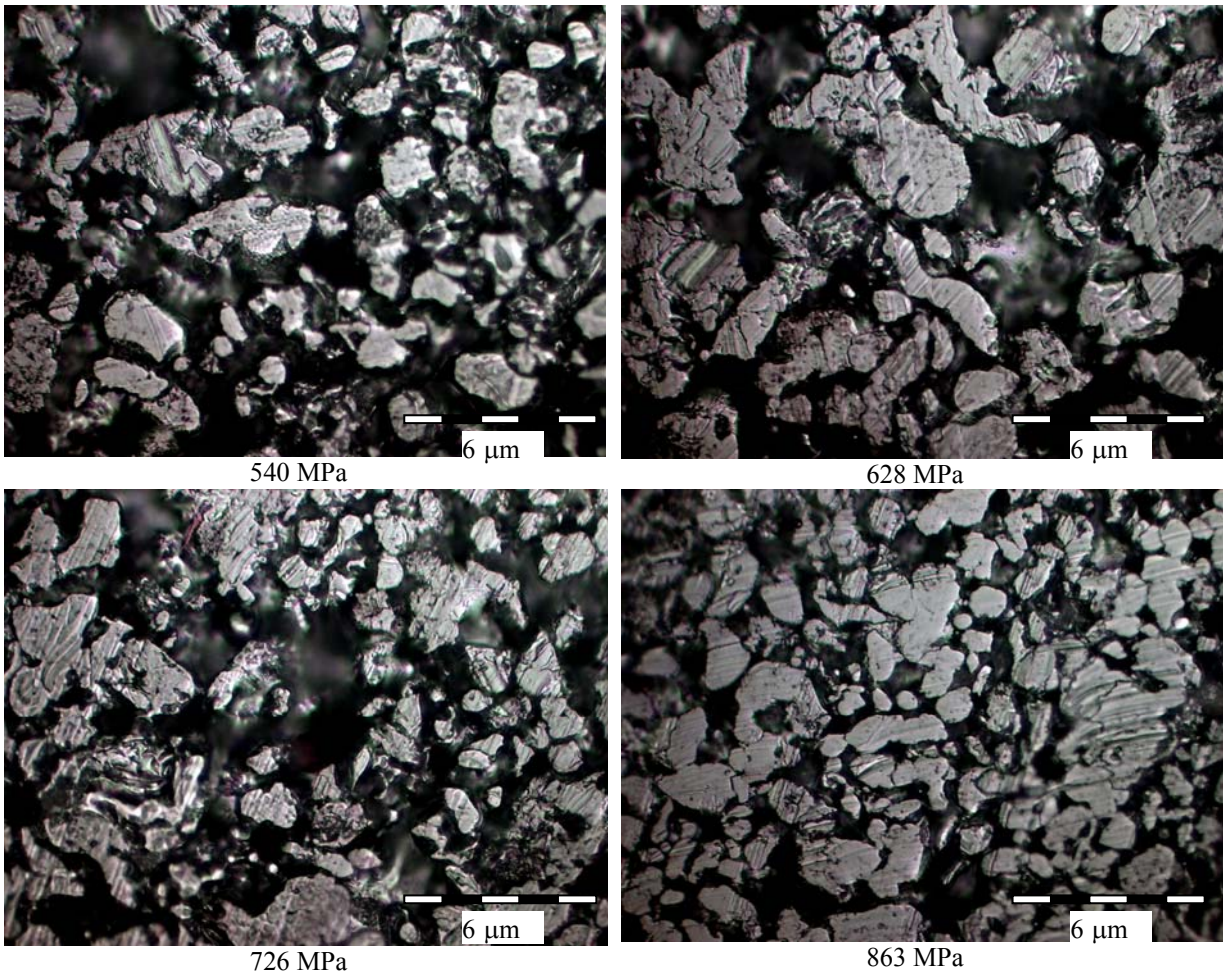

540 MPa 628 MPa

726 MPa 863 MPa

Fig. 2. *Microstructure of 316 stainless steel at different pressures*

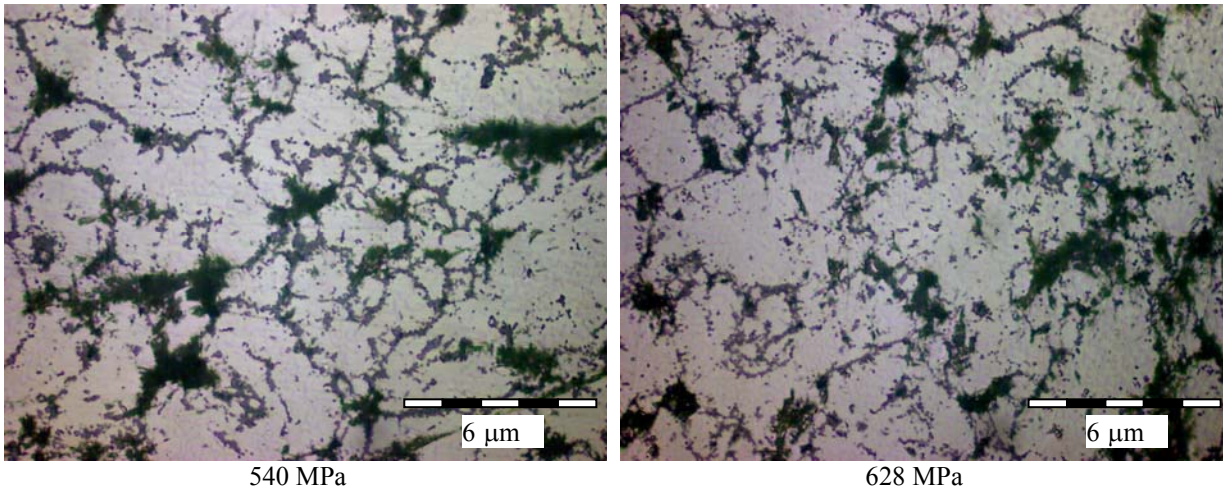

540 MPa 628 MPa

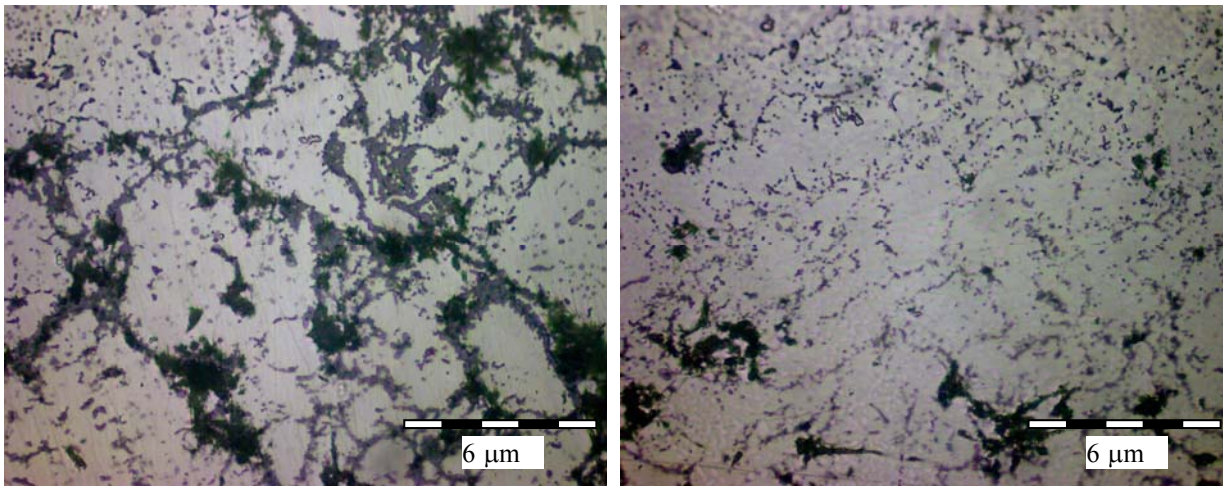

726 MPa 863 MPa

Fig. 3. *Microstructure of 316 stainless steel samples, attack-free*

In Fig. 2 it can be seen that porosity decreases with increasing pressure. Microscopic analysis performed on sintered samples by the microscope Neophot 2 is illustrated in fig.3.

Looking at Fig. 3 it can be seen that porosity decreases with increasing pressure. Microstructure of sintered samples under electrolyte attack with 50% HNO_3 solution is presented in Fig. 4.

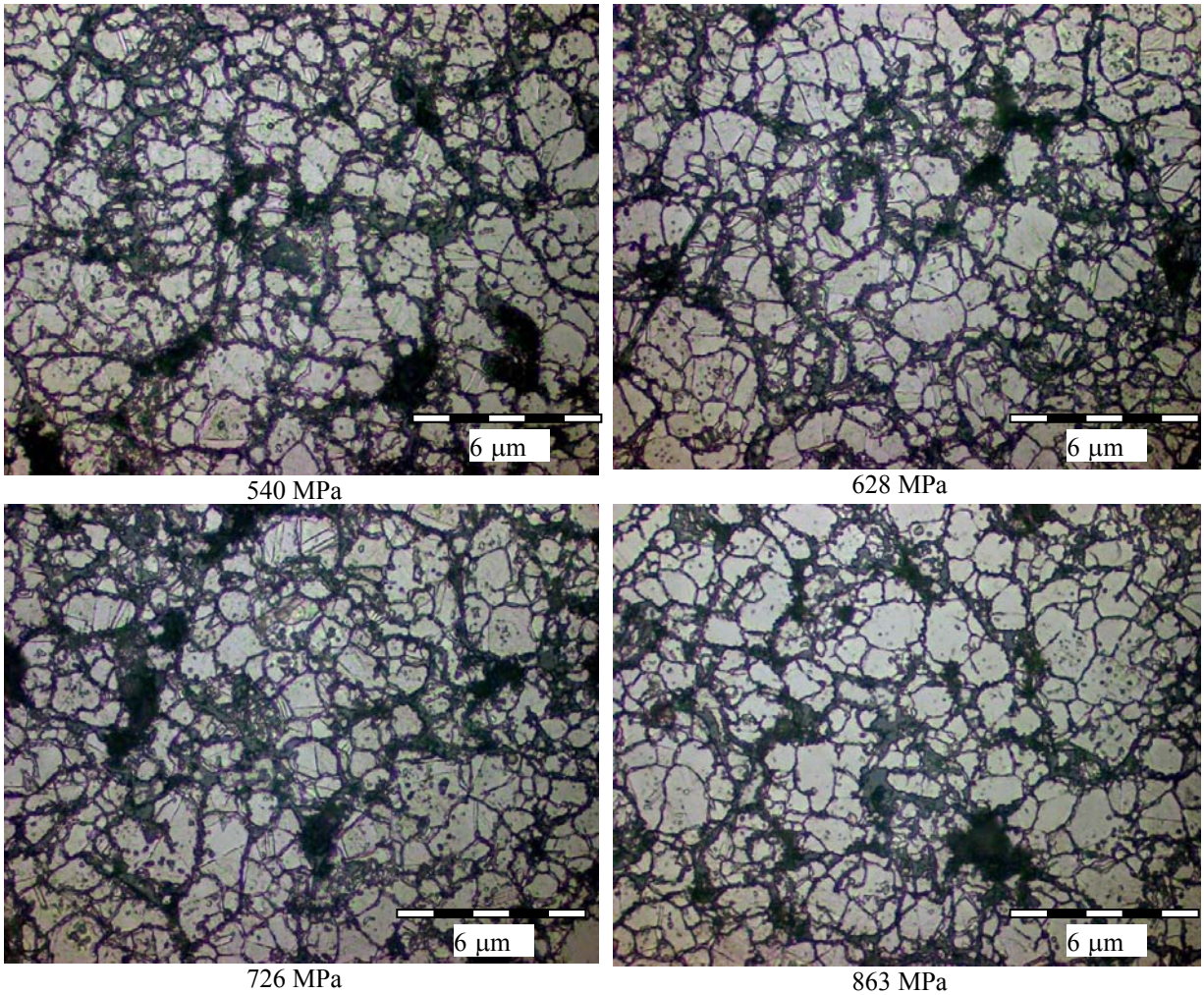

540 MPa 628 MPa

726 MPa 863 MPa

Fig. 4. *Microstructure of sintered 316 stainless steel, electrolyte attack, solution 50% HNO_3*

From Fig. 4 it can be seen that samples microstructure consists of austenite. The $HV_{0.1}$ microhardness determined on samples of sintered powder was $HV_{0.1}$ = 3120.2 MPa, Fig. 5. The 316 stainless steel sintered samples were subjected to wear test on rotary disk with sand paper.

The results, as average of three determinations, are presented in Table 1. Analyzing Table 1 and Fig. 6 one can say that 316 stainless steel powder is recommended to be pressed at pressures higher than about 863 MPa to ensure superior resistance to wear. Pressing at low pressure leads to a lower compaction which results in lower wear resistance. Sample porosity was determined by the linear segments method. Porosity variation vs formation pressure is presented in Fig. 7. It can be seen that with increased pressure porosity is reduced both in the middle of the samples and at their edge.

Wear variation vs average porosity is presented in Fig. 8. It can be seen that with decreasing porosity the wear resistance increases. In Fig. 9 – 12, 3D images are presented made with an Image J software, of the 316 powder sample areas obtained from the abrasive wear test.

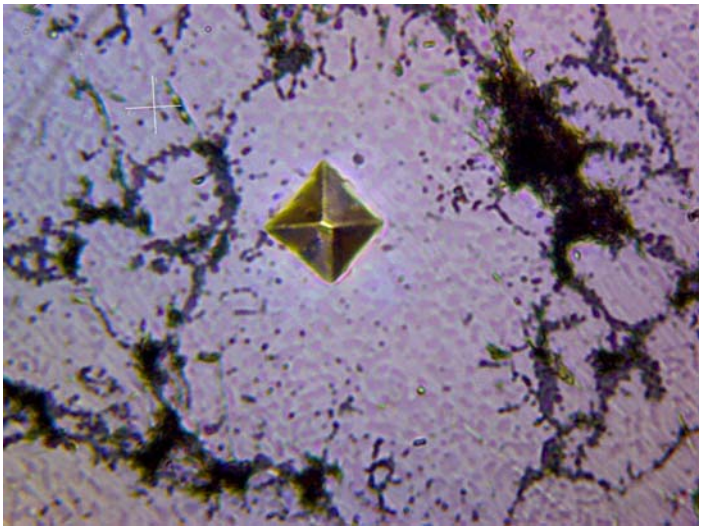

Fig. 5. *Determining microhardness of 316 stainless steel samples*

Table 1. *Abrasive wear behavior of sintered powder products*

Pressure	**Mass wear**	**Length run**	**Wear/ length run**
[MPa]	[g]	[m]	[g/m]
540	0.0141	11.6	0.001224
628	0.0122	11.6	0.001052
726	0.0117	11.6	0.001009
863	0.0113	11.6	0.000974

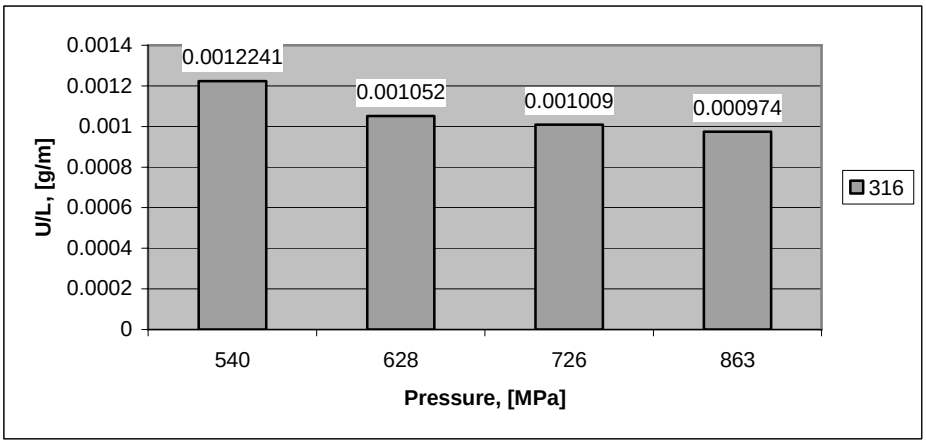

Fig. 6. *Abrasive wear behavior of sintered powder products*

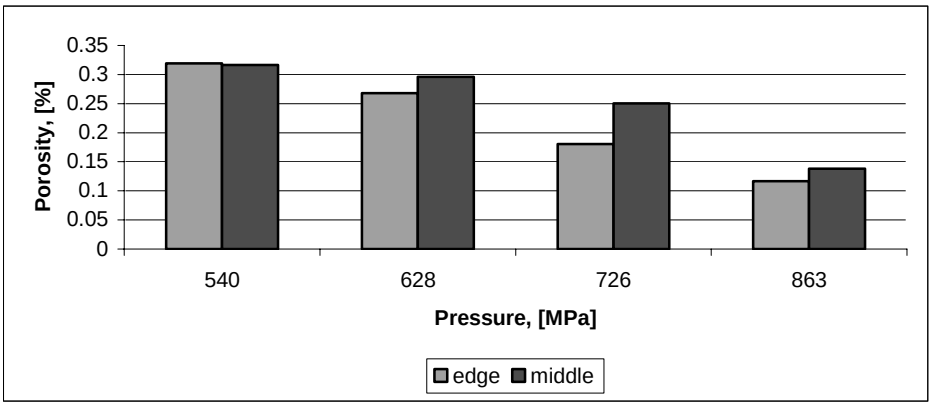

Fig. 7. *Porosity variation with formation pressure*

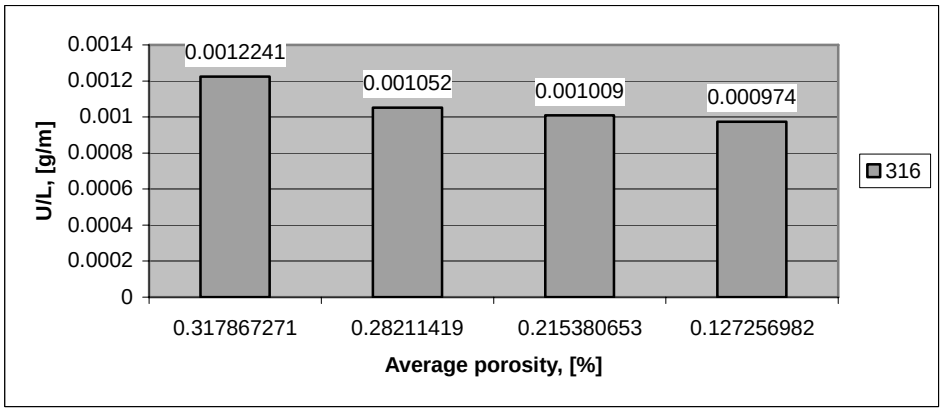

Fig .8. *Wear variation vs average porosity*

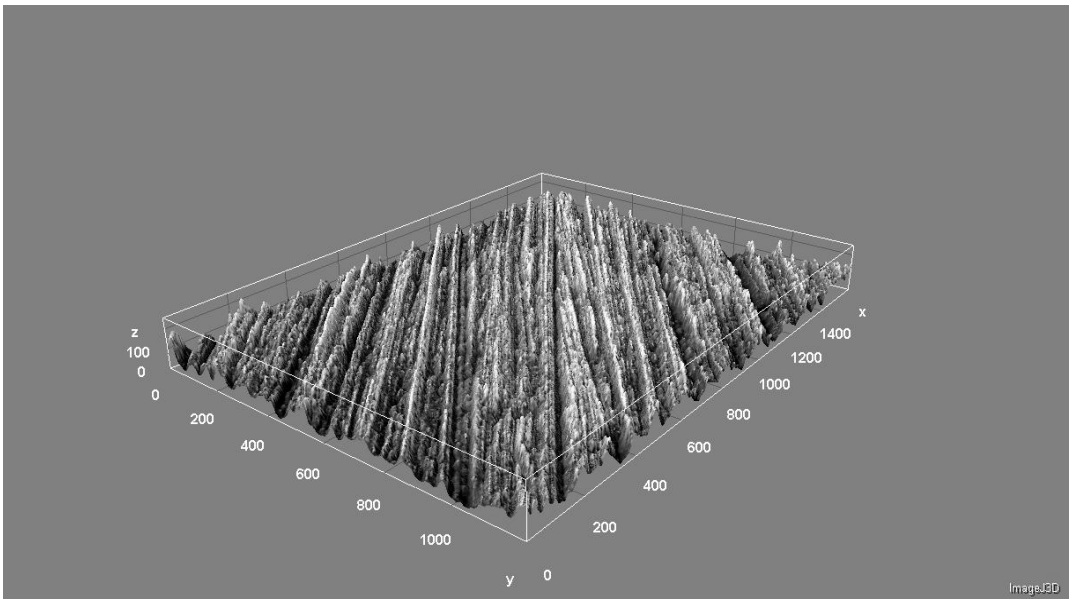

Fig. 9. *3D image of the sample surface pressed with 540 MP subjected to abrasive wear*

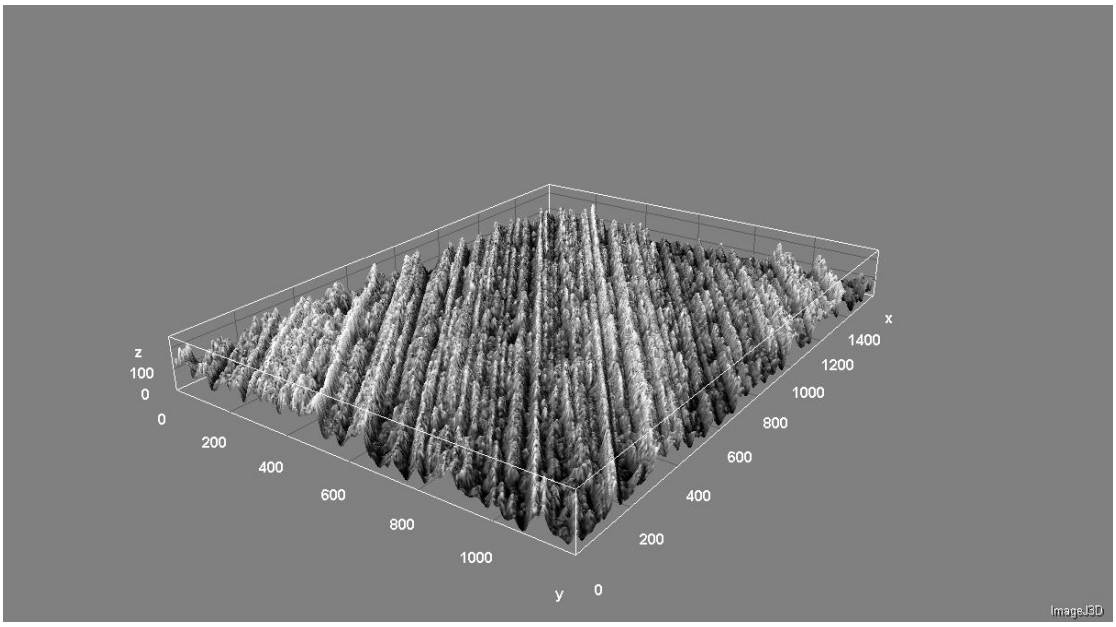

Fig. 10. *3D image of the sample surface pressed with 628 MPa subjected to abrasive wear*

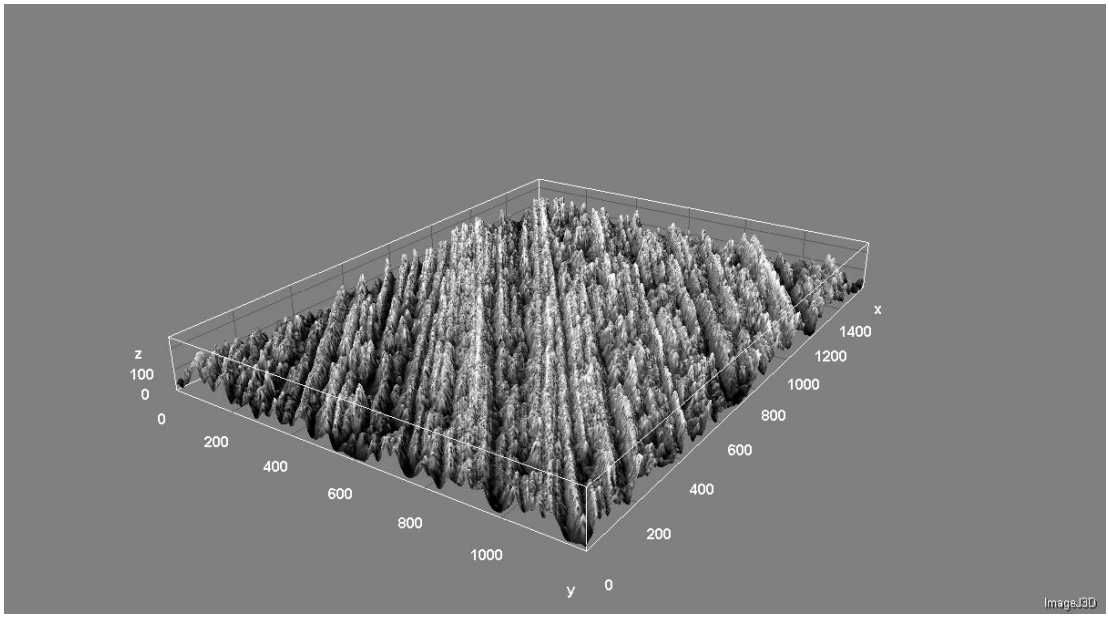

Fig. 11. *3D image of the sample surface pressed with 726 MPa subjected to abrasive wear*

Analyzing the previous images one can see good wear behavior of the samples pressed at higher pressures.

4. Conclusions

The production of 316 austenitic stainless steel powders revealed the following:

* the powder used in the experimental research has an irregular shape specific to water atomisation, being suitable for conventional compaction in mold and sintering at a theoretically higher density;

* the pressures used for 316 powder compaction were 540, 628, 726, 863 MPa;

* it was found that increased pressure leads to reduction in tablets porosity;

* sintering of powder tablets at 1150°C, for one hour has reduced their porosity;

*samples microstructure consists of austenite;

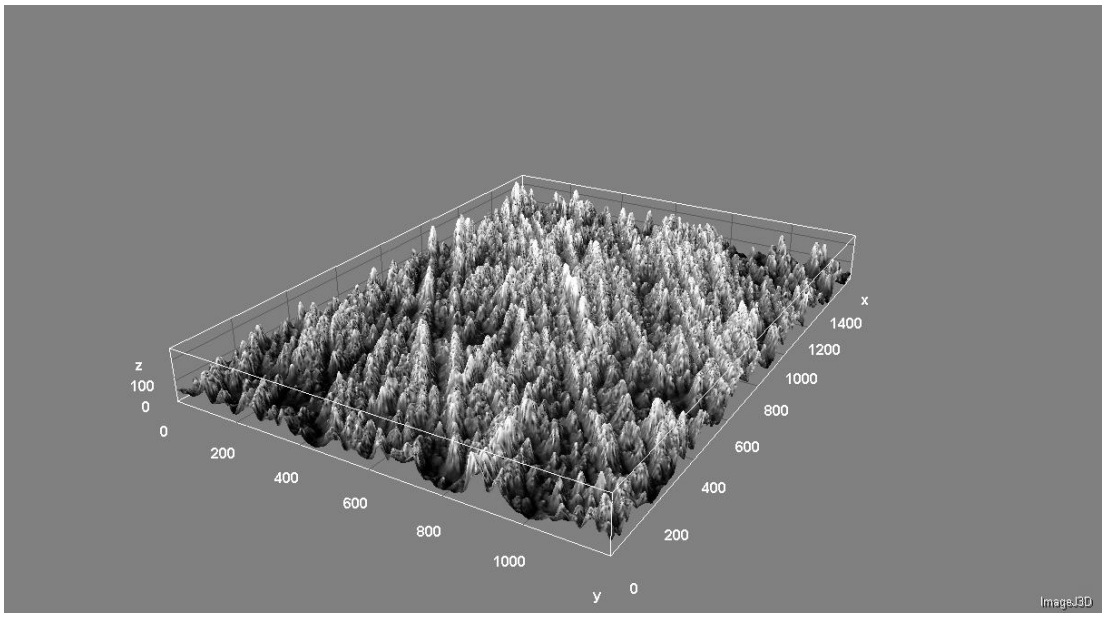

Fig. 12. *3D image of the sample surface pressed with 863 MPa subjected to abrasive wear*

* $HV_{0,1}$ microhardness determined on sintered powder tablets was HV 0.1 = 3120,2 MPa, higher than the initial state powder;

* as regardis the abrasive disk wear resistance it was found that 316 stainless steel powder is recommended to be pressed at pressures higher than about 863 MPa to ensure superior resistance to wear.

* pressing at low pressure leads to a lower compaction resulting in decreased wear resistance.

References

[1]. H. N. Ch'ng, J. Pan - *Modelling microstructural evolution of porous polycrystalline materials and a numerical study of anisotropic sintering*, J. Comput. Phys. 204, 430–461, Journal of Computational Physics, Volume 204, Issue 2, 20, (2005).

[2]. D. Bernard, D. Gendron, J. M. Heintz, S. Bordere, J. Etourneau, *First direct 3D visualisation of microstructural evolutions during sintering through X-ray computed microtomography*, Acta Materialia 53, (2005).

[3]. Y. V. Levinsky - *The Behavior of Closed Pores at the Final Stage of Sintering*, ISSN 1067-8212, Russian Journal of Non-Ferrous Metals, Vol. 50, No. 3, pp. 298–316. © Allerton Press, Inc., (2009).

[4]. Deleanu L., Ciortan S. - *Evaluating Tribological Damages by 3D profilometry,* EHD Lubrication and Traction, May 6-8, 2010 VAREHD 15, Suceava, Romania, http://www.varehd.usv.ro/, ISSN 1844-8917, pp. 163-169, (2010).

[5]. E. Drugescu, O. Potecaşu, F. Potecaşu, M. Marin, V. Mereuta, L. Deleanu - *Mechanical properties, abrasive wear behavior and surface quality evaluation of new sintered iron alloys*, Rotrib, Universitatea Tehnică „Gh. Asachi", Iaşi, Tomul LVII (LXI), Fasc. 1, (2011).

[6]. Deleanu L., Cantaragiu A., Ciortan S. - *Surface Quality evaluated by 3D Functional Parameters,* Proceedings of 10th Intern. Conf. "Research and Development in Mechanical Industry", RaDMI 16-19 September, Donji Milanovac, Serbia, pp. 311-318, (2010).

[7]. Palfalvi -*Metalurgia Pulberilor,* Editura Tehnică, Bucureşti, (1988).

[8]. T. Surdeanu, M. Perneş - *Piese sinterizate din pulberi metalice,* Editura Tehnică, Bucureşti, (1984).

[9]. Marshall D. - *Austenitic Stainless Steels. Microstructure and mechanical properties*, (1984).

[10]. *** - ASM Specialty Handbook, Stainless Steels, (2004).

THE ANNALS OF "DUNAREA DE JOS" UNIVERSITY OF GALATI.
FASCICLE IX. METALLURGY AND MATERIALS SCIENCE
N^0. 4 – 2012, ISSN 1453 – 083X

MECHANICAL PROPERTIES AND ABRASIVE WEAR BEHAVIOR OF FLUIDIZED - BED CARBURIZED SINTERED IRON ALLOYS

Mihaela MARIN, Florentina POTECAŞU, Elena DRUGESCU, Octavian POTECAŞU, Petrică ALEXANDRU
Dunărea de Jos University of Galati
email: mihaela.marin@ugal.ro

ABSTRACT

In this paper is studied the influence of fluidized bed carburizing of sintered steels on mechanical properties and abrasive wear behavior for two different types of powder. Carburizing was carried out at temperature of 900° C and maintining time of 20 minutes, respectively 40 minutes. It was found that the best values for Vickers microhardness and abrasive wear were recorded when carburizing time is 40 minutes for powder P_2.

KEYWORDS: powder metallurgy, sintering, fluidized bed carburizing, abrasive wear

1. Introduction

Powder metallurgy (P/M) is a technology providing an alternate with lower costs process comparing with other metal technologies.

Powder metallurgy's markets for this parts are varied, the automotive applications are dominated.

Iron powder accounts around 90% of the total world powder production and is the most common form of powder in manufacturing, mostly in the auto industry [1- 4].

The four basic stages of powder metallurgy are: powder manufacture, powder mixture, pressing and sintering (Fig. 1).

Sintering is the process of compaction, consolidation by heat treatment of a part. Is a complex process, with physical and physicochemical phenomena that success or overlap [4]. The mechanisms involved in the transport of material to sintering are surface, intergranular and volume diffusion.

The properties of sintered materials are determined, in first step by the nature of the material's characteristics for powders involved, and secondary by pressing and sintering process parameters [5].

Mechanical properties can be improved on increasing the density, reducing the pore size or by applying an thermochemical treatment (carburizing, nitriding, boriding) [6-7].

Carburizing consists in a surface carbon enrichment, which gradually decreases towards the core [8-14].

In this paper, the mechanical porperties and abrasive wear behavior of carburized in fluidized bed sintered steels are analyzed. The abrasion tests were conducted under constant load and speed conditions.

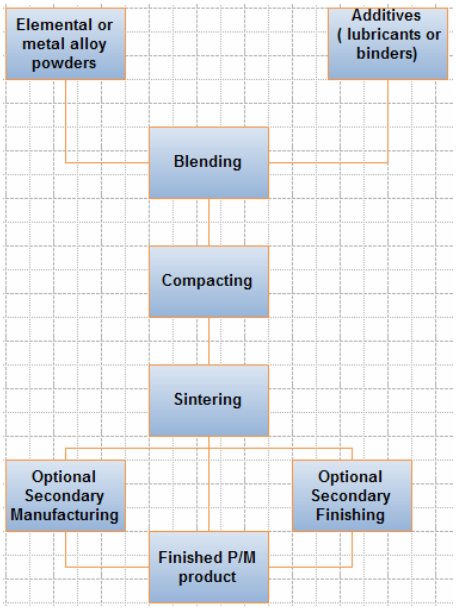

***Fig. 1**. Powder Metallurgy Process*

2. Experimental procedure

2.1. Materials

Specimens prepared from atomized iron powder and from pre-alloyed iron base powders were analyzed in this paper.

The chemical composition of the powder samples, pure iron and iron-based prealloyed powder with Cu, Ni and Mo is presented in Table 1. To evaluate the mechanical properties, a die for making the samples in the form of a cylinder was produced. The samples were used to evaluate mechanical properties such as Vickers microhardness and abrasive wear.

Table 1*.Chemical composition of analyzed powders (wt%)*

Powder type	Cu	Mo	Ni	C
P_1	0.096	0.008	0.046	<0.01
P_2	1.50	0.50	1.75	<0.01

The powders were mixed with 1% zinc stearate. The samples were compressed in a universal mechanical testing machine to a pressure of 600 MPa, the dimensions of disc specimens are $\phi 8 \times 6$mm. In figure 2 is the picture of the sample.

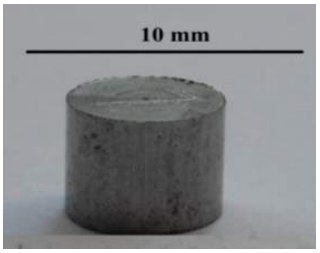

Fig. 2. *Aspect of sintered sample*

The green samples were sintered in a laboratory furnace, within a controlled atmosphere. The sintering temperature was approximately 1.150 °C and the sintering time was 60 min with a heating rate of 30-40 °C/min.

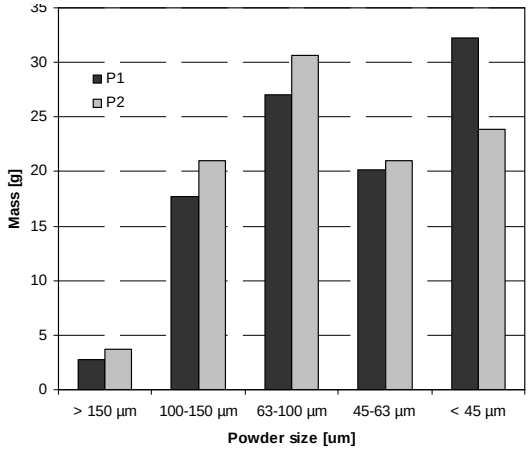

Fig. 3. *Size distribution of analyzed powders*

All the samples were kept in the furnace for slow cooling to room temperature. The microstructure depends on the amount of sintered carbon and cooling rate.

Before the sintering temperature is reached, the parts were maintained during 30 min at 500 °C to burn lubricant, respectively zinc stearate.

After cooling to room temperature the samples were carburized-treated. In Figure 3 is presented the size distribution of the analyzed powders. Treatment conditions for the fluidized bed carburizing process were heating at 900°C during 20 and 40 minutes. Specimens were then air-cooled to room temperature.

The carburized layer depth is a function of carburizing time and carbon potential available surface [10]. When carburizing times are increased, deep carburized layers are obtained, which can lead to a structure consisting of residual austenite in excess or free carbides. These two microstructural elements have adverse effects on residual stress distribution in the layer. Therefore, a high carbon potential may be suitable for short carburizing times, but not for increased carburization. In this study, it appears that only the carburized sample with 40 minutes is showing the carburized layer. The microstructure of carburized samples was observed by optical microscopy (Olympus BX 50). Photomicrographs were obtained at a magnification of 200X.

2.2. Abrasion wear tests

Samples subject to fluidized bed carburizing were tested for abrasion wear test (Fig. 4). The SiC particles on the abrasive papers were the size of 80µm and the load applied was 855g. The distance traversed in each case was limited to 150 cycles, corresponding to 76.5 m.

Fig. 4. *Aspect of worn surface after the abrasion test*

The samples were subjected to circular motion over the wheel on which the abrassive paper was stuck.

The abrasion test process included the stepts: first, fixing the abrassive paper on the wheel.

Then, the samples of known weight were loaded on the machine and then was applied the load and finally, the samples were cleaned and weighed prior to and after each test interval. After the tribological tests, the worn surfaces were examined by optical microscope, in order to identify the dominant wear mechanisms.

2.3. Mechanical properties

The carburized in fluidized bed samples were analyzed according to their mechanical properties. The microhardness tests were performed by measuring Vickers microhardness, and the test parameters are: the penetrator is a diamond pyramid diameter and load of 100g.

The microhardness was the average of three indentations on the top and another on the bottom surfaces of the samples.

3. Results and discussion

3.1. Microstructure

Optical micrographs representative of carburized samples are presented in figures 5 and 6. Microstructural analysis shows uniform structures with specific components of steel depending on difussion carbon content.

Most alloying elements moves the S point to the left of the Fe-C diagram, it means that powder is increasing the carbon content by applying thermochemical treatment in fluidized bed. Carburizing can reached at the surface eutectiod or hipereutectoid steel structures (pearlite and cementite).

This distribution of structures explains the major hardness of carburized superficial layer.

3.2. Tribological tests

The worn surfaces of carburized samples after abrasion tests were examined in optical microscope, the typical aspects of abraded surfaces are represented in figures 7 and 8.

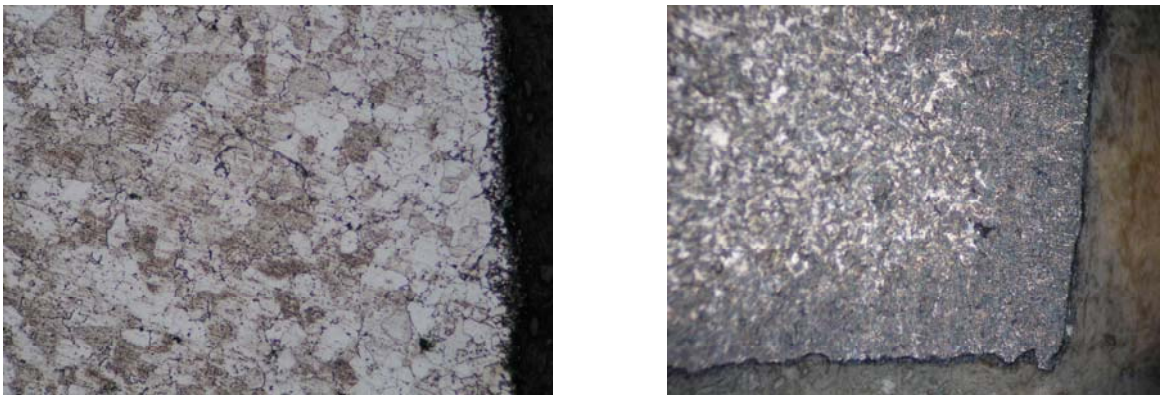

a) b)

Fig. 5*. Microstructures of sample carburized (powder P_1) at 900° C: a) 20 minutes (200x), b) 40 minutes (200x), etched Nital (2%)*

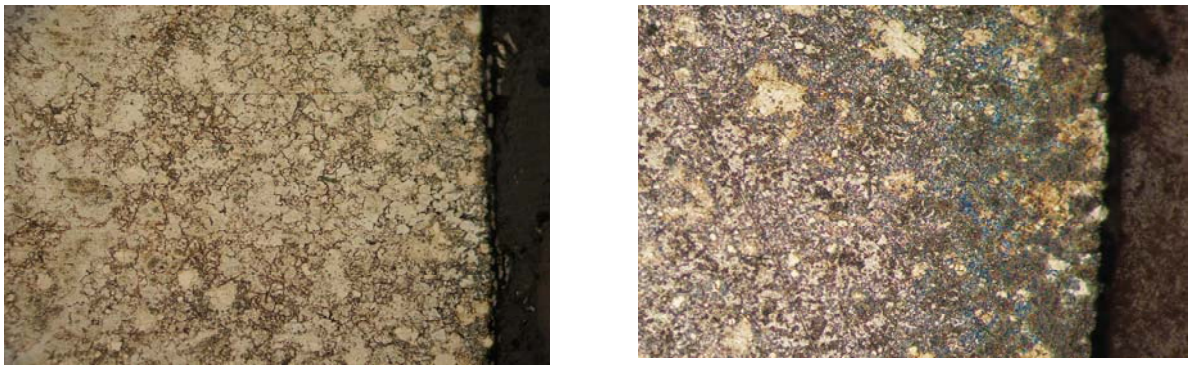

a) b)

Fig. 6*. Microstructures of sample carburized (powder P_2) at 900° C: a) 20 minutes (200x), b) 40 minutes (200x), etched Nital (2%)*

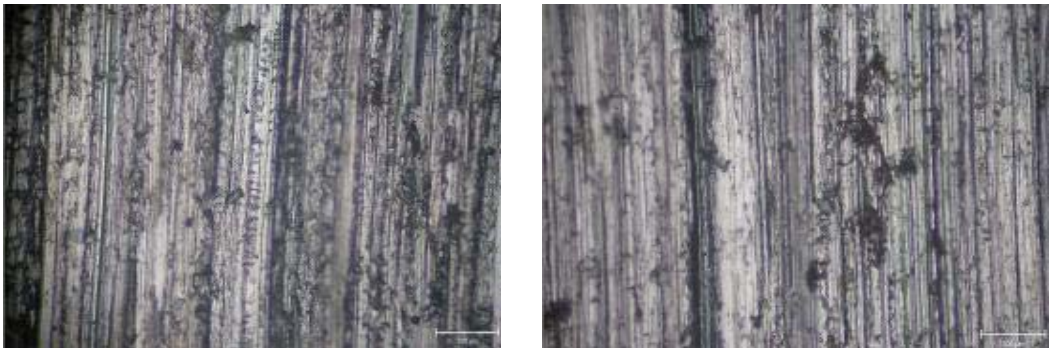

a) b)

Fig. 7. *Optical photomacrographs of worn surfaces for carburized samples at T= 900°C, 20 minutes. (x200): a) P_1, b) P_2*

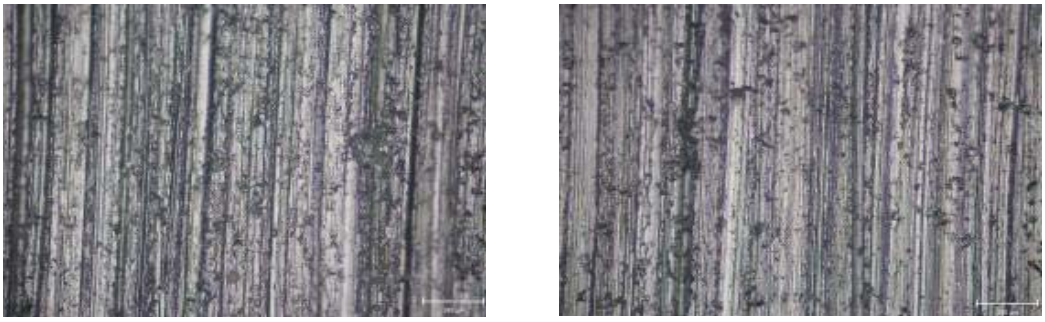

a) b)

Fig. 8. *Optical photomacrographs of worn surfaces for carburized samples at T= 900°C, 40 minutes. (x200): a) P_1, b) P_2*

Figures 9 and 10 show microhardness values for carburized treated samples studied. It is found that samples carburized for 40 minutes have proximate values of Vickers microhardness. The depth and width of wear grooves of carburized samples P_1 are greater compared to samples P_2.

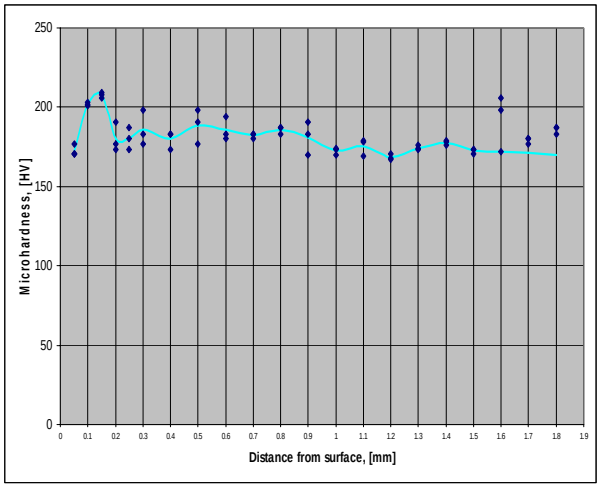

Fig. 9*. Microhardness variation from surface to the center for carburized sample (powder P_1) at T= 900°C, 40 minutes*

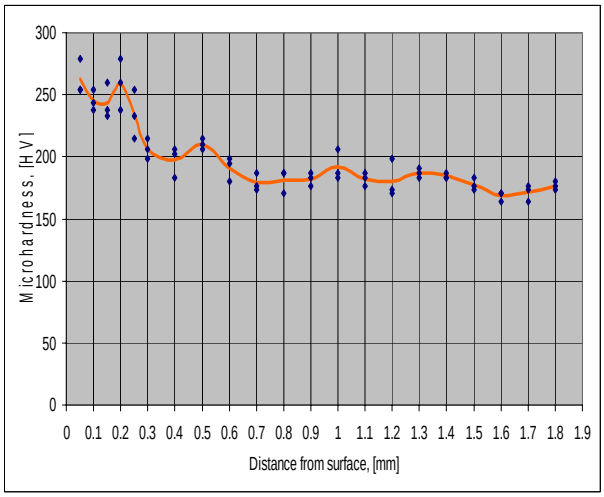

Fig. 10*. Microhardness variation from surface to the center for carburized sample (powder P_2) at T= 900°C, 40 minutes*

4. Conclusions

According to the experimental results in this study, the following conclusions may be discussed:

- The best microhardness values were recorded when the sample was carburizing at 900° C for 40 minutes, especially for powder P_2.

- Carburized layer depth is a function of carburizing time and carbon potential available surface.

- Abrasive wear surfaces for two types of powders presents deeper traces in unalloyed samples and finer trace in samples alloyed P_2, as subsequently wear tests giving results in conformity with these aspects of the surface.

- The carburized sample P_1 presents a depth and width of wear grooves greater, thus there is a possibility of less resistance offered.

- The carburized samples P_2 present a much smaller wear groove width much less, that can asssure a good resistance.

References

[1]. K.V. Sudhakar - *Fatigue behavior of a high density powder metallurgy steel*. Int J Fatigue, (2000), 22:729–34.

[2]. G.B. Jang, M.D. Hur, S.S. Kang - *A study on the development of a substitution process by powder metallurgy in automobile parts*, J Mater Process Technol, (2000), 110–5.

[3]. V. B. Akimenko, I. A. Gulyaev, O. Yu. Kalashnikova, M. A. Sekachev - *The Prospects for Russian Iron Powder*, Central Scientific-Research Institute of Ferrous Metallurgy, Vol. 37, No. 5, p. 472–476, ISSN 0967-0912; (2007).

[4]. K.S. Narasimhan - *Sintering of powder mixtures and the growth of ferrous powder metallurgy*. Mater Chem Phys, (2001), 67:56–65.

[5]. C. Anayarana C, E. Ivanov, V.V. Boldyrev - *The science and technology of mechanical alloying*. Mater Sci Eng A, 304–306:151–8, (2001).

[6]. J. Georgiev, T. Pieczonka, M. Stoytchev, **D. Teodosiev** - *Wear resistance improvement of sintered structural parts by C_7H_7 surface carburizing*, Surface and Coatings Technology, volumes 180-181, Pages 90-96, (2004).

[7]. Hadrian Djohari, JorgeI Martínez-Herrera, Jeffrey J. Derby - *Transport mechanisms and densification during sintering:I.Viscous flow versus vacancy diffusion*, Department of Chemical Engineering and Materials Science, MN55455-0132.

[8]. G. Krauss, *Microstructure residual stress and fatigue of carburized steels*, in: Proceedings of the Quenching and Carburizing, The Institute of Materials, pp. 205–225, (1991).

[9]. G. Krauss - *Principles of Heat Treatment of Steels*, American Society for Metals, pp. 251.

[10]. M. Askaria, H. Khorsand S. M. Seyyed Aghamiric - *Influence of case hardening on wear resistance of asintered low alloy steel,* Journal of Alloys and Compounds Volume 509, Issue 24, 6800-6805, (2011).

[11]. S. Mansoorzadeh, F. Ashrafizadeh - *The effect of thermochemical treatments on case properties and impact behaviour of Astaloy CrM,* Surface and Coatings Technology, Volume 192, Issues 2-3, Pages 231-238, (2005).

[12]. J. Kazior, C. Janczur, T. Pieczonka, J. Ploszczak - *Thermochemical treatment of Fe–Cr–Mo alloys,* Surface and Coatings Technology, Volumes 151-152, 1 March 2002, Pages 333-337.

[13]. I. D. Radomysel'skii, A. F. Zhornyak, N. V. Andreeva, G. P. Negoda - *The pack carburizing of dense parts from iron powder,* Powder metallurgy and metal ceramics, Volume 3, 204-211.

[14]. O. I. Pushkarev, V. F. Berdikov - *Increasing the wear resistance of equipment in pressing parts from high-hardness powder materials,* Refractories and industrial ceramics, Volume 39, Numbers 9-10, 326-328, DOI: 10.1007/BF02770594.

THE ANNALS OF "DUNAREA DE JOS" UNIVERSITY OF GALATI.
FASCICLE IX. METALLURGY AND MATERIALS SCIENCE
N^0. 4 – 2012, ISSN 1453 – 083X

ASPHALT PAVEMENT AND ENERGY COLLECTION

Adrian VASILIU, Daniela Laura BURUIANA
"Dunarea de Jos" University of Galati
email: adrian.vasiliu@ugal.ro

ABSTRACT

Romania, as an EU member state is bind to appraise and disseminate accurate and updated information about quantities, types, sources, production, transformation and consumption of energy in order to monitor the impact and consequences of its energy policy. The energy statistics, which were traditionally focused on the energy supply and fossil energy, need to be developed in order to ensure better knowledge and monitoring of renewable energy sources, according to targets set by Directive 2009/28/EC. In Romania so far, no one was interested in putting into practice this idea and has been no study in this respect. This paper aims at conducting laboratory experiments on samples similar to asphalt structure deposited over the public roads in Romania, for energy recovery.

KEYWORDS: energy, efficiency, asphalt, recovery

1. Introduction

Of all land passageways, roads have their beginnings in ancient times, being for thousands of years the only means of communication between people, for their own movement and transport of goods among inhabited areas. From antiquity until today, roads have developed differently depending on both economic and social levels and also on the degree of civilization of each era.

The emergence of the motorcar will lead to a new boom in road engineering, increased number of motor vehicles, directly affecting the design, construction and maintenance of roads. Human life can not be conceived but dynamically in space and time, the need to move to ensure existence being an essential component of an organized society. This, in its evolution, has always needed communication routes as intrinsic mediator of trade, cultural, goods or persons exchanges.

Romania has a high attractiveness for investments in road infrastructure and implementation of techniques and solutions for generating thermal energy accumulated in roads and highways covered with asphalt.

2. Objective

This paper aims at conducting laboratory experiments on similar samples similar to the road asphalt coat structure for the study of the heat exchange and accumulated thermal energy recovery. To exploit the heat energy of the asphalt, it is proposed to place water –filled metal pipelines under the asphalt. The water in the pipes receives the heat accumulated from asphalt and can be further used in a heat exchanger to supply hot water for domestic use, offices, industrial areas or can be converted into electricity.

Asphalt road construction materials are used to provide a road coat able to bear the burden of road traffic vehicles and transferred it in a dispersed form to the road foundation/base [1].

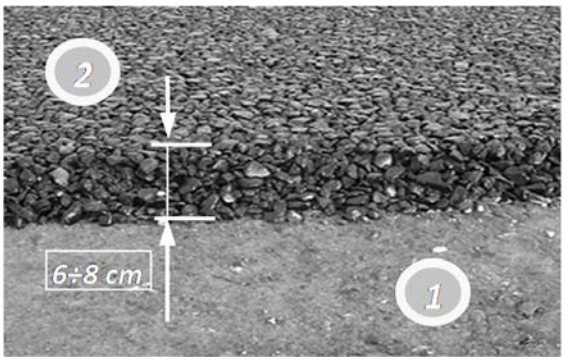

***Fig. 1**. Base and link layers[1]*
1-ballast foundation; 2-asphalt mixture

The main types of construction materials are binder and aggregates. (Fig.1). Depending on the binder used, road layers are classified as rigid (cement) and flexible (bitumen). The running layer 1 of the asphalt road structure is composed of bitumen

(5÷10%) and granular mineral aggregates (gravel, quality rock, sand).

Energy generated by the sun is the most important and reliable resource of all renewable energy sources currently exploited. This also represents an inexhaustible source of energy for humans, especially due to its energy being clean, uncontaminated. The solar radiation reaches the Earth's surface as direct solar radiation and diffuse solar radiation due to Earth's atmosphere.

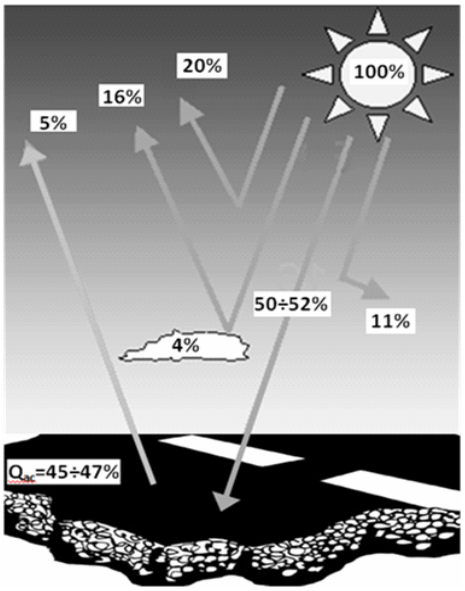

Fig. 2. *Distribution of solar radiation*

The global radiation received from the Sun, on a horizontal surface at ground level on a cloudless day, consists of the sum of the two radiations. Absorbed radiation is generally converted into heat and diffuse radiation is returned to all directions in the atmosphere. (fig. 2).

The reduced temperature will extend the life of the pavement, while the reduced temperature of the near surface air will lead to savings in energy consumption of adjacent buildings and improvement in air quality (such as by reducing ozone concentration).

3. Working method

Samples were made in wooden boxes (photo 1) by depositing successive layers of materials while complying with the quality and height requirements. Between the base layer and the granular mineral aggregates a metal coil (photo 2) was covered with asphalt (photo 3, 4).

Photo 1.
Box manufacturing

Photo 2.
Coil location

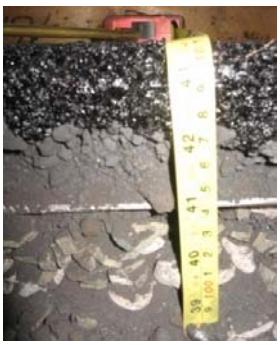

Photo 3, 4. *Laying the asphalt coat*

In the laboratory, the asphalt samples were exposed to heating by a radiator (photo 5) fitted with a variable voltage device so that it could be established a steady temperature by loss compensation. Water in the system is circulated through the metal coil located under the carpet of asphalt and a buffer tank by a pump driven by an electric motor controlled by a thermostat (photo 6).

Photo 5
Electrical heater

Photo 6
Water buffer tank

The temperatures T1 at the sample surface (photo 7) at 5 cm depth into the asphalt T2 (photo 8) and of the water T3 (photo 9) in the buffer tank were measured from the beginning of asphalt heating until a stationary temperature was reached.


Photo 8, 9 *Location of thermometers*
The asphalt surface *The water tank T3*

4. Laboratory measurements

Transport of the accumulated heat energy in the asphalt layer to the coil is carried out by conduction and from the coil wall to the water circulated by a pump to the buffer tank (active system), by convection.

After establishing a steady temperature between the heat emitted by the radiator and the heat accumulated in the asphalt sample at a distance of 30, 35 and 40 cm so that the surface temperature be constant temperatures T2 and T3 are measured at intervals of about 30 minutes until the water temperature remains constant.

Table 1. *Notations and calculation relations*

Denomination	Symbol	Value	Measure unit
Distance from resistance to asphalt surface	H	$(35, 40, 4)\cdot10^{-3}$	[m]
Thickness of asphalt layer, (photo 4)	x	Measured = $50\cdot10^{-3}$	[m]
Coil diameter	d_s	Measured = $5\cdot10^{-3}$	[m]
Coil heat exchange surface	s_s	Calculation = $6.863\cdot10^{-3}$	[m^2]
Asphalt surface	S_{asf}	Calculation = $2.925\cdot10^{-3}$	[m^2]
Asphalt volume	V_{asf}	Calculation = $0{,}146\cdot10^{-3}$	[m^3]
Thermal conductivity [8], [9]	$\lambda_{asph.}$	0.75÷0.9	W/(m.K)
Density [8], [9]	$\rho_{asph.}$	2640	Kg/m^3
Specific heat capacity [8], [9]	$c_{asph.}$	385	J/(kg.K)
Resistors voltage	U	Measured = 220	[V]
Intensity of resistance current	I	Measured = 1,88	[A]
Resistor temperature	T_R	Measured = 1100	[^{0}C]
Ambient temperature	T_0	Measured = 15	[^{0}C]
Stefan Boltzmann's constant [8]	σ_0	$5.67\cdot10^{-8}$	W/(m^2.K^4)

5. Calculation of heat exchange efficiency

Resistor radiation (t=1hour):

$$Q_{rez} = U \cdot I \cdot t = 413.6\,[Wh] = 1488960[J] \quad (1)$$

Heat transmitted by radiation:

$$Q = \varepsilon_{red} \cdot \sigma_0 \cdot \left[(T_{rez})^4 - \left[(T_1)^4\right]\right] s_{box} \cdot 3600\,[J] \quad (2)$$

The transfer of energy by electromagnetic waves through empty space is called radiation heat transfer. Energy can be transferred by thermal radiation between a gas and solid surface or between two or more surfaces [9].

Heat transmitted by conduction asphalt:

$$Q_{c,asph} = \frac{\lambda}{x} \cdot (T_1 - T_2) \cdot s_{box} \cdot 3600 \quad [J] \quad (3)$$

The heat transfer by conduction is the energy transfer through a substance, a solid or a fluid as result of the presence of a temperature gradient within the substance [9].

Heat accumulated in asphalt:

$$Q_{c,asph} = m_{asph} \cdot c_{asph} \left(\frac{T_1 + T_2}{2} - T_0 \right) \quad [J] \quad (4)$$

Heat flow transmitted by convection:

$$Q_c = \alpha_c \cdot (T_2 - T_3) \cdot s_s \cdot 3600 \quad [J] \quad (5)$$

The heat transfer by convection is the energy transfer between a fluid and a solid surface. Heat transfer by convection is more difficult to analyze than the heat transfer by conduction because it varies from situation to situation upon the fluid flow conditions. In practice, the heat transfer by convection is treated empirically [9].

Heat amount from the water (m_a = *4kg*) in the vessel:

$$Q_{water} = m_w \cdot c_w \cdot (T_3 - T_0) = 231012 \quad [J] \quad (6)$$

Exchange output/efficiency:

$$\eta = \frac{Q_{rez}}{Q_{water}} \cdot 100 = 15.51\,\% \quad (7)$$

Efficiency is calculated 15.51%, large losses of approximate 35% are produced by convection from the radiator to sample asphalt. The efficiency of the pavement - heat exchanger system in transmitting the heat from the pavement to the fluid inside the system of pipes depends on a number of factors, including:

1. The pavement surface actually collects the incident solar radiation. If it is a highly reflective surface (high albedo) then very little heat will be absorbed and be available for harvesting. If on the other hand, the absorptivity is increased (say by painting the surface black), then we will have more heat energy to harvest.

2. The function of the pavement materials depend on their location with respect to the heat exchanger system. For the materials in the layers above and around the heat exchanger system, the ideal function should be to transmit the heat (or conduct the heat, more approximately) in the most efficient manner. The function of the materials in the layer beneath the heat exchange system should be to insulate the system from the bottom layers, such that very little heat can be transmitted through the bottom layers.

3. The material of the heat exchanger system (which consists of pipes) should have a high conductivity and the layout should be such as to allow the exposure of the pipes to the pavement for sufficient length to allow the fluid to reach the maximum temperature achievable in the system.

4. The initial temperature of the fluid (that is the temperature of the fluid as it enters the heat exchanger system) should be low enough, in comparison to the temperature of the pavement, such that the there is significant difference between the two, and hence a significant rate of flow of heat into the fluid.

6. Measured values

Based on measurements made in a period of 2 hours and three different cases, with variations of radial distance and sample asphalt (H) and obtained results were presented in the tables 2÷4.

Resistor height H1 =35·10^{-3} m

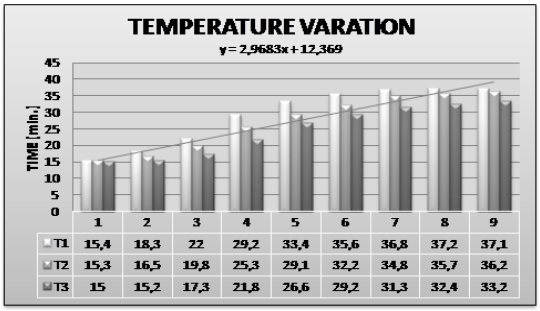

Graphic 1. *Heating up to the stationary temperature H1*

Resistor height H2=40·10^{-3} m

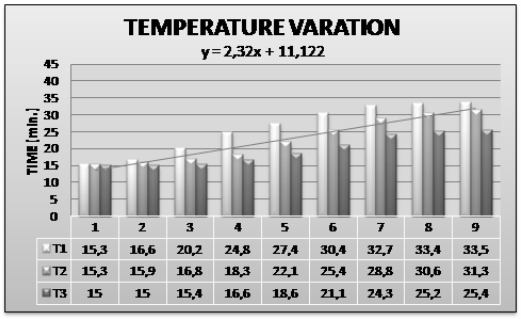

Graphic 2. Heating up to the stationary temperature H2

Resistor height H3=45·10^{-3} m

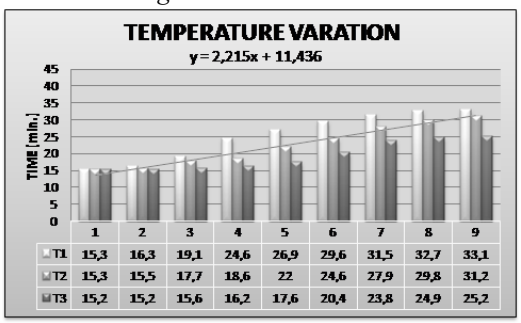

Graphic 3. Heating up to the stationary temperature H3

These were processed resulting graphs with a linear variation of temperature in the three points T_1, T_2 and T_3.

The temperature at any depth of the pavement depends on the pavement materials and the surface temperature, which depends on a number of factors including the location, surface, the wind speed and the cloud cover.

Based on available models, pavements temperatures at different depths can be predicted throughout the year.

7. Conclusions

The road infrastructure in Romania is poor, which calls for major investments in this sector and development in the future.

Construction of public asphalt roads is based on the use of specific materials, such as binder and aggregates, deposited in successive layers.

The important cost considerations are those that are needed for the installation of the system –labor and materials, for piping and pumping, as well as for the end application (for example, a turbine, if the generation of electricity is required), and maintenance of the system. The payback period can be estimated

by calculating the savings in energy consumption, and/or selling of excess energy to a grid.

References

[1]. * -** http://en.wikipedia.org/wiki/ Asphalt_base.jpg.
[2]. *** - www.cnadnr.ro/ Compania Naţionala de Autostrăzi şi Drumuri Naţionale din România.
[3].*-** Monitorul Oficial Partea I nr. 323 din 14/04/2004, Normativ, privind reciclarea la cald a îmbracămintelor rutiere bituminoase.
[4]. Kelemen G. & Ursa D. - *Argumente in favoarea utilizării energiei solare*, Rev. Tehnica instalaţiilor nr. 5/2003.
[5].*** - http://re.jrc.ec.europa.eu/pvgis/ Solar radiation maps - Europe [RO].
[6]. * -** www.Engineering ToolBox.com "Thermal Conductivity"
[7]. Anca C-tin - *Termotehnică*, Ovidius University Press, Constanţa, (2002), (course) ISBN 973-614-052-0.

THE ANNALS OF "DUNAREA DE JOS" UNIVERSITY OF GALATI.
FASCICLE IX. METALLURGY AND MATERIALS SCIENCE
N^0. 4 – 2012, ISSN 1453 – 083X

CHOOSING AND USING RATIONALLY THE THERMIC PROCESSED STEELS

Octavian POTECAŞU, Florentina POTECAŞU
Center of Nanostructures and Functional Materials, "Dunărea de Jos" University of Galaţi
email: opotec@ugal.ro

ABSTRACT

On a global scale one can notice a constant preoccupation for a rational choosing and using of the materials on the whole and, especially of the steels with the main objective the increase of the machines', equipment' and constructions' efficiency and competitiveness. An important issue that contributes, for example, to the choice of the "ideal" brand of steel for a piece, is the availability of a right equipment to produce a thermal processing under control. The research looked for the influence of the carbon content on the one hand, and of the vanadium on the other hand (as a micro alloying element), on the mechanical characteristics and the structure for four series of materials (21VMoCr14, 34 MoCr11, 40 VMoCr11 si 42 MoCr11), which undertook different types of thermal processing.

KEYWORDS: steel, thermal processing, mechanical characteristics, microstructure, efficiency

1. Introduction

The quality of the metallic materials used for producing a product together with the layout design and the manufacturing technology, contributes to the level of the technical, economical performances that it can achieve. Thus, today it is a continuous increase of how to use rationally the materials worldwide as a whole and especially the use of the steels. The main objective is the increase in efficiency and competitiveness of the machines, equipment and constructions.

A rational usage of a metallurgical product for a certain field is a complex issue, and it generally means assigning the steel brand that has the minimum resistance and endurance requirements of the piece for a minimum price. Any tendency to ensure superior materials as to the minimum requirements is harmful from an economic point of view and it does not contribute to increasing the machines' technical performances out of which the respective piece is part of. In our country the steel brands and the products intended to be used in the main fields of the national economy are standardized. Using other materials than those standard is forbidden by law. In order to fulfill with these materials the economy needs' it has grown a relatively wide range of standardized steels, which can sometimes lead to an inefficient marketing of steel brands and products, whose usage is scanty in real life and so they are difficult to buy.

Creating a steel brand in the siderurgical industry is usually made in high capacity plants. Answering to a small quantity request, requires either using from stock-piles, which usually are in a limited range of dimensions and it leads to higher metal consumptions, or waiting until these requests taken to the producer who decides to produce casts with the respective requirements. This can frequently be met in the case of the steels for thermal treated pieces. It is considered to be useful to anticipate, on groups of machines constructions, the limited range of steel brands and recommended products to be used. When choosing these steel brands one has to take also into account the perspective economic materials and, when choosing for a given case the routine should be avoided.

The maximum exploitation of the technological properties of the siderurgical product requires that the steels have adequate technological properties, according to the specific technologies from the machines' construction industry. The most important are: the weldability, the behavior to thermal treatment, the aptitude for plastic deformation, etc. Often enough these proprieties are antagonistic to those of resistance, and so it appears as necessary to establish an optimum compromise. For instance, any steel is weldable in certain conditions, but it should be avoided welding those steels to which these operations as well as the necessary thermic treatments and the subsequent quality controls are expensive or

the quality factor of the welding is relatively low. This is why the steels with a better weldability are to be preferred in these cases and it ensures a welding thorugh efficient procedures. This way, even if the material has lower resistance characteristics, the minimum requirements asked for the respective market are met. An important factor that, for instance, contributes to the choice of the "ideal" steel for a piece, is the availability of the right equipment for thermal treatment. Neglecting this aspect leads most of the time to unnecessary expenses, caused either by the use of an expensive material, or by producing scrap materials due to decarburation, ruptures, excessive deformation, etc.

2. Experimental

The influence on content of the carbon as well as the vanadium was studied in the research (as an micro alloying element) on the mechanical characteristics and the structure for four series of materials with 0.2%, 0.3%, 0.4%C, on which different types of thermal treatments were applied (classic brands, known according to the STAS rules as steels 21VMoCr14, 34 MoCr11, 40 VMoCr11 and 42 MoCr11). The chemical composition, guaranteed by the producers was confirmed also by the laboratory chemical analysis made on the DV-6 spectrometer.

The mechanical proofs were made at the room temperature according to the applicable standards SR EN 10002/1:2002 (traction assay) and SR EN 10045/1:1993 (the bending assay through jolt).

The assay series to be studied were put under the following thermal treatments: normalization (N), quenching (C), quenching + high annealing (C+RI), quenching + medium annealing (C +RM), quenching + low annealing (C+RJ) and annealing (R), after which the metallographic structure was analyzed and the corresponding mechanical characteristics to each quality of material was determined. For this the following assays were made at the room temperature: the traction assay, according to SR EN 10002/1 and the bending assay through jolt according to SE EN 10045/1, on samples ISO –V.

We should say that this experimental program was fully kept after each thermal treatment applied to the samples.

3. Results and Discussion

For all of the four types of steel, depending on the applied thermal treatment, are comparatively presented the mechanical characteristics' values for each of the four series of materials in the histograms below (fig1…. Fig5).

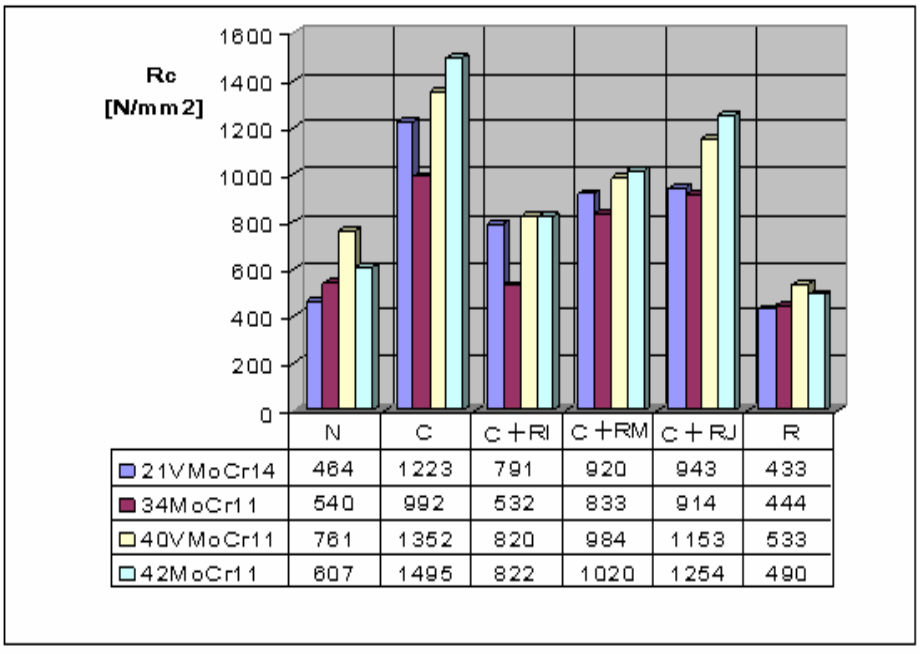

	N	C	C +RI	C +RM	C + RJ	R
21VMoCr14	464	1223	791	920	943	433
34MoCr11	540	992	532	833	914	444
40VMoCr11	761	1352	820	984	1153	533
42MoCr11	607	1495	822	1020	1254	490

Fig. 1. *The variation of the flowing limit depending on the thermal treatment applied for the four steel brands studied*

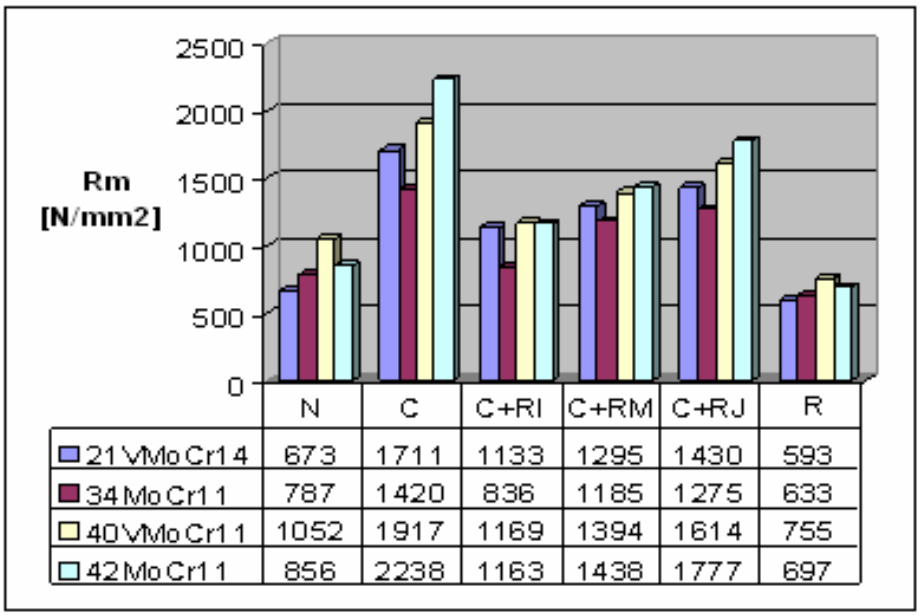

	N	C	C+RI	C+RM	C+RJ	R
21VMoCr14	673	1711	1133	1295	1430	593
34MoCr11	787	1420	836	1185	1275	633
40VMoCr11	1052	1917	1169	1394	1614	755
42MoCr11	856	2238	1163	1438	1777	697

Fig. 2. *The variation of the tensile strength depending on the thermal treatment applied for the four steel brands studied*

In order to establish a metallurgical ongoing state in the comparative analysis, all the samples had initially been put under a **stress-relieving annealing** thermic treatment. This way the internal tensions, remnant to the rolling process of the semi product, had been tampered down and the potential danger of breaking at mechanical strains was eliminated in order not to affect the determination's relevance. The four steel brands studied in this paper have a relatively low mechanical resistance combined with satisfying plasticity and tenacity.

The tendency to reduce the tenacity, induced by the chrome presence, is compensated by reducing the fragility with the influence of molybdenum and vanadium.

One can notice a superior plasticity to carbon content comparable (at the brands with vanadium), which is explained by the role of the chemical element in finishing the grains.

After the ***stress-relieving annealing*** thermal treatment applied to the studied samples, if we take into consideration the average value of the impact strength, we notice that this is with over 50% higher at 40VMoCr11, as compared to 42 MoCr11, an observation valid also for the elongation (A), bottlenecking (Z) and flowing (Rc). This gap is also noticed at the comparison between 21VMoCr14 and 34MoCr11, although the comparison is less relevant due to the carbon content difference.

The flow limit for the four steels studied is comparatively presented in the graph in fig. 1. It can be noticed that the highest values of the flow limit is recorded in the case of ***quenching and quenching followed by low annealing***.

The tensile strength records values significantly higher when quenching, according to the thermal treatment applied to the studied steels for the four types of steel.

Elongation has the highest values at high annealing. All four steels have the best values compared to the other treatments in the case of high annealing. So, high annealing is the most efficient treatment for the studied steels, when it is required as the main property elongation.

The impact strength has significant values when high annealing is applied, the highest value obtained is 82.7 Joule, for the steel 34MoCr11. When quenching we have the lowest impact strength values, for all the types of the studied steels.

Bottlenecking depending on the thermal treatment has the highest values for high annealing for all the steel types in question.

Applying ***the normalization treatment*** had as a notable result an increase of the mechanical resistance (fig. 2) without important changes of the plasticity or tenacity. The brands with a higher content of carbon presented the highest variations of the tensile strength and the flow limit, while the role of the alloying elements had a similar behavior just like the annealing. It is to be noticed the increase of 40% of the mechanical resistance for the brand 40VMoCr11, while keeping an average value of 32 Joule for the breaking energy, value that means it has a satisfying tenacity. It can also be noticed that the influence of the carbon content on the increase of the mechanical resistance is higher for steels with vanadium, where this element acted as a strong agent of forming the carbides.

The quenching thermal treatment applied on the four series of material lead to doubling the mechanical resistance (fig. 2), associated with a drastic diminishing of the plasticity and tenacity, with but one exception (34MoCr11), where it was a diminishing of the elongation of three times and of the bottlenecking of half. (fig. 3, fig. 4, fig. 5).

The average value of the breaking energy dropped under the value of 27 Joule in all cases, a value that is considered as a limit under which the breaking becomes fragile. The hardness value increased with a similar proportion to the mechanical resistance, with a higher effect at the brands with a high content of carbon.

The presence of chrome increased the fragility tendency in all cases, with a higher effect at the brands with a high carbon content.

The double thermal treatment of quenching and annealing made that the mechanical resistances to decrease while the units characterizing plasticity (A, Z) and tenacity (KV) to increase significantly.

These evolutions are the more obvious as the annealing temperature rises. Please notice the highly different proportion where the mechanical resistance changes as compared to the tenacity.

The high annealing at 42MoCr11 lead to the decrease of the mechanical resistance with approximately 50%, while the breaking energy increased ten times. As the studied steels are made for the construction of machine components, this evolution confirms the usage aptitude that requires high mechanical resistance combined with a very good tenacity (durable without affecting the capacity of jolt taking).

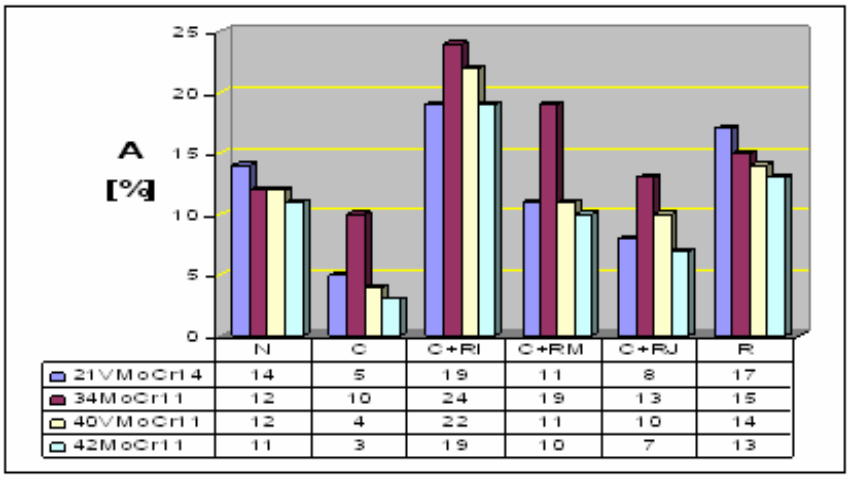

	N	C	C+RI	C+RM	C+RJ	R
21VMoCr14	14	5	19	11	8	17
34MoCr11	12	10	24	19	13	15
40VMoCr11	12	4	22	11	10	14
42MoCr11	11	3	19	10	7	13

Fig. 3. *The elongation variation depending on the thermal treatment applied to the four steel brands studied.*

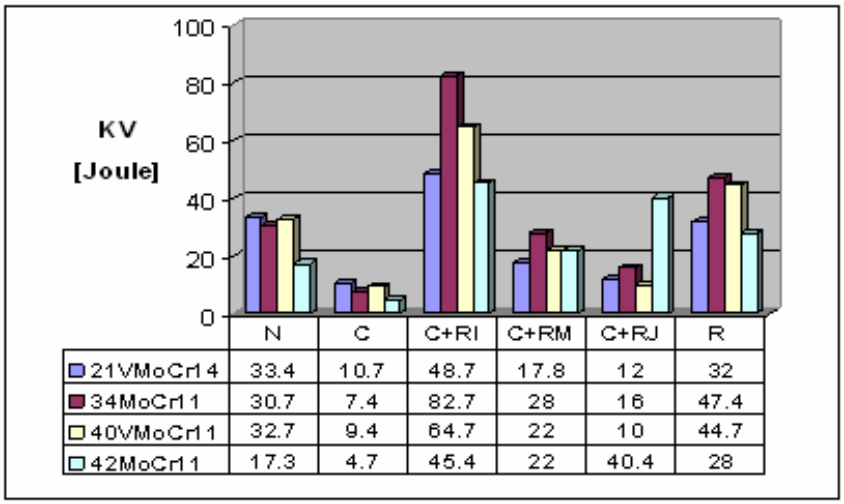

	N	C	C+RI	C+RM	C+RJ	R
21VMoCr14	33.4	10.7	48.7	17.8	12	32
34MoCr11	30.7	7.4	82.7	28	16	47.4
40VMoCr11	32.7	9.4	64.7	22	10	44.7
42MoCr11	17.3	4.7	45.4	22	40.4	28

Fig. 4. *The impact strength variation depending on the thermal treatment applied to the four steel brands studied.*

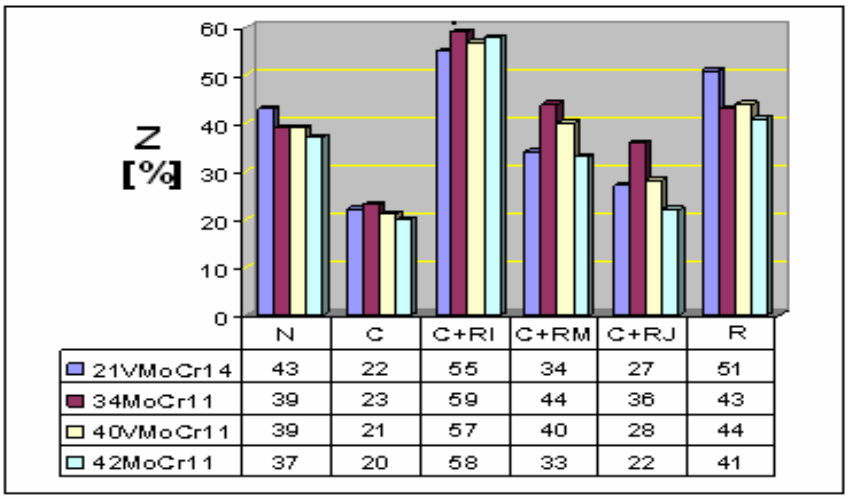

	N	C	C+RI	C+RM	C+RJ	R
21VMoCr14	43	22	55	34	27	51
34MoCr11	39	23	59	44	36	43
40VMoCr11	39	21	57	40	28	44
42MoCr11	37	20	58	33	22	41

Fig. 5. *The bottleneck variation depending on the thermal treatment applied to the four steel brands studied*

Fig. 6. *Microstructure obtained after the normalisation treatment for the steel 40VMoCr11- ferite+fine perlite (x100)*

Fig. 7. *Microstructure obtained after the normalisation treatment for the steel 42MoCr11- ferite+perlite (X100)*

Fig. 8. *Microstructure obtained after the normalisation treatment for the steel 40VMoCr11- ferite+very fine perlite+ troostite (x500)*

Fig. 9. *Microstructure obtained after the normalisation treatment for the steel 42MoCr11 - ferite+perlite (X500)*

The mechanical characteristics are confirmed by the quantity, size, shape of the structural constituents resulted after the phase transformations at thermal processing. The structural morphology depends both on the carbon content as well as the presence of the other elements from the chemical composition of the steel brands analyzed in this paper. In fig. 6…15, there are several examples of microstructures (at

different zooms in order to be more suggestive) that should show the acute change of the structural constituents as well as the size of the crystalline grains. This is a result of the increase of the carbon content or of vanadium alloying.

Fig. 10. *Microstructure obtained after the quenching treatment for the steel 40VMoCr11– martensite +rezidual austenite +troostite (x100)*

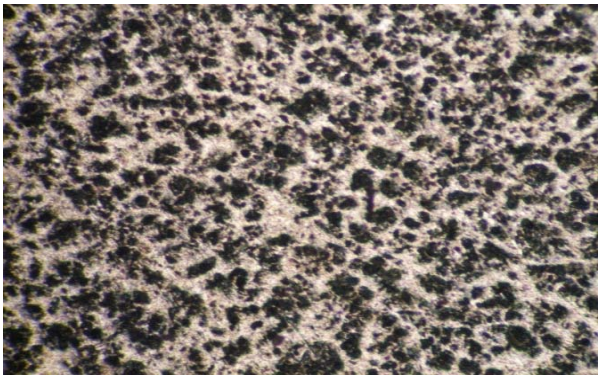

Fig. 11. *Microstructure obtained after the quenching treatment for the steel 42MoCr11- white martensite + rezidual austenite + troostite (X100)*

Fig. 12. *Microstructure obtained after the quenching treatment for the steel 40VMoCr11 – martensite +rezidual austenite +troostite (x500)*

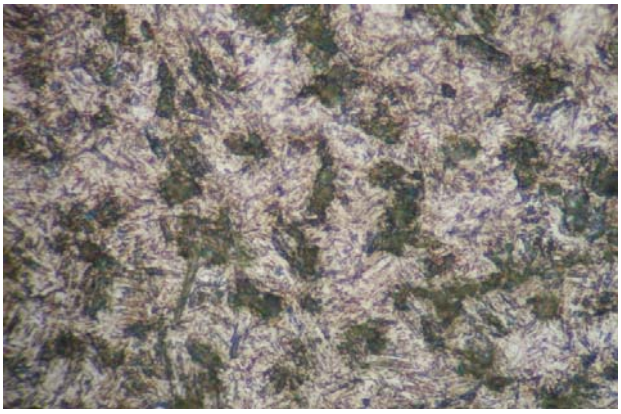

Fig. 13. *Microstructure obtained after the quenching treatment for the steel 42MoCr11- white martensite + rezidual austenite + troostite (X500)*

Fig. 14. *Microstructure obtained after the quenching + high annealing treatment (improvement) for the steel 40VMoCr11- sorbite (X100)*

Fig. 15. *Microstructure obtained after the quenching + high annealing treatment (improvement) for the steel 42MoCr11 - sorbite (X100)*

4. Conclusions

Applying the normalization treatment had as a notable result the increase of the mechanical resistance, without important changes of plasticity and tenacity.

The quenching behaviour of the studied brands can be summarized by doubling the mechanical resistance, associated with a drastic decrease of the plasticity and tenacity, which requires for a second annealing thermal treatment so that it takes the structure to phases closer to equilibrium.

Comparing the values after normalisation, and after annealing, we notice that the high annealing lead in all cases to mechanical properties of resistance, ductility and tenacity superior to those obtained after normalization.

One can also notice the influence of the elements' content of alloying on the mechanical characteristics when we compare the brand 40VMoCr14 to the 42MoCr11.

Under the same treatment (high annealing), the mechanical resistance is superior to 40VMoCr14, with a lower carbon content, the result being obtained without a significant weighing factor of plasticity or tenacity.

As the studied steels are meant for the construction of machine components, this evolution confirms the usage aptitude that requires a high mechanical resistance combined with a very good tenacity (durability, without affecting the capacity of jolt taking).

References

[1]. H.E. Boyer - *Chapter 1, Practical Heat Treating*, 1st ed., American Society for Metals, (1984), p 1–16.
[2]. *** - *Metals & Alloys in the Unified Numbering System*, 10th ed, SAE International and ASTM International, (2004).
[3]. H.N. Oppenheimer - *Heat Treatment of Carbon Steels*, Course 42, Lesson 1, Practical Heat Treating, Materials Engineering Institute, ASM International, 1995
[4]. H.E. Boyer - *Chapter 2, Practical Heat Treating*, 1st ed., American Society for Metals, 1984, p 17–33
[5]. C.R. Brooks - *Principles of the Heat Treatment of Plain Carbon and Low Alloy Steels*, ASM International, (1996).
[6]. *** - A*tlas of Time-Temperature Diagrams for Irons and Steels*, G.F. Vander Voort, Ed., ASM International, (1991).
[7]. G. Krauss - *Steels: Processing, Structure, and Performance,* ASM International, (2005).

THE ANNALS OF "DUNAREA DE JOS" UNIVERSITY OF GALATI.
FASCICLE IX. METALLURGY AND MATERIALS SCIENCE
N^0. 4 – 2012, ISSN 1453 – 083X

SYNTHESIS AND CHARACTERISATION OF Ag/SnO_2/CLAY NANOCOMPOSITES WITH POTENTIAL APPLICATION AS PHOTOCATALYSTS

Claudia-Mihaela HRISTODOR, Diana TANASA, Narcisa VRINCEANU, Violeta-Elena COPCIA, Aurel PUI, Eveline POPOVICI
"Al.I.Cuza" University of Iasi
email: narcisa.vrinceanu@ulbsibiu.ro

ABSTRACT

This work reported a novel synthesis and characterization of Ag/SnO_2/clay nanocomposites. The obtained materials were characterized using techniques such as X-ray diffraction (XRD), Fourier Transform Infrared Spectroscopy, particles size distribution, BET analyses and Scanning Electron Microscopy. The Ag/SnO_2/clay nanocomposites have been used as efficient and environmentally benign photocatalysts. The protocols developed using this kind of material is advantageous in terms of simple experimentation, reusable catalyst, excellent yields of the products, short reaction time and preclusion of toxic solvents. The synthesized nanosized AgSnO_2/clay nanocomposites have been used as photocatalysts for degradation and discoloration of synthetic wastewater containing Eosin Y dye, xanthene fluorescent dye, under solar radiation.

KEYWORDS: clay, nanocomposite, dye, wastewater

1. Introduction

A great variety of methods have been used in recent years to synthesize nano powders of oxide materials and especially semiconducting powders like TiO2, MgO, Fe_2O_3, SnO_2 and ZnO. Nano-sized tin oxide (SnO_2) is an interesting semiconducting material with a wide band gap (Eg = 3.6 eV, at 25^{o}C) [1]. Nanoparticles of tin oxide have found a wide range of applications in gas sensors, lithium batteries, optoelectronic devices, transparent electrodes and photocatalysts [2-8]. It is generally known that by changing the method of preparation it is possible to change the structural, morphological and textural properties of metal oxide particles.

A very promising candidate for such an application is represented by the system silver tin oxide [9]. The noble metals deposited on the surface of nano oxide powders can improve its photo-catalytic properties.

There has been very limited study in this direction. The researches ont the preparation of silver nanoparticles have been an extraordinarily active area due to its potential applications in nanoelectronics, magnetics, biosensor, data storage, catalysis, surface enhanced Raman scattering and excellent antibacterial activity [10–15]. Most of these applications require nanoparticles with a small particle size and a narrow size distribution [16, 17].

To the best of our knowledge, there has been no publication on the synthesis of the Ag/SnO_2/clay nanocomposites. The present method for silver nanoparticles preparation is not only the formation rate of silver nanoparticles much quicker, particle size distribution more uniform, but also offers numerous benefits of eco-friendliness and compatibility for pharmaceutical and biomedical applications due to all the environmentally benign and renewable materials used in the experiments are [18].

Metals or semiconductor nanoparticles synthesized by various techniques have found potential application in many fields such as catalysis, sensors, etc. [19 -22]. In most of the applications, nanoparticles are used as building blocks toward functional nanostructures. The coinage metal nanoparticles such as silver, gold, and copper are mostly exploited for such purposes as they have surface plasmon resonance absorption in the UV visible region [23]. The surface plasmon band arises from the coherent existence of free electrons in the conduction band due to the small particles size effect, which is dependent on the particle sizes, chemical surrounding, adsorbed species on the surface, and dielectric constant. [23-26] The unique feature of the

coinage metal nanoparticles is that a change in the absorbance or wavelength provides a measure of the particle size, shape, and interparticle properties. For small particles (2 nm), the surface plasmon band is strongly damped due to low electron density in the conduction band. However, as particle size increases, the intensity of the surface plasmon band increases. It has been suggested that, although both absorbance and scattering contribute to the optical property, the contribution of the latter is relatively insignificant as compared to that of the former for very small nanoparticles (e15 nm). [19-33]

2. Experimental Methods

2.1. The starting material

As raw material, we used clay of montmorillonite bentonite type, provided by firma Riedel-de Haen Chemicals Company. Given the compositional complexity of clay materials, we considered useful to perform an ion exchange process, as a first step, for their cleansing, their transition to sodium cation form, respectively. The clay exchange in Na^+ form has been performed by treating it with a 1M NaCl solution, having a solid/liquid ratio of 1:10 [34, 35].

2.2. Preparation of Ag/SnO_2/clay nanocomposites

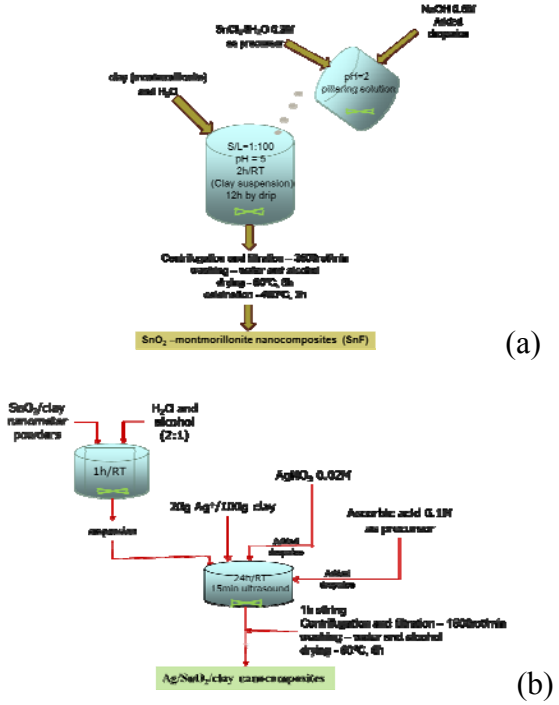

Fig. 1. *Schematic illustration for preparation of nanosized Ag/SnO_2/clay compounds (AgSnF)*

Bentonite montmorillonitic-clay, provided by Riedel-de Haen Chemicals Company, was used as starting material. The nanosized SnO_2 particles were prepared by pillaring method (dispersing the tin oxide particles). Preparation of Ag/SnO_2/clay nanocomposites takes place in two steps preparation of SnO_2/clay nanometer powders (Fig. 1, a) and obtaining of Ag/SnO_2/clay nanocomposites shown in Fig. 1, b.

2.3. Studies of photocatalysis

Investigations of photocatalytic oxidation have been performed, having as objective degradation and discoloration of synthetic solution containing Eosin Y dye, by varying the concentration of catalyst (0,5-2g/l). Photocatalysis occurs in two stages: the first step consists in adsorption in the dark conditions, for 30 minutes and the second step relies on photometric measurement of the dye concentration, by exposure to UV light running at wavelength of 254 nm at equal time intervals based on the calibration curve.

The study was conducted in an initial concentration of pollutant (Eosin Y dye) in water of 20 mg/L, using nanometer SnO_2 as photocatalyst. Other working conditions are as follows: for photocatalysis 1g catalyst/L, 2g catalyst/L respectively, have been used, at an initial pH=5.5±0,2, temperature 25°C±2°C. Photocatalytic test was done using a type of UV lamp UVP, 254 nm surface. Photocatalyst sample was stirred for 30 min to reach equilibrium and then coupled to the UV lamp and the timer was turned on.

2.4. Characterization methods

The structure and properties of the obtained materials were studied by X Ray Diffraction (XRD), FTIR spectroscopy, N_2 adsorption-desorption isotherms and UV–Vis diffuse reflectance spectroscopy. The structures of pure and modified clay were investigated using Shimadzu LabX XRD 6000 diffractometer. The diffraction angle was scanned from 10 to 80 degrees, an usual interval for complex clays and SnO_2. Measurement conditions were: X-ray tube, Cu target Cu, voltage = 40.0 (kV), current 30.0 (mA) and scanning: scan mode-Continuous Scan, scan speed 2.0000 (deg/min). FTIR spectra were recorded on a FTIR JASCO 660+ spectrometer. UV–vis diffuse reflectance spectra recording was performed by a Shimadzu UV-2401 PC Recording Spectrophotometer ranging between 200–600 nm. The adsorption isotherms of N_2 , specific surface areas and porosities were determined with a Nova 2200e (Quantachrome Instruments) automated sorptometer at 77 K. Particles size distribution and mean particle size diameter (D_p, nm) measurements were recorded using an optic

measurement device SALD-7001 type Laser Diffraction Particle Size Analyzer (Shimadzu, Japan).

3. Results and Discussion

Changes occurring in the structure of lamellar supports can be monitored on the basis of Bragg reflections determined from the X-ray diffractograms of the Ag/SnO_2/layer silicate samples.

Identification of peaks was performed using the diffractometer software. The pure clay presents all specific peaks for complex clays: quartz, bentonite, feldspar, aluminum silicate and mica. Reference diffractogram for thin oxide shows a nanocrystalline powder with tetragonal structure of elementary cell. These elementary cell dimensions are well fitted in SiO_2 sites of clay, as identification image shows. Thus, the stable monodisperse, uniform particle size distribution of silver nanoparticles ise formed.

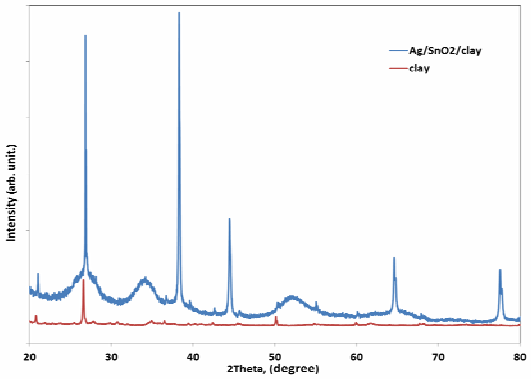

Fig. 2. *X-ray diffraction (XRD) patterns of the studied samples*

X-ray diffraction patterns of clay and Ag/SnO_2/clay nanocomposites have been given in Fig. 2. The crystallite sizes of these samples were obtained by using Scherrer's equation. D = kk/bcosh where D is the crystallite size, k is the radiation wavelength (1.5406 Å), b is the peak full width at half maximum (FWHM), h is the diffracting angle and k = 0.94 for spherical shape particle. The average crystallite size was found to be 18.17Å and 11.75Å (±1) nm, respectively for clay and Ag/SnO_2/clay nanocomposites mode powder. As shown in Fig. 2 the original d-spacing of clay, 3.32Å and 2.34Å of Ag/SnO_2/clay nanocomposites 2θ angles (2θ = 26.82° and 38.29Å respectivelly).

This value is a direct proof of the fact that, in the path of Ag^+ ions are bound not only on the external surfaces and edges of MMT but also in the interlamellar space. Since the ionic radius of Ag^+, is 1.22 Å it is expected that silver occupies interstitial position which in turn can lead to expansion of lattice parameters. We presume that some of the Ag^+ rests go to the surface of the clay.

The IR spectra of the clay and Ag/SnO_2/clay nanocomposites are shown in Figure 3. The band situated at 3614 cm^{-1} is specific to montmorrilonite by its elongation vibrations belonging to OH groups from octahedral layer coordinated, the 1014 cm^{-1} and 1025 cm^{-1} wavelength specific to Si-OH sylanolic groups from the material surface and the 784 cm^{-1} wavelength specific to the deformation vibration of O-H group, bound by an Al-Al-OH cation.

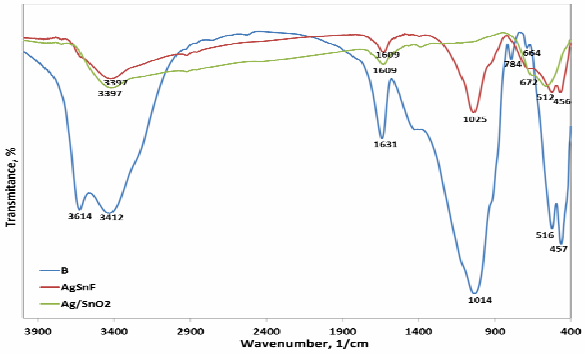

Fig. 3. *FTIR Spectra: B – clay; AgSnF – Ag/SnO_2/clay nanocomposites; Ag/SnO_2 – Ag/SnO_2 nanoparticles*

At the O–H stretching frequency region, all the impregnation and pillared clay materials show two intense IR 3412 cm^{-1} (Fig. 3). These two bands have been assigned to the stretching vibration of the structural OH groups in the clay sheet and to the water molecules present in the interlayer, respectively [36, 37]. If one compares the intensity of these bands for the clay samples, note that the pillaring has a positive impact on the water retention capacity of the clay minerals and the intensity of the band descreases with the process of pillaring. [38]

The IR band observed at 1631 cm^{-1} is due to the bending vibration mode of OH groups. Montmorillonite clay is known to contain two types of hydroxyl groups. One of them is more labile, with an IR absorption pattern similar to that of liquid water and has been ascribed to the water molecules present in the outer coordination spheres of the interlayer cations. The other type is more firmly held and is associated with the water molecules directly coordinated to the exchangeable cations. The latter directly coordinated to the exchangeable cations. The latter is type also contributes significantly to this absorption band [36]. The hydrated aluminum species present in the clay interlayer contain significantly larger amounts of water molecules in the first coordination sphere. The intense band observed for the impregnation and pillared clay suggests the possibility of increasing the acidity due to pillaring since the water molecules in the first coordination sphere dissociate in the clay interlayer, producing

protons. The structural OH-bending mode in montmorillonite shows a series of discrete IR absorption bands between 784 cm^{-1} depending upon the cation composition in the octahedral sheet [39]. Fig. 4 shows bands around 3397 cm^{-1} and 1609 cm^{-1} for Ag/SnO_2 nanoparticles and Ag/SnO_2/clay nanocomposites.

Micromorphology and textural characteristics of clay and Ag/SnO_2/clay nanocomposites are described by the results of nitrogen adsorption/desorption isotherms. The specific surface area has been calculated using BET method at a relative pressure ranging between 0.05-0. The pore volume has been calculated at a relative pressure of 0.95. The distribution of pore size has been determined from the nitrogen adsorption isotherm using Barett-Joyner-Halenda model (BJH model). Subsequenly, isotherms and distributions corresponding to the pore sizes have been performed (Fig. 4).

The general aspect of the samples isotherm reveals an IUPAC IV type isotherm, characteristic to the porous absorbers, presenting the so-called capilar condensation phenomenon. The results of pore distribution calculus (Fig. 4) indicate the occurrence of some mesoporous with 4.18 nm and 3.73 nm radius, respectively.

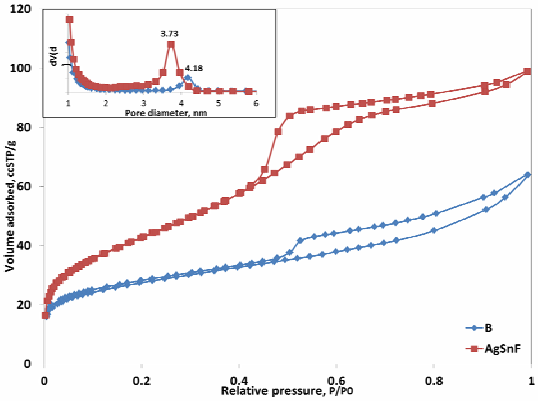

Fig. 4. *The N_2 adsorption/desorption isotherms of the clay (B) and Ag/SnO_2/clay nanocomposites (AgSnF)*

In the domain of partial pressures values higher than p/p_0>0,5 the isotherm unveils the appereance of an H3 type hysteresis, indicating the existence of pores with a relatively even distribution [40]. The amounts of adsorbed nitrogen measured at identical relative pressures are considerably higher in Ag/SnO_2/clay nanocomposites than in the bare clay support. In the Ag/SnO_2/clay nanocomposites samples, N_2 molecules have access to a much larger surface (the nanoparticles own surface also contributes to the overall increase in surface area) than it is the case in the unmodified support. [41]

Table 1. *Textural properties of the materials*

Sample	Surface area, a_{BET}^{s}	Pore volume	Pore diameter
	[m^2/g]	[cc/g]	[nm]
B	97.206	0.127	4.18
AgSnF	153.471	0.267	3.73

From data in Table 1 data, it is noteworthy that after the intercalation of silver/tin oxide between the clay's interlayers the BET specific surface area, pore size and total volume increase, which confirm the fact that silver/tin oxide has been intercalated between the clay's interlayers.

The particle size distribution for clay and Ag/SnO_2/clay nanocomposites is shown in Fig. 5 and Fig. 6. For a sample two consecutive measurements were made. The particle size distribution of clay appeared to be bimodal, with particles averaging about 0.1 μm.

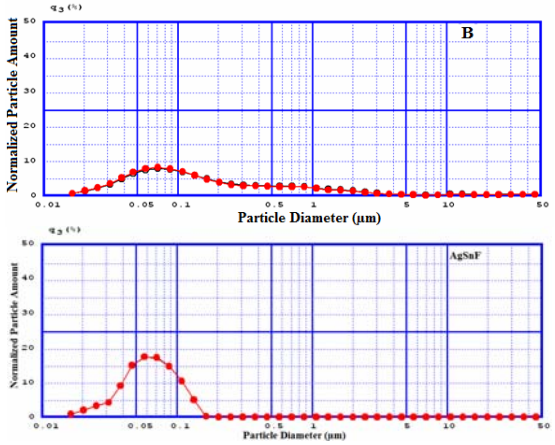

Fig. 5. *Volume histogram of the particle size distribution in clay (B) and Ag/SnO_2/clay nanocomposites (AgSnF)*

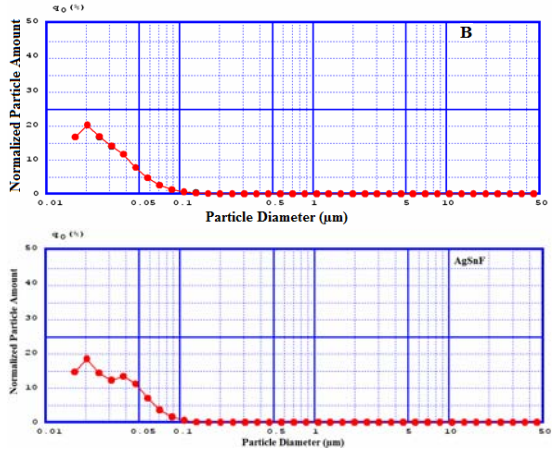

Fig. 6. *Numerical histogram of the particle size distribution in clay (B) and Ag/SnO_2/clay nanocomposites (AgSnF)*

Representing the numerical histogram we could say that the particle size distribution is unimodal with the particle diameter of 0.06 μm.

We firstly checked the photocatalytic performance of the Ag/SnO_2/clay nanocomposites for degradation of Eosin Y dye. The results are shown in Fig. 7. Samples investigations of photocatalytic oxidation had as objective the degradation and discoloration of synthetic solution containing Eosin Y dye, by varying the concentration of catalyst: 1g/L and 2g/L respectively. Some blank experiments (without UV irradiation or catalysts) were carried out in order to check if the Eosin Y dye removal is really due to a photocatalytic process. The experiments conducted in the absence of photocatalyst but with the assistance of UV irradiation showed the fact that the Eosin Y cannot be degraded. The absorption spectra of the obtained Ag/SnO_2/clay nanocomposites are shown in Fig. 7. Eosin Y shows a mean absorption peak in visible region at 516 nm and the rate of decolorization was recorded with respect to the change in intensity of this absorption peak. The main absorption peak has diminished and finally disappeared during photoirradiation process, which indicated that the Eosin Y had been degraded.

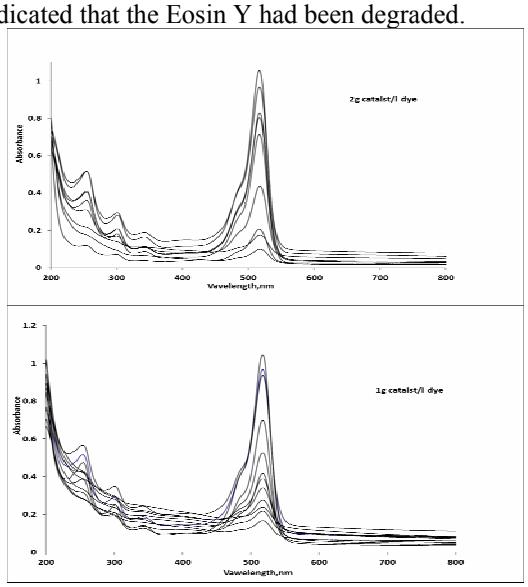

Fig. 7. *UV-vis spectra of the studied samples: 1-2g Ag/SnO_2/clay nanocomposites/L Eosin Y dye*

It is known that the photocatalysed decolourization of a dye in solution is initiated by the photoexcitation of the SnO_2, followed by the formation of electron–hole pair on the surface of catalyst. The high oxidative potential of the hole in the catalyst permits the direct oxidation of the dye to reactive intermediates.

Another reactive intermediate which is responsible for the degradation is hydroxyl radical (OH•). It is either formed by the decomposition of water or by reaction of the hole with OH^-. The hydroxyl radical is an extremely strong, non-selective oxidant (E_0 = +3.06V) which leads to the partial or complete mineralization of several organic chemicals [42, 43]. It can be seen that the loading of silver can significantly enhance the photocatalytic efficiency of SnO_2 in degradation of Eosin Y. The positive effect of noble metal deposits is commonly due to the fact that Ag nanoparticles on the semiconductor surface behave like electron sinks, which provides sites for accumulation of the photogenerated electrons, and then improves the separation of electrons and holes. This can be understood based on the proposed charge separation of Ag/ SnO_2under UV illumination. [44, 45]

An efficient photocatalytic process needs very crystalline semiconductors, in order to reduce the recombination electrons/positive holes pairs. Thus, for an increasing of catalyst quantity up to an optimal dose, a higher quantity leads to an augmentation of the efficiency of Eosin Y removal, due to the generation of a higher number of active species. The bigger the quantity of catalyst, the more HO• radicals. The last one will be considered as main oxidant species responsible for the photocatalytic process [46].

An increasing of photocatalyst quantity over the optimal limit leads to an augmentation of suspension turbidity, thus decreasing the intensity of UV radiation at its passing by the specimen, consequently resulting a decreasing of HO• radicals number generation.

The efficiency of Eosin Y discoloring increase with the increase in the concentration of photocatalysts (Fig. 8).

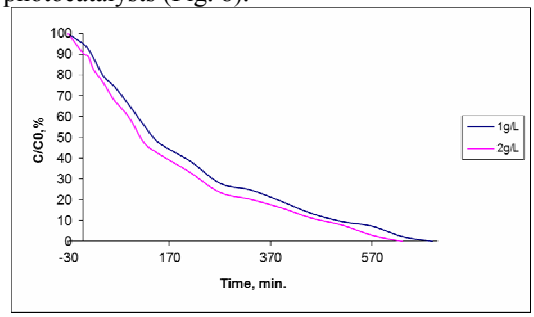

Fig. 8. *Efficiency of photocatalytic degradation of Eosin Y dye in the presence of Ag/SnO_2/clay nanocomposites catalysts samples*

4. Conclusions

We reported the synthesis and characterization of some new Ag/SnO_2/clay nanocomposites. Intercalation of argint/tin dioxide nanoparticles into clay was unambiguously proven by X-ray diffraction. The presence of nanoparticles in the samples was

verified by monitoring the specific surface area of the samples and the particle size distribution. It was established that this parameter increases because the crystallinity of nanocomposites increases. The ability of the nanocomposites to degrade Eosin Y dye under UV light was studied. It is observed that nanosized Ag/SnO_2/clay photocatalysts are an efficient photocatalyst, both in respect of decolorization as well as mineralization of Eosin Y. The synthesized Ag/SnO_2/clay nanocomposites are potential photocatalysts for treatment of organic wastewaters by converting the residual dyes to harmless compounds.

Acknowledgments

The financial support provided by the Research Contract within POSDRU No. /89/1.5/S/49944 Project, belonging to "Al.I.Cuza" University of Iasi.

References

[1]. Sikhwivhilu L.M., Pillai S.K., Hillie T.K. - *Influence of Citric Acid on SnO2 Nanoparticles Synthesized by Wet Chemical Processes*, Submitted to Journal of Nanoscience and Nanotechnology (Revised version).
[2]. Chappel S., Zaban A. - Sol. Energ. Mat. Sol. Cells. 71:141 (2002).
[3]. Schlamp M.C., Peng X., Alivisatos A.P. - J. Appl. Phys. 82:5837 (1997).
[4]. Cirera A., Vila A., Dieguez A., Cabot A., **Cornet A., Morante J.R.** - Sens. Actuat. B 64:65 (2000).
[5]. Miyauchi M., Nakajima A., Watanable T., Hashimoto K. - Chem. Mater. 14:2812 (2002).
[6]. Morales J., Perez V.C., Santos S., Tirado L.J., J. Electrochem. Soc. 143:284 (1996)
[7]. Aurbach D., Nimberger A., Markovsky B., Levi E., Sominski E., Gedanken A., Chem. Mater. 14:4155 (2002)
[8]. Artemyev M.V., Sperling V., Woggon U. - J. Appl. Phys. 81:6975 (1997)
[9]. Patent no. 2644284, 14/09/90 CLAL, *Nouveaux matériaux à base d'argent et d'oxide d'étain pour la réalisation de contacts électriques*.
[10]. Kameo A., Yoshimura T., Esumi K. - Colloids Surf. A: Physicochem. Eng. Aspects 215 (2003) 181–189.
[11]. Ullah M.H., Kim Il, Ha C.S. - Mater. Lett. 60 (2006) 1496–1501.
[12]. Zou X.Q., Ying E.B., Dong S.J., J. Colloid Interf. Sci. 306 (2007) 307–315.
[13]. Tian X.L., Wang W.H., Cao G.Y. - Mater. Lett. 61 (2007) 130–133.
[14]. Mohan Y.M., Lee K., Premkumar T., Geckeler K.E. - Polymer 48 (2007) 158–164.
[15]. Courrol L.C., Silva F.R., Gomes L. - Colloids Surf. A: Physicochem. Eng. Aspects 305 (2007) 54–57.
[16]. Chen Z.T., Gao L. - Mater. Res. Bull. 42 (2007) 1657–1661.
[17]. Khanna P.K., Singh N., Charan S., Viswanath A.K. - Mater. Chem. Phys. 92 (2005) 214–219.
[18]. Xu Guang-nian, Qiao Xue-liang, Qiu Xiao-lin, Chen Jian-guo - Colloids and Surfaces A: Physicochem. Eng. Aspects 320 (2008) 222–226.
[19]. Templeton A. C., Wuelfing W. P., Murray R. W. - Acc. Chem. Res. 33, 27 (2000).
[20]. Storhoff J. J., Mirkin C. A. - Chem. Re., 100, 409 (2000).
[21]. Shipway A. N., Katz E., Willner I. - Chem.Phys.Chem. (2000) 1, 18.
[22]. Zhong, C. J.; Maye - M. M. Ad . Mater. (2001) 13, 1507.
[23]. Kamat P. V. - Chem. Re. (1993), 93, 267.
[24]. Belloni J. - Radiat. Res. (1998), 150, 39.
[25]. Henglein A., Meisel D. J. - Phys. Chem. B (1998), 102, 8386.
[26]. Dimitrijevic N. M., Bartels D. M., Jonah C. D., Takahashi K., Rajh T. J. - Phys. Chem. B (2001), 105, 954.
[27]. Henglien A. Isr. - J. Chem. (1993), 33, 77.
[28]. Bruchez M., Moronne M., Gin P., Weiss S., Alivisatos, A. P. - Science (1998), 281, 2013.
[29]. Brust M., Bethell D., Keily C. J., Shiffrin D. J., Langmuir - (1998), 14, 5425.
[30]. Geirsig M., Pastoriza-Santos I., Liz-Marzan L. M. - J. Mater. Chem. (2004), 14, 607.
[31]. Link S., El-Sayed M. A. - J. Phys. Chem. B (1999) 103, 8410.
[32]. Musick M. D., Pena D. J., Botsko S. L., McEvoy T. M., Richardson T. N., Natan M. J. - Langmuir (1999), 15, 844.
[33]. Anjana Sarkar, Sudhir Kapoor, Tulsi Mukherjee - J. Phys. Chem. B (2005), 109, 7698 7704.
[34]. Popovici E., Hristodor C.M., Alexandroaei M., Hanu A.M. - Rev. Chem. 57: 8-11(2006).
[35]. Popovici E., Humelnicu D., Hristodor - C.M. Rev. Chem. (2006) 57: 675-678
[36]. Trillo J.M., Alba M.D., Castro M.A., Munoj A., Poyato J., Tobias M. - Clay Miner. 27, 423 (1992).
[37]. Miller S.E., Heath G.R., Gonzalez R.D. (1982) Clays ClayMiner. 30:111
[38]. Sowmiya M., Sharma A., Parsodkar S., Mishra B.G., Dubey A. (2007) Applied Catalysis A: General 333:272–280
[39]. Sposito G., Prost R., Gaultier J.P. - Clays Clay Miner. 31:9 (1983).
[40]. Rouquerol J., Rouquerol F., Sing K. - Adsorption by powders and porous solids, ISBN 10: 0-12-598920-2, Published: OCT-1998
[41]. Németh J., Dékány I., Süvegh K., Marek T., Klencsár Z., Vértes A., Fendler J. H. - Langmuir 19 (9):3762-3769 (2003).
[42]. Daneshvar N., Salari D., Khataee A.R., - J. Photochem. Photobiol. A: Chem. 157:111 (2003).
[43]. Kansal S.K., Singh M., Sud D. - Journal of Hazardous Materials 141:581–590 (2007).
[44]. Linsebigler A. L., Lu G. Q., Yates J. T. - *Photocatalysis on TiOn Surfaces: Principles, Mechanisms, and Selected Results*, Chem. Rev. 95 735–58, (1995).
[45]. Weiwei L., Guosheng L., Shuyan G., Shantao X., Jianji W. - Nanotechnology 19 (2008) 445711.
[46]. Nishio J., Tokumura M., Znad H.T., Kawase Y. - J. Hazard. Mater. B138:106-115 (2006).

THE ANNALS OF "DUNAREA DE JOS" UNIVERSITY OF GALATI.
FASCICLE IX. METALLURGY AND MATERIALS SCIENCE
N^0. 4 – 2012, ISSN 1453 – 083X

AUGMENTED REALITY– APPLIED INFORMATICS TECHNOLOGY TO PRODUCTS MAINTENANCE, REPAIR AND SERVICING

Ana-Maria IONESCU[1], Ionel PETREA[2], Florin Bogdan MARIN[2]
[1]Student 2nd year IPMI of Faculty of Metallurgy and Materials Science
[2]Dr.eng. of Faculty of Metallurgy and Materials Science
University of "Dunărea de Jos" of Galati
email:flmarin@ugal.ro

ABSTRACT

Augmented Reality (AR) enhances a user's perception of the real world by enhancing it with specific objects that are over-imposed to the real objects. The virtual objects display information that the user may use it. The information conveyed by the virtual objects helps a user perform real-world tasks. One augmented reality applications is the assembly, maintenance, and repair of complex machinery or common goods. Instructions might be easier to understand if they were available, not as manuals with text and pictures, but rather as 3-D drawings superimposed upon the actual equipment, showing step-by-step the tasks that need to be done and how to do them. These superimposed 3-D drawings can be animated, making the directions even more explicit. This paper describes a proof-of-concept AR application to be used for office printer service operation.

KEYWORDS: augumented reality, informatics, maintenance, repair

1. Introduction

Augmented Reality enhances a user's perception of the real world by enhancing it with specific objects that are over-imposed to the real objects.

The virtual objects display information that the user may use it. The information conveyed by the virtual objects helps a user perform real-world tasks.

There are several AR applications such as medical visualization, maintenance and repair, annotation, robot path planning, entertainment, and military aircraft navigation and targeting.

The next section describes only little research in the AR field. An AR system is defined as a system which combines real and virtual objects in a real environment and run interactively and in real time.

In the medical field**,** doctors could use Augmented Reality as a training aid for surgery using 3-D datasets of a patient in real time, using non-invasive sensors like Magnetic Resonance Imaging (MRI), Computed Tomography scans (CT), or ultrasound imaging, the AR might be a solution to simulate operation [2] [3] [4].

At the moment many research groups are aiming developing augmented reality algorithms and application [5] [6] [7] [8], but no commercial robust products are available on the market. World known company BMW A.G. is developing in their research labs an augmented reality application to help mechanics as shown in Fig.1. By adding more information to the reality, the mechanic will be assisted to service the car. The mechanic is using special goggles to access a computer by wireless communication and to access exactly information they need in workshop, such as order of assembly, torque, etc.

Another category of Augmented Reality applications is the assembly, maintenance, and repair of complex machinery. Instructions might be easier to understand if they were available, not as manuals with text and pictures, but rather as 3-D drawings superimposed upon the actual equipment, showing step-by-step the tasks that need to be done and how to do them. These superimposed 3-D instructions can be animated, making the directions even more explicit.

Current maintenance systems require even the most experienced user to spent time to search manuals, or search within manuals for specific procedures and component data.

Besides that, the stress induced by search within manuals can affect work for certain maintenance and repair operations.

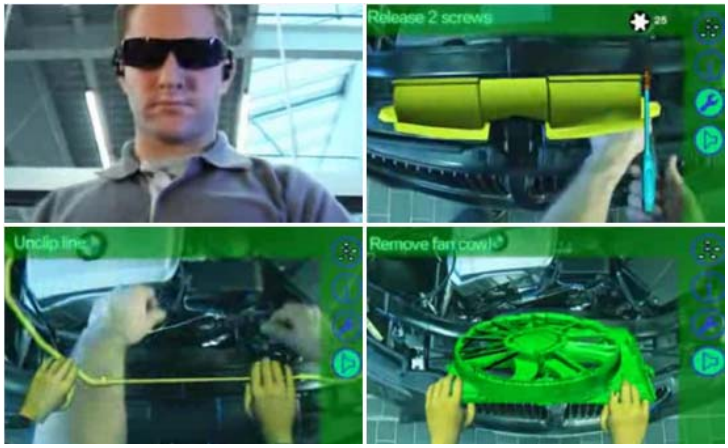

Fig. 1. *AR application developed by BMW for workshop repair*

During the maintaining process, the user must interpret the information in the manual and apply it spatially and conceptually to a particular repair procedure. This means filtering relevant information to matching components in the manual to real world components.

In the early 1990s, Caudell and Mizell invented the term "augmented reality," to define the idea of using an AR system to replace the complex manuals documentation used for airplanes such as the Boeing 747 [11].

Such system in servicing provides several advantages such as to be able to synthesize additional information and complex sequences relatively hard to be explained especially to an inexperienced user (in case of common goods products such as office printers). The information in the manual must synthesise information and is very hard to place and describe a specific context of servicing.

Feiner and colleagues introduced the idea of Knowledge-based Augmented Reality for Maintenance Assistance (KARMA), demonstrating a system to aid a user in servicing an office laser printer [15]. This system interactively generated instructions by tracking user position and orientation and printer position components in order to inform current servicing operation by over-imposing a virtual reality to real one (Fig. 2).

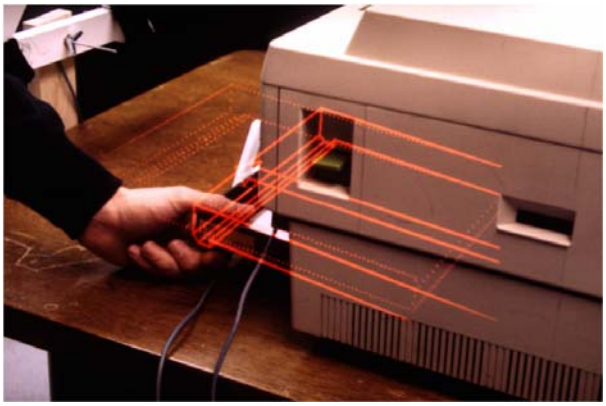

Fig. 2. *Augmented reality for servicing a office printer [9]*

2. Problem formulation

We propose the following problem statement to guide our work:

Provide maintenance and repair assistance to actively assisting in their performance, using augmented reality technology and incorporate instructions and assistance with specific software. We aim to develop an AR application for office printer service.

We found several challenges in order to develop robust augmented reality algorithm:

- Real-time data acquisition and processing. In order to be effective and usable augmented reality algorithm need fast execution and low processing resources.

- Consistent data models. In order to identify parts we need data models. Some components are quite easy to be identified whereas others, with

complex and similar shapes with other are difficult to be identified in 3d space.

3. Problem solution

The hardware used is a Genius Hd Camera and a PC with Pentium D 3 GHz processor processing. The frame's resolution to be processed is 1200X800 pixels. The proposed algorithm is shown in Fig. 3 The object recognition, which is the most challenging part of the algorithm, is represented by SURF (Speeded Up Robust Feature). SURF (Speeded Up Robust Feature) is a robust local feature detector presented by Herbert Bay in 2006, an is based on identifying remarkable features in the image. These features are compared between the model image to the one to be processed and identified.

Using known distance between identified features of the model image, we can approximate position in space relative to the camera of the object.

Once the component is identified the relative positions of features are calculated and the actual position of the component in space is approximated. Using OPenGL library the cartridge model is displayed, taking into account necessary transformation concerning rotation, scale, and point of view. The 3d cartridge model is over-imposed in real image at the correct coordinates.

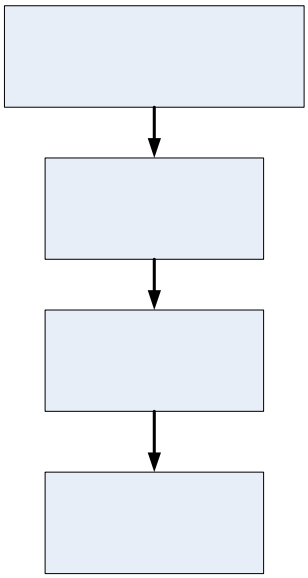

Fig. 3. *The proposed algorithm*

In Fig. 4 Is displayed some of the features detected by SURF algorithm.

The features are previously selected in the model image. In the Fig. 5 Is displayed real image as taken by camera and in Fig. 6 Is shown augmented reality with the 3d model of the cartridge in place and instructions to remove it.

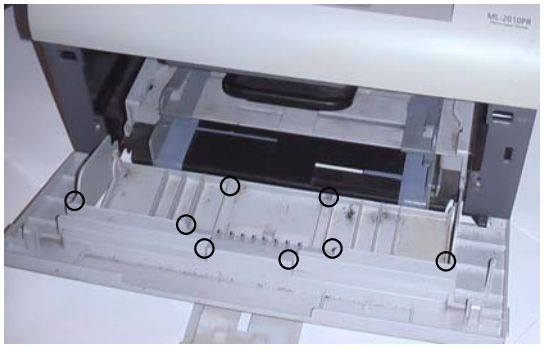

Fig. 4. *Several SURF features identified in the image*

Fig. 5. *Reality as taken by web camera*

Fig. 6. *Augmented reality with instructions for servicing*

We used Visual C 8 IDE environment along with Open CV as computer vision library and OpenGL libraries for 3d graphics display.

The algorithm successfully can be used for those components with enough image variations to be identified as features for SURF algorithm.

However, in case of complex surface with no image variations such as casing of the printer, the algorithm presented fails to identify the surface. Further algorithm and techniques need to be done to solve advanced identification image issues.

4. Conclusion

Augmented Reality is a beyond maturity at the moment.

Today AR systems are primarily found in academic and industrial research laboratories. Several manufacturers are researching currently to release commercial products.

The paper describes a proof-of-concept algorithm. The algorithm successfully can be used for those components with enough image variations to be identified as features for SURF algorithm.

However, in case of complex surface with no image variations such as casing of the printer, the algorithm presented fails to identify the surface.

References

[1]. Andreas Dünser, Hannes Kaufmann, Karin Steinbügl, Judith Glück - *Virtual and Augmented Reality as Spatial Ability Training Tools.*

[2]. R. Beichel. -*Virtual Liver Surgery Planning: Segmentation of CT Data.* PhD thesis, Graz University of Technology, (2005).

[3]. Henry Fuchs, Mark A. Livingston, Ramesh Raskar - D'nardo Colucci, Kurtis Keller, Andrei State, Jessica R. Crawford, Paul Rademacher.

[4]. Samuel H. Drake, **and Anthony A. Meyer** - *Augmented reality visualization for laparoscopic surgery.* In MICCAI '98: Proceedings of the First International Conference on Medical Image Computing and Computer-Assisted.

[5]. Wacker FK, Vogt S, Khamene A, Jesberger JA, Nour SG, Elgort DR, Sauer F, Duerk JL, and Lewin JS. - *An augmented reality system for mr image-guided needle biopsy: initial results in a swine model.* Radiology, 2(238):497–504, February (2006).

[**6]. T. P. Caudell and D. W. Mizell** - *Augmented Reality: An Application of Heads-up Display Technology* to Manual Manufacturing Processes," Proceedings of the Twenty-Fifth International Conference on System Sciences, Hawaii, (1992), pp. 659-669 vol. 2.

[7]. Dangelmaier, W., Franke, W., Mueck, B.; Mahajan, K. - *Augmented Reality Applications in Warehouse Logistics.* In Proceedings of the 7th International Conference on Production Engineering and Logistics, Aim-Shams University, Cairo. Dede, C. (2006): How mediated immersion shapes learning. Online: http://csdl2.computer.org/comp/proceedings/vr/2006/ 0224/00/022xiii.pdf, IEE.

[8]. Doil, F., Schreiber, W., Alt, T., Patron, C. - *Augmented Reality for manufacturing planning.* In Proceedings of the 7th International Immersive Projection Technologies Workshop, ETH Zurich, Zurich (2003).

[9]. Friedrich, W. ARVIKA – *Augmented reality for development, production and service.* Publicis Corporate Publishing, Erlangen (2004).

[10]. S. Feiner, B. Macintyre, and D. Seligmann - *Knowledge-based Augmented Reality,* Communications of the ACM, 36(7), (1993), pp. 53-62.

THE ANNALS OF "DUNAREA DE JOS" UNIVERSITY OF GALATI.
FASCICLE IX. METALLURGY AND MATERIALS SCIENCE
N^0. 4 – 2012, ISSN 1453 – 083X

LOW POTENTIAL HEAT RECOVERY USING HEAT PUMPS

Sorinel TOFAN, Tanase PANAIT
"Dunarea de Jos" University of Galaţi
email: Sorin.Tofan@ugal.ro

ABSTRACT

This paper presents a study on the possibility of recovering low thermal potential heat from the cooling technological water of industrial processes. The analysed solution consists in the use of a heat pump which would send the recovered heat to a hot water flow. We started from a technological water flow which was taken over by a 350 m^3/h cooling tower and we determined the performances of a heat pump when using various refrigeration agents, for a range of values of the temperature of hot water and the temperature of the return of technological water which varies according to the season.

KEYWORDS: heat recovery, technological water**,** heat pump, Carnot efficiency, exergy output

1. Introduction

Many industrial processes require the release of heat flows into the environment, in order to maintain the parameters of those processes within normal operation limits. In the case of high capacity industrial equipment, this heat release is generally performed by means of a flow of cooling water, also called technological water, which takes over the heat from the concerned industrial equipment and, subsequently, releases it into the environment. This release of the heat taken over from the industrial process is generally performed by means of a cooling tower.

Cooling towers, with natural air circulation or with forced air circulation, are based on the operating principle of cooling by evaporation of a certain amount of the technological water. This means that the formed water vapours, which are taken from the air which circulates through the cooling tower, contain the cooling heat of the technological water under the form of latent evaporation heat.

Given the present wishes to increase the use efficiency of energy resources and to decrease fuel consumption, we must analyse all the possibilities of recovering low potential energy resources [1], [2]. We can include here the heat obtained from technological water, released into the atmosphere by means of the cooling towers. Any solution to recover and to use heat from technological water must take into account that, even if heat flows can be very high, the temperature level is, generally, fairly low.

This, if any user of recovered heat requires a certain value of input temperature.

In this paper, we mean to prove the possibility of recovering heat from technological water by means of a heat pump.

This heat pump shall take over the heat from the low temperature technological water and shall send it to a circuit of hot water which can be used by domestic or industrial consumers [3]. Obviously, the concrete application with heat pump sizing must take into account the heat requirement of consumers and the flow of available industrial technological water.

2. Heat recovery by means of the heat pump

For the purposes of this study, we have considered a flow of technological water cooled by means of a 350 m^3/h cooling tower. The operating parameters of the cooling circuit of the technological equipment, as well as its composition, have not been modified, so that the goal of technological process cooling may be achieved when heat recovery does not occur.

Consequently, for the recovery of heat from technological water, a heat pump has been introduced in the cooling circuit (Fig.1) which, by means of the vaporiser, takes heat from the technological water and, by means of the condenser, transfers it to the flow of hot water, which is then sent to consumers [4].

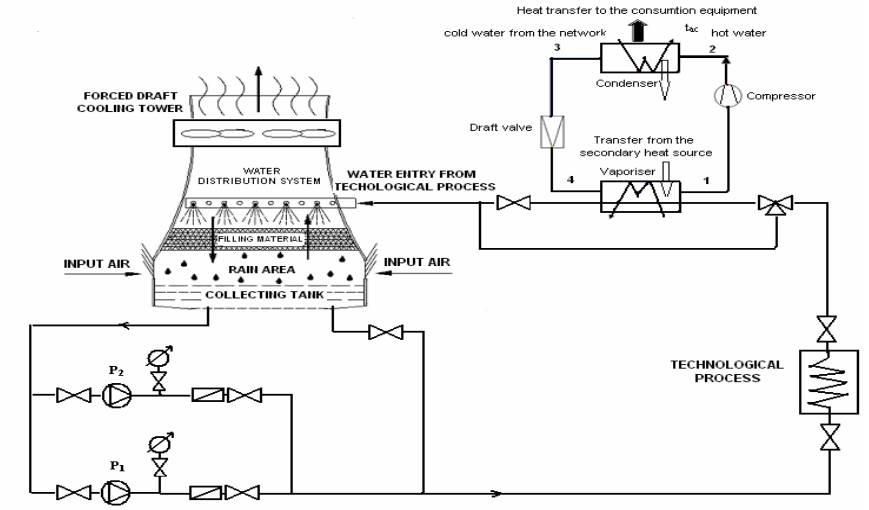

Fig. 1. *Cooling technological equipment with heat recovery*

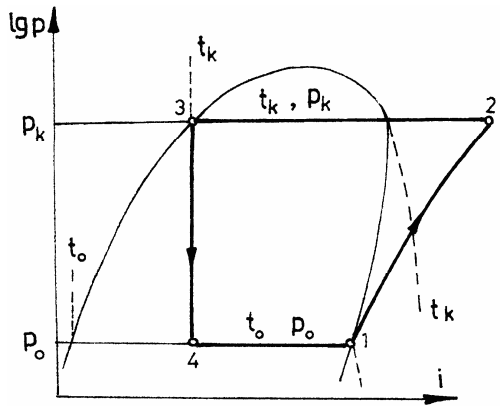

Fig. 2. *Theoretical cycle of the heat pump*

In order to determine the operating parameters of the recovery equipment, we have used the Engineering Equation Solver (EES) programme, able to solve the equations of the mathematical model of processes which take place in heat pumps, consonant with the structure of the equipment and with the type of the working agent which evolves in it. The programme calculates for the heat pump the following performance measures: Carnot efficiency, η_c; exergy output, η_{expc}; coefficient of performance, COP; obtained hot water flow: $\dot{m}_{ac}$ [kg/s].

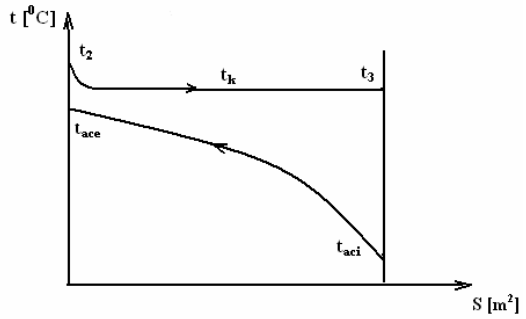

Fig. 3. *Diagram of fluid temperature variation along the heat - condenser transfer area*

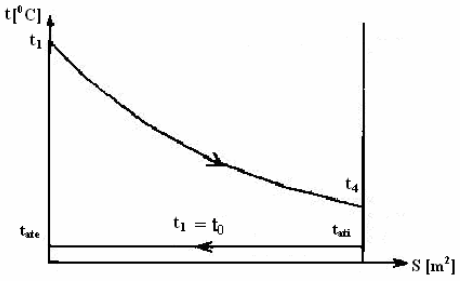

Fig. 4. *Diagram of fluid temperature variation along the heat - vaporiser transfer area*

The hot water flow is calculated on:

$$\dot{m}_{ac} = \frac{\phi_K}{c_a \cdot \Delta t_k} \quad [kg/s] \qquad (1)$$

where: c_a = 4,18 kJ/kg.K - specific water heat; Δt_k = 40 ^{o}C - temperature increase of the obtained hot water; ϕ_K $[kW]$ - heat flow yielded to hot water in the heat pump condenser.

Given the temperature - heat transfer area representations in the heat pump vaporiser (fig. 3), respectively in the condenser (fig. 4), Carnot efficiency, the exergy output of the recovery equipment, as well as the coefficient of performance of the heat pump, are expressed by means of the following relations [5], [6]:

$$\eta_{C1} = 1 - \frac{(t_{mat} + 273,15)}{t_{mac} + 273,15} \qquad (2)$$

$$\eta_{expc} = \frac{\phi_K \cdot \eta_{C1}}{P_{C1}} \cdot 100 \ [\%] \qquad (3)$$

$$COP = \frac{\phi_K}{P_{C1}} \qquad (4)$$

where: $t_{mat} = \frac{t_{ati} + t_{ate}}{2}$ [^{o}C] - average temperature of the technological water which enters the heat pump vaporiser with the temperature t_{ati} and exits it with the temperature t_{ate}; $t_{mac} = \frac{t_{aci} + t_{ace}}{2}$ [^{o}C] - average temperature of the water which enters the heat pump condenser with the temperature t_{aci} and exits it with the temperature t_{ace}; P_{C1} [kW] – power of the heat pump compressor.

We mention that the adoption of the value for the temperature increase of the obtained hot water (Δt_k = 40^{o}C) covers all the possible situations requested by heat consumers. For instance, in the presented application we focused solely on the supply of domestic hot water, which undergoes heating from 25^{o}C to 65^{o}C. However, if the recovered heat flow is used for heating buildings, with the need of increasing hot water temperature to 95^{o}C, then the same temperature increase can be preserved, as a hot water closed circuit is presupposed, with return to 55^{o}C.

By means of the EES programme, we have made a comparative study of the performance of the recovery equipment with heat pump, when using different refrigeration agents. This, given that the thermodynamic properties of the refrigeration agent which evolves in a heat pump directly influence the compression, drafting and heat transfer processes. As main thermodynamic conditions of these refrigerating agents, we mention: boiling point under cooling temperature of technological water, vapour pressure as close as possible to atmospheric pressure, condensation pressure as low as possible in order to achieve low energy consumption, latent evaporation heat as high as possible in order to ensure reduced flows and an as small as possible vapour specific volume. The use of certain inappropriate refrigerating agents can lead to a decrease in the efficiency of the recovery equipment or to the oversize of the heat pump components, these leading to an increase of the recovery costs. Consequently, the following refrigerating agents have been selected, R152a, R500, R600, R114, R717.

3. Results and conclusions

For the analysis of the performances of the equipment for heat recovery from technological water, we considered the following variable measures: t_{ati} - the temperature of technological water on entering the heat pump vaporiser; t_{ace} - the temperature of hot water on exiting the heat pump condenser; $\dot{m}_{at}$ - flow water of the technological process. Given the conditons above, we present below the graphical representation of the results.

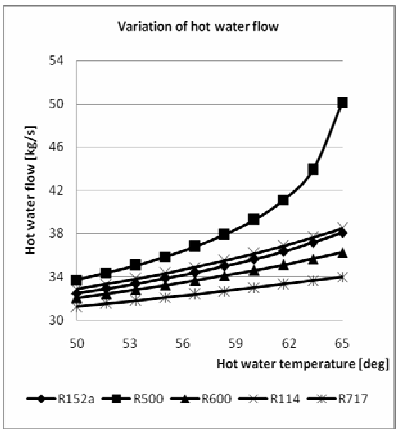

Fig. 5. *Variation of hot water flow*

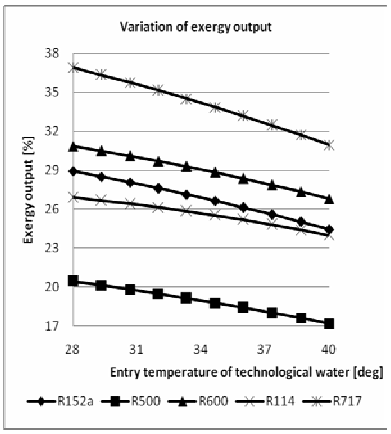

Fig. 6. *Variation of exergy output f(t_{ati})*

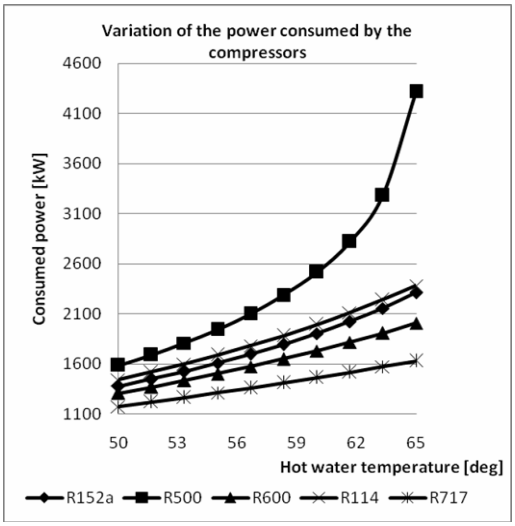

Fig. 7. *Variation of the power consumed by the compressor*

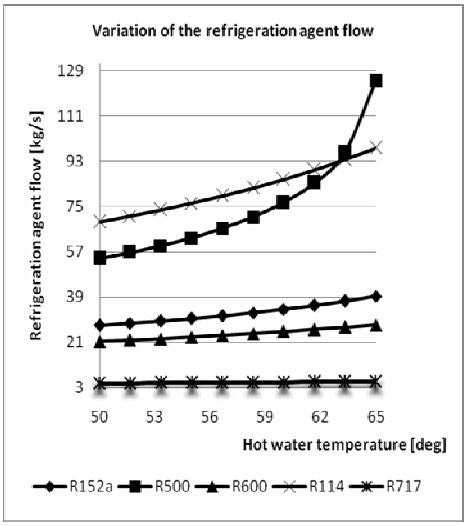

Fig. 8. *Variation of the refrigeration agent flow*

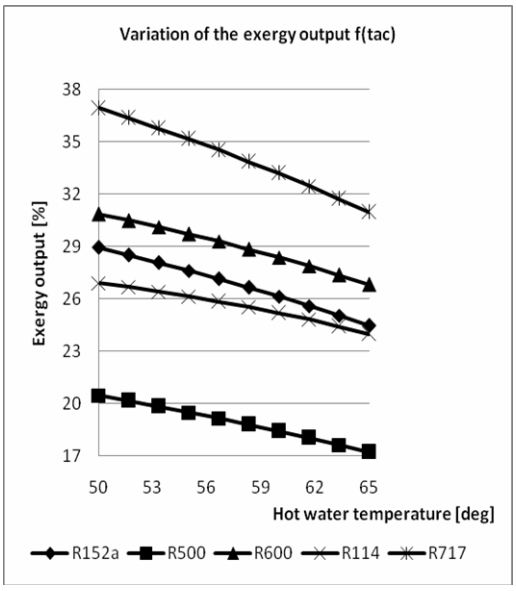

Fig. 10. *Variation of the exergy output f(t_{ac})*

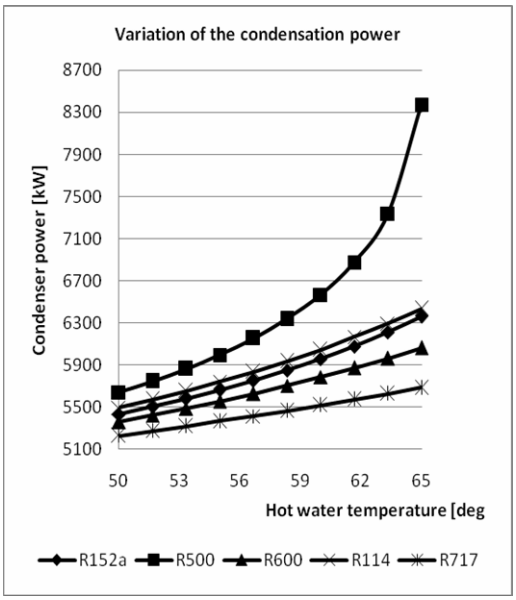

Fig. 9. *Variation of the condensation power*

The values obtained and graphically presented prove the possibility of the proper operation of a heat pump which would ensure the recovery of heat from the cooling water of technological processes. Thus, we can discuss two important aspects:

1. The temperature of hot water on exiting the heat pump condenser directly influences the performances of the recovery equipment. This happens because, for the increase of hot water temperature, condensation temperature must go up, involving the increase of compression pressure with the increase of the power consumed by the compressor (fig. 7). In this case, the increase of the flow of obtained hot water (fig. 5) is explained by the fact that it will increase condenser power (fig. 9), on the basis of the increase of compressor consumption, not due to the increase of the flow of recovered heat.

Still in the conditions of the increase of hot water on exiting the heat pump condenser, one can notice an increase of the refrigeration agent flow (fig. 8). This is explained by maintaining the same minimum temperature differences in the condenser, between the condensation temperature and the exit temperature of hot water, if the flow sent into the condenser increases.

2. The exergy output, considered main coefficient of performance of the heat recovery equipment, is influenced both by the temperature of hot water on exiting the heat pump condenser and by the temperature of technological water on entering the vaporiser. Thus, in the first case, exergy output decreases (fig. 10) because by the increase of the temperature of hot water on exiting the heat pump condenser and the increase of the power consumed by the compressor, the coefficient of performance of the heat pump (COP) shall decrease. In the second case, the decrease of the exergy output, with the increase of the temperature of technological water on entering the vaporiser is due to the increase of the average temperature in the cold source.

The two aspects are specific to any heat recovery equipment which uses heat pumps, irrespectively of the type of refrigeration agent it operates on. We find, however, that there are fairly significant differences in the values of performances according to the type of refrigeration agent, which allows the selection of the most adequate agent. Based on this simulation, it clearly results that for the recovery of heat from technological water by means of heat pumps the most appropriate working agents are R600 and R717, obtaining the best values for exergy output and the lowest compression consumptions.

References

[1]. Athanasovici V., Badea V. - *Valorificarea resurselor energetice*, Editura Tehnică, Bucureşti, (1985).
[2]. Daniel Munteanu - *Posibilităţi de valorificare a resurselor secundare*, Universitatea Transilvania din Braşov, (2004).
[3]. Radcenco V., Florescu Al., Duicu T., Burchiu N. Dimitriu S. ş.a. - *Instalaţii de pompe de căldură,* Editura Tehnică Bucureşti (1985).
[4]. Ming Gao, Feng - Zhong Sun, Kai Wang, Yue - Tao Shi, Yuan - Bin Zhao - *"Experimental research of heat transfer performance on natural draft counter flow wet cooling tower under cross-wind conditions"* – International Journal of Thermal Sciences - 23 July 2007.
[5]. Sava Porneală, Cristian Porneală - *Procese în instalaţii frigorifice şi pompe de căldură*, Editura Fundaţiei Universitare Dunărea de Jos - Galaţi, (2004).
[6]. Constantin Iosifescu, Cristian Iosifescu - *Calculul şi construcţia instalaţiilor frigorifice,* Editura Bren, Bucureşti, (2003).

THE ANNALS OF "DUNAREA DE JOS" UNIVERSITY OF GALATI.
FASCICLE IX. METALLURGY AND MATERIALS SCIENCE
N^0. 4 – 2012, ISSN 1453 – 083X

MATHEMATICAL MODELING OF THE HEAT TREATMENT PROCESS APPLIED ALLOY Al-Zn-Mg-Cu-4.5% Zn WHEREAS, USED IN AERONAUTICS

Marian NEACSU, Doru HANGANU
Universitatea Dunărea de Jos Galaţi
e-mail: uscaeni@yahoo.com

ABSTRACT

In this paper presents mathematical modeling regression analysis method by active experiment a thermal treatment process applied to an Al-Zn alloy system, which finds application in aeronautics.

Using the mathematical model, determined on a statistical basis, the prediction is achieved mechanical properties studied by simulating the heat treatment process, namely the heat treatment simulation parameter values within the experimental values.

Mathematical model equations obtained in this paper can be used to achieve optimal technological parameters of treatment to achieve a set of desired properties with a minimum of expense.

KEYWORDS: mathematical modeling, aluminum alloy, heat treatment

1. Introduction

Mathematical modeling is a form mathematized implementation of a real physical process. As mathematical modeling process can be done in two stages: the first stage is the stage in which the expression of specific mathematical model, and in the second stage specifies how the mathematical model is used to obtain a series of predictions both input quantities, the heat treatment process parameters in this case, and the output quantities, values of mechanical properties studied. All the equations can be obtained mathematical model and optimize the heat treatment process studied.

In this paper we developed a mathematical model of the heat treatment process applied alloy Al-Zn-Mg-Cu containing 4.5% Zn, regression analysis method by active experiment.

Regression analysis method by active experiment is a method of solving problems that require extreme levels determine independent values for input u1, u2, ... uk, where the objective function: $y = f(u_1, u_2, ..., u_k)$ has extreme values (maximum and minimum) and and calculation of these values. [1]. Input values for the heat treatment process studied are: t-temperature heat treatment ie artificial aging temperature; τ - time of artificial aging.

Based on these input data obtained using a mathematical model to study their influence on the studied mechanical properties, mechanical strength, yield strength, elongation at break, hardness HB that is output sizes.

The starting point is random and coordinated basic levels factorial space, u_{01}, u_{02} for the two input values Were established and ranges of these input quantities, Δu_1, Δu_2.

By adding the variation in the basic education level is attained and is obtained by subtracting the lower level of the factor.

If encoded value is denoted by xi ui factor resulting from the relationship:

$$x_i = \frac{u_i - u_{0i}}{\Delta u_i} \qquad (1)$$

upper level is denoted coded +1, the lower level -1, and basic level 0. [1]

2. Experimental conditions

Aluminum alloy processed as illustrated in Figure 1 has a chemical composition shown in Table 1.

Table 1. *Chemical composition of the alloy heat treated*

Chemical element / Alloy	Zn	Mg	Cu	Si	Fe	Pb	Cr	Mn	Al
$AlZn_4,5Mg_1$	4.5	1.4	0.2	0.35	0.4	-	0.35	0.5	rest

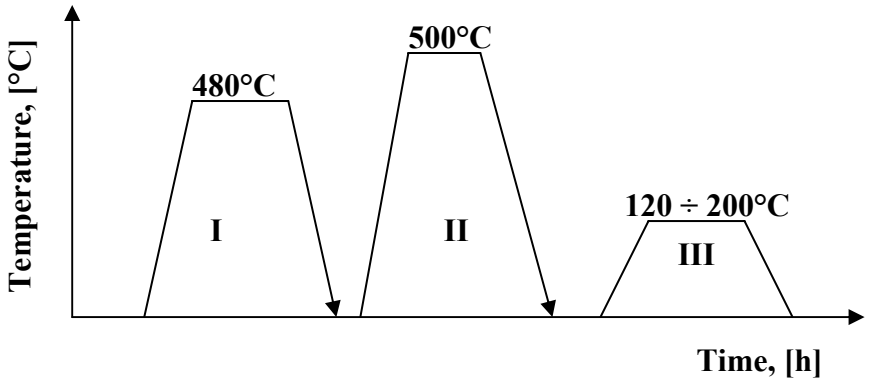

Fig. 1. *Technological scheme for achieving thermal treatment*
I - homogenization, II - implementing solution hardening, III - artificial aging

As illustrated in Figure 1 alloy was processed in a homogenization heat treatment at 480°C, followed by quenching of implementing the solution at 500°C for 2 hours and finally artificial aging at five different temperatures (120, 140, 160, 180, 200°C) with five retention times (4, 8, 12, 16, 20 hours) for each of the five aging temperatures. Thermal processing parameters to achieve mathematical modeling of this process were determined as: 1 - artificial aging temperature - t [°C]; 2 - Time keeping - τ [h];

Table 2 shows the correlation between different levels of factors expressed in natural with those expressed in coded values for the two factors used in the heat treatment.

Table 2. *Correspondence between the factors expressed in natural units and those expressed in encoded units*

Factor	**Process temperature**		**Process duration**	
	Natural units, in °C	**Encoded values**	**Natural units,** in hours	**Encoded values**
Basic level	$u_{01} = 160$	$\frac{160-160}{40} = 0$	$u_{02} = 12$	$\frac{12-12}{4} = 0$
Variation interval	$\Delta u_1 = 40$	0	$\Delta u_2 = 8$	0
Superior level	$u_{1s} = 200$	$\frac{200-160}{40} = +1$	$u_{2s} = 20$	$\frac{20-12}{8} = +1$
Inferior level	$u_{1i} = 120$	$\frac{120-160}{40} = -1$	$u_{2i} = 4$	$\frac{12-20}{8} = -1$

Coded to represent the experiment we used the following notations and symbols:

- x_1 - artificial aging temperature, t, °C;
- x_2 - retention time, τ [h];
- Y_1 - tensile strength, R_m [MPa];
- Y_2 - yield, $Rp_{0.2}$ [MPa];
- Y_3 - hardness, [HB];

Between natural and coded values of the factors are the following relations x_i link:

$$x_1 = \frac{t - t_0}{\Delta t}; \qquad x_2 = \frac{\tau - \tau_0}{\Delta \tau}; \qquad (2)$$

He made a full factorial experiment type 2^2 shown in Table 3.

Table 3. *Determination of 2^2 type factorial experiment matrix*

No. exp.	X_0	X_1	X_2	$X_1 X_2$	Y_1	Y_2	Y_3	Y_4
1	+1	+1	+1	+1	288	248	14.5	71
2	+1	-1	+1	-1	440	385	10.7	127
3	+1	+1	-1	-1	253	221	15.6	62
4	+1	-1	-1	+1	312	269	13.2	91

Considering that the model structure of I, is: [4]

$$Y_i = c_0 + \sum_{i=1}^{2} c_i \cdot x_i + \sum_{\substack{i=1 \\ j=1 \\ i \neq j}}^{2} c_{ij} x_i x_j \qquad (3)$$

Equation (03) is written in matrix form as follows:

$$Y = X \bullet C \qquad (4)$$

where: X is the matrix of experimental conditions

$$X = \begin{Vmatrix} x_{01} & x_{11} & x_{21} & \dots & x_{m1} \\ x_{02} & x_{12} & x_{22} & \dots & x_{m2} \\ x_{03} & x_{13} & x_{23} & \dots & x_{m3} \\ \dots & \dots & \dots & \dots & \dots \\ x_{0n} & x_{1n} & x_{2n} & \dots & x_{mn} \end{Vmatrix} \qquad (5)$$

where: m - number of terms of equation (3);
n - number of experiments considered;
C - column vector of coefficients but
C = [c_0, c_1, ..., c_n] T, where: T is the symbol matrix transposition
Y - Matrix of experimental results

$$Y = [Y_1, Y_2, \dots, Y_n]^T \qquad (6)$$
$$Y = [Y_1, Y_2, Y_3]^T$$

where: Y_1 = [288;440;253;312];
Y_2 = [248;385;221;269];
Y_3 = [14.5;10,7;15.6;13.2]
Y_4 = [71;127;62;91];
For this case, the linear function (3) is a particular form:

$$Y_i = c_0 + c_1 \cdot x_1 + c_2 \cdot x_2 + c_{12} \cdot x_1 \cdot x_2 \qquad (7)$$

For this case, the linear function (3) is a particular form:

$$\mathbf{E} = [\, X^T X \,]^{-1} \times X^T ,$$

follows:

$$\mathbf{C} = [\, X^T \times X]^{-1} [\, X^T \text{ x } Y \,] \qquad (8)$$

expression that represents the relatioship for calculating the coefficients of the regression equation.

Using the values in Table 3, based on the relation (08) to obtain first-order model coefficients, presented in Table 4.

Table 4. *Values of the coefficients of the order I models*

Y_i / c_i	Y_1	Y_2	Y_3	Y_4
c_0	323.25	280.75	13.5	87.75
c_1	-52.75	-46.25	1.55	-21.25
c_2	40.75	35.75	-0.9	11.25
c_{12}	-23.25	-22.25	0.35	-6.75

Therefore mathematical model-order equation (7) for each property separately, is:

$$Y_1 = 323.25 - 52.75 \cdot x_1 + 40.75 \cdot x_2 - 23.25 \cdot x_1 \cdot x_2; \qquad (9)$$
$$Y_2 = 280.75 - 46.25 \cdot x_1 + 35.75 \cdot x_2 - 22.25 \cdot x_1 \cdot x_2; \qquad (10)$$
$$Y_3 = 13.5 + 1.55 \cdot x_1 - 0.9 \cdot x_2 + 0.35 \cdot x_1 \cdot x_2 \qquad (11)$$
$$Y_4 = 87.75 - 21.25 \cdot x_1 + 11.25 \cdot x_2 - 6.75 \cdot x1 \cdot x_2; \qquad (12)$$

By replacing the variables xi relations (2) and these calculations in the above equations we obtain the following equations representing mathematical models of first order expressions for the four properties considered

$$Y_1(t, \tau) = 333.625 - 0.446 \cdot t + 16.718 \cdot \tau - 0.072 \cdot t\, \tau; \qquad (13)$$
$$Y_2(t, \tau) = 278.625 - 0.04 \cdot t + 15.59\, \tau - 0.07 \cdot t\, \tau; \qquad (14)$$
$$Y_3(t, \tau) = 10.75 + 0.025 \cdot t - 0.287\, \tau + 0.001 \cdot t\, \tau \qquad (15)$$
$$Y_4(t, \tau) = 157.975 - 0.544 \cdot t + 1.231\, \tau + 0.001 \cdot t\, \tau; \qquad (16)$$

First-order mathematical models were verified statistically by using Fisher criterion to decide if they can be used to analyze and process study is necessary to determine the higher order models.

After verifying that all models are consistent with experimental data.

Equations (in t and τ) (13), (14), (15), (16) are valid for t = 120 ... 200 ° C and τ = 4 ... 20 hours.

Using these relations, graphs were drawn to each property variation with temperature during treatment:

In Figures 2, 3, 4, 5, are the properties studied variations depending on the heat treatment parameters (temperature and time), both measured and calculated using the mathematical model equations.

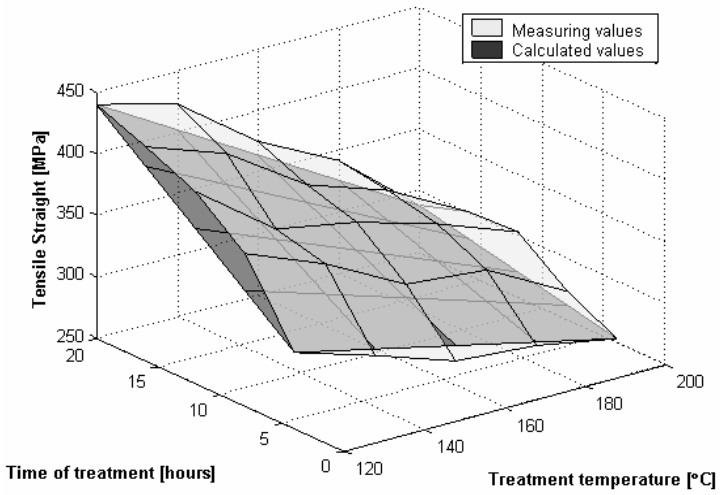

Fig. 2. *Breakthrough variation depending on the time and temperature of artificial aging*

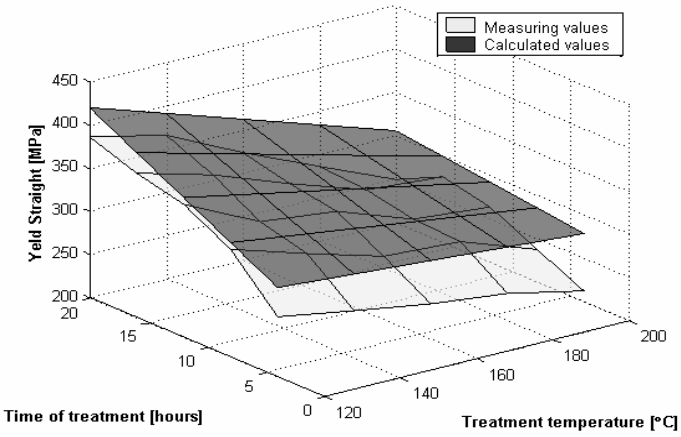

Fig. 3. *Variation of tensile yield stress function of time and artificial ageing temperature*

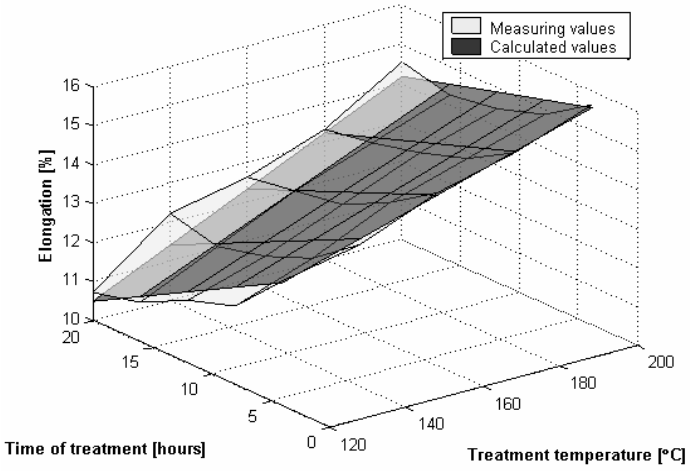

Fig. 4. *Change in elongation at break, depending on the time and temperature of artificial aging*

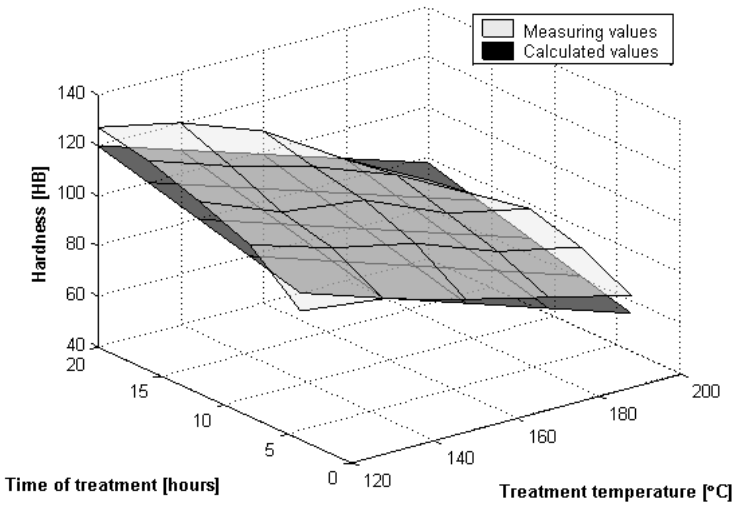

Fig. 5. *Variation of hardness function of time and artificial ageing temperature*

As shown in Figures 2 to 4 mechanical property values determined by calculations using mathematical models are close to the experimentally determined values This is the proof that performed mathematical modeling to simulate the heat treatment process shown in Figure 1.

3. Conclusions

Simulation of heat treatment was based on the mathematical model obtained and presented in equations (13), (14), (15), (16). This simulation is based on technological change parameter values (t, τ) within experimental;

During artificial aging treatment is the factor with the greatest influence on mechanical strength obtained, as shown in the evaluation of equation (13) where τ is a positive parameter coefficient and the highest value;

All of evaluating equation (13) shows that as the artificial aging temperature increases, there is a decrease in strength properties.

Regression equations obtained show that increasing artificial aging temperature in the range considered, above the 180°C leads to a decrease in tensile strength, yield strength and hardness.

The mathematical model presented allows the calculation to optimize process parameters of heat treatment in order to obtain optimal complex properties of resistance, with minimal expenses.

References

[1]. **Taloi D, Florian E, Bratu C**.- *Optimizarea proceselor metalurgice* Editura Didactică si Pedagogică, Bucureşti, (1983).
[2]. **Baron, T. s.a**. - *Statistică teoretică şi economică.* Editura Didactică şi Pedagogică, Bucureşti, (1995).
[3]. Naisnith, S.J. - *Encyclopedie dictionary of mathematics for engineers and applied scientists.* Editura S.J.N, Oxford, (1986).
[4]. Nistor, L. ş. a. - *Modelarea formei secţiunii transversale a laminatului prin optimizarea puterii consumate în procesul de laminare pe principiul metodei de calcul variaţional.* În rev. Metalurgia nr. 5, (1995).
[5]. A. Brăgaru, C. Picoş, N. Ivan – *Optimizarea proceselor şi echipamentelor tehnologice*, Editura didactică şi pedagogică, Bucureşti, (1996).

THE ANNALS OF "DUNAREA DE JOS" UNIVERSITY OF GALATI.
FASCICLE IX. METALLURGY AND MATERIALS SCIENCE
N^0. 4 – 2012, ISSN 1453 – 083X

SOME ASPECTS REGARDING THE INFLUENCE OF THE TRIBOLOGYCAL FACTORS ON THE SUPERFICIAL LAYERS OF TREATED STEELS WITH PLASMA NITRIDING

Carmen Penelopi PAPADATU, Elisabeta VASILESCU
"Dunarea de Jos" University of Galati
email: papadatu.carmen@yahoo.com

ABSTRACT

It were considered some 38MoCrAl09 (SAE 4038) steel grade samples. This material was subjected to the plasma nitriding treatments regimes. The structural and diffractometric aspects of the superficial layers of the steel are studied after the wear tests by friction, using an Amsler type machine, taking two sliding degrees at different contact pressures and testing time. The tests were done to detect the sustainability to the material, the evolution of the superficial layer through different tests and to establish the influence of these tribological factors (operating parameters) on the superficial layers.

Keywords: plasma nitriding process, wear process, tribological parameters

1. Introduction

Nitriding is a heat treating process that diffuses nitrogen into the surface of a steel to create a case hardened surface.

The process are named after the medium used to donate.The three main methods used are: gas nitriding, salt bath nitriding and plasma nitriding.

Plasma nitriding, also known as *ion nitriding*, *plasma ion nitriding* or *glow-discharge nitriding*, is an industrial surface hardening treatment for steels and for other metallic materials such as:
SAE 4100, 4300, 5100, 6100, 8600, 8700, 9300 and 9800 series steel grades, UK aircraft quality steel grades BS 4S 106, BS 3S 132, 905M39 (EN41B), stainless steels, some tool steels (H13 and P20 for example) and certain cast irons. The steels for nitriding should be in the hardened and tempered condition, requiring nitriding take place at a lower temperature than the last tempering temperature. A fine-turned or ground surface finish is best.

Nitriding alloys are alloy steels with nitride-forming elements such as aluminum, chromium, molybdenum and titanium.

In plasma nitriding, the reactivity of the nitriding media is not due to the temperature but to the gas ionized state. In this technique intense electric fields are used to generate ionized molecules of the gas around the surface to be nitrided. The highly active gas with ionized molecules is called plasma, naming the technique.

The gas used for plasma nitriding is usually pure nitrogen, since no spontaneous decomposition is needed (as is the case of gas nitriding with ammonia). There are hot plasmas typified by plasma jets used for metal cutting, welding, cladding or spraying. There are also cold plasmas, usually generated inside vacuum chambers, at low pressure regimes. Plasma nitriding modify the strain limit, and the fatigue strength of the metals being treated. For instance, mechanical properties of austenitic stainless steel like wear can be significantly reduced and the hardness of tool steels can be double on the surface [1,5,7].

Plasma nitriding is often coupled with physical vapor deposition (PVD) process and labeled Duplex Treatment, with enhanced benefits. Many users prefer to have a plasma oxidation step combined at the last phase of processing to produce

a smooth jetblack layer of oxides which is resistant to wear and corrosion.

The superficial layer is defined according to the type of interaction between the external action and materials.

In figure 1 was presented one of the first model of the superficial layer [4,5].

Introducing a surface treatment as nitriding process with plasma (ionic nitriding), increase the wear resistance and the resistance of corrosion increase too [15].

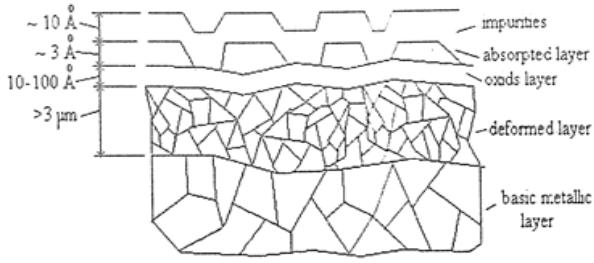

Fig. 1. *One model for the superficial layer*

Diffusion and interaction the nitrogen with the basic material lead to structural constituents whose nature determines a major hardness of the nitrided layer.

The chemical combination area consists of two phases:

- *the* ε *phase* – a solid solution based on the chemical compound of Fe_3N, rich in nitrogen (8.2 to 11.2%N) having a hexagonal compact (HC), crystal lattice, is highly resistant to wear, [1,4,5],and corrosion;

- *the* γ *' phase* – a solid solution based on the Fe_4N compound, presents a centred-face cube (C.F.C.) crystal lattice, has a lower nitrogen solubility (5.7 to 6.1%N), showing very high values of hardnessand tenacity.

The diffusion area is composed of the following elements:

- *the* α *phase (the nitrided ferite)* – a nitrogen connate solid solution in Fe α crystallizing in centre

– volume cube (C.V.C.) lattice, showing a maximum solubility of 0.11% at a temperature of 590° C;

- *the* γ *phase (the nitrided austenite)* – a nitrogen connate solid solution in Fe γ (C.F.C.), having a maximum nitrogen solubility of 2.8% at a temperature of 650° C (see Fig.3) [4,7].

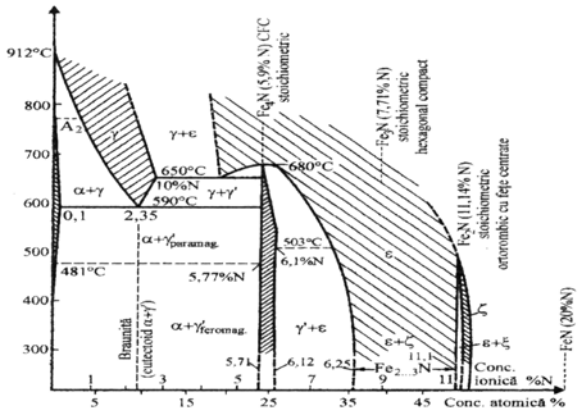

Fig. 2. *Fe-N diagram of equilibrum*

The transformation of $\gamma \rightarrow \alpha$'- martensite with nitrogen (a suprasatured solution of nitrogen in Fe α), showing very high values of hardness, takes place from the nitriding temperature, in case of a rapid cooling of austenite with nitrogen (γ). The hardness and the depth of skin, are determined both by the chemical composition of the chosen material and by the technological parameters of the thermo-chemical treatment [4].

In case of hard worn out parts [4], the skin structure selection has to observe the three – layered rule as it is advised by the tribology studies:

a. – a thin layer of 0.02 to 0.04mm, not so rigid, showing a crystal lattice separate to the basic (hexagonal compact) material, avoiding adhesive wear;

b. – a very tough and flexible layer, not breakable or deformable under very high stresses;

c. – a basic material showing adequate hardness, mechanical strength as well as a suitable tenacity in order to avoid material cracking under stress. Figure 2 depicts the layer hardness in their sequence [5].

The wear behavior of coated surface is controlled by several factors such as the geometry of the contact, the topography of the surface, the material characteristics, mechanical properties of the material, microstructures of the material and the operating parameters (Q, ξ, Δt).

In this paper, are presented a series of researches regarding the structural and the tension state changes that appear and develop in the superficial layer of some materials subjected to damages processes as: running-in, friction, wear or fatigue.

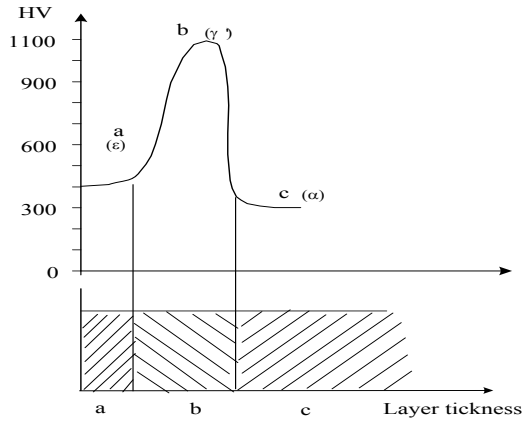

Fig. 3. *The hardness of the superficial layer according with the layer thickness evolution*

For this aim, the tribomodelling operation has been used. The materials tested on tribomodels present some advantages versus in situ ones. Thus, the multifactorial planning of the experiments may be used and the testing optimal conditions, for a given material, can be found.

The friction and wear processes are complex, being of physical, chemical, mechanical or metallurgical nature [2, 3]. These processes appear during dynamic or static contact between surfaces of two solid bodies where may be or not be in a gaseous atmosphere, liquid or solid lubricant. The depth of the superficial layer varies between some atomic layers, in case of wear and chemical processes, and can attain up to 50-100 μm – in case of dry friction.

2. Experimental researches

It were considered some 38MoCrAl09 steel grade samples. This material was subjected to the plasma nitriding treatments regimes.

The structural and diffractometric aspects of the superficial layers of the steel are studied after the wear tests by friction, using an Amsler type machine, taking two sliding degrees at different contact pressures and testing time.

The tests were done to detect the sustainability to the material, the evolution of the superficial layer through different tests and to establish the influence of these tribological factors (operating parameters) on the superficial layers.

To start the researches, it is necessary to present some characteristics about the material. So, in table 1, it was presented the 38MoCrAl09 steel grade composition.

The content of Ni corresponding to 38MoCrAl09 steel is 0.26%. The steel analyzed reach a max score 4.5 from inclusions and a fine grain (score 8-9).

Table 2 presents the mechanical characteristics of the steel SAE 4038 (38MoCrAl09) [2,4,15].

Table 1. *Chemical composition of the materials,* (%)

Steel grade	C	Mn	Si	P	S	Cr	Cu	Mo	Al
38MoCrAl09 (SAE 4038)	0.38	0.50	0.25	0.026	0.020	1.38	0.058	0.17	1.18

Table 2. *Mechanical characteristics of the steel*

Steel grade	$Rp_{0,2}$	R_m	A_5	Z	$KCU_{300/2}$	$KCU_{300/5}$	HB (State of annealing)
	[daN/mm^2]		[%]		[daJ/cm^2]		
38MoCrAl09 AISI (SAE) 4038	85	100	15	50	9	6	229

The steel analyzed in this paper is improved steel grade which should undergo high local variable strains: traction, compression, shearing and therefore certain properties are imperious:

- higher hardness and homogenity of the hardness values;
- elimination, if it is possible, of the residual austenite;
- a good tenacity;
- high elasticity point, so as to keep the plastic deformations within small limits.

The treatment applied was t_1 (classic treatment) followed by nitriding process at 530ºC.

The heat and thermo-chemical treatments applied in nitrided treatment case are:
t1= Martensitic hardening process (at 920°C – for code R) and high recovery (at 620°C – for code R) (classic treatment). T1= t1 + ionic nitriding (plasma nitriding) at 530°C.

The usual methodology for the machine elements studying (roller wheels) used in the metallurgical industry, presents the theoretic contact like a point (point contact) or a line (linear contact).

On Amsler machines [6, 8, 9], was determined the durability of rollers, the surface structure evolution for different parameters of testing regimes. It could not be neglected other factors influencing the wearing process: the contact geometry of the friction couple (roller on roller, roller on ring etc.), the technological parameters (surface quality, heat treatments etc.) and the exploitation conditions (the thermal solicitation, for example).

Wear tests were carried out on an Amsler machine, using several couples of rollers, each couple corresponding to different sliding degrees ξ, defined as:

$$\xi=[(\nu_1-\nu_2) / \nu_1] 100 \ [\%] \quad (1)$$

where v_1 and v_2 are the peripheral velocities of the rollers in contact, each one having their specific peri-pheral velocity due to a particular combination of an-gular speeds (n_1, n_2) and diameter sizes (d_1, d_2). Index 1 or 2 are added for the roller 1 or 2, respectively, both of the same tested friction couple. For instance, *10%*ξ= is obtained for a pair of tested rollers having d_1=40 mm, n_1=180 rpm and d_2=40 mm, n_2=162 rpm; *18%*ξ= is obtained for a pair of tested rollers having d_1=44 mm, n_1=180 rpm and d_2=40 mm, n_2=162 rpm; the level of the stress is corresponding to a specific load of 150 daN (as normal load is Q=1.500 N) and the contact between roller is b=10 mm [2].

3. Experimental results

The phases and their characteristics identifed at diffractometry analysis for 38MoCrAl09 steel grade after Thermal treatment followed by plasma nitriding, are presented in table 3[see 6*,12,13*].

Comparing the results obtained for 122 samples (code R,T1, Q=75 daN, ξ = 10%) and 222 samples (code R, T1, Q = 150 daN, ξ = 10 %), we can see the following aspects:

Table 3.

Code sample	**~ % I_{Fe3N}**	**~ σ_{II} B_{Fe3N}**	**~ % I_{Fe4N}**	**~ σ_{II} B_{Fe4N}**	**~ c/a B_{211}**	**~ σ_I Δθ**	**t** [h]	**Q** [daN]	**ξ** [%]
122	9	3.00	16	3.20	1.31	-0.04	0	-	-
122	22	4.40	17	2.98	1.31	-0.04	1	75	10
122	22	4.88	16	3.20	1.29	-0.05	2	75	10
122	19	4.75	16	3.07	1.29	-0.10	3	75	10
222	10	3.33	12	3.00	-	-	0	-	-
222	5	2.94	6	2.444	2.526	-0.10	3	150	10
422	6	4.00	8	3.2	-	-	0	-	-
422	10	3.33	6	2.4	2.00	-0.15	3	190	20
322	4	4	20	1.81	2.526	-	0	-	-
322	6	4.40	26	2.4	2.526	-	1	150	20
322	4	4	20	1.81	2.26	-	2	150	20
322	20	5	26	3.33	2.260	-0.10	3	150	20

- For 122 sample, after each hour of wear process, we couldn't saw sesizable modification of Phases quantities inside in the superficial layer. But, it was an exception, for Feα quantity, which increase simultanelly with the increase of wear process time.The width of the Fe_4N (40˚ - 42˚) phase increase after three hours of wear process.

- Comparasing 222 sample with 122 sample, at 122 sample -after three hours of wear process, it can be observed that the Fe_3N phase quantity

increased and it was visible the increase of Feα (M) phase quantity too. Results that in the case of classic treatment (T1), when the sliding degrees (ξ) increase (on the increase of the specific load), the quantities of Feα and Fe_3N phases (hard phases) decrease. Finally, we can obtained a decrease of hardness value inside in the superficial layers, after wear process through friction. This variation was correlated and verified with the mass loss evolution during and after wear process. In fig. 4 was presented some diffractometry aspects for 122 samples, after each hour of wear process.

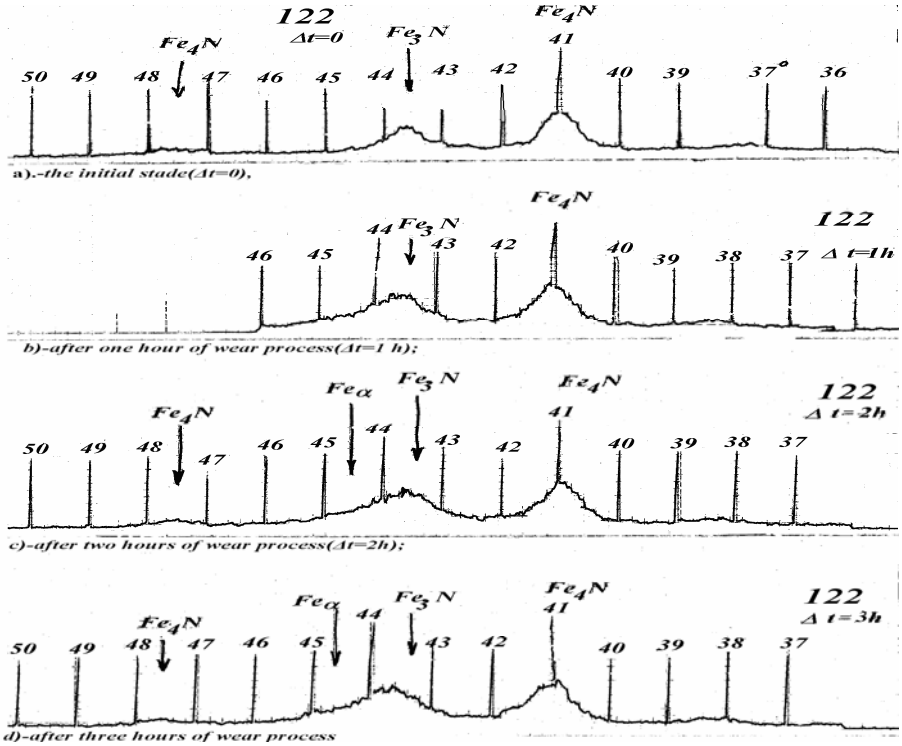

Fig. 4. *Diffractometry aspects for 122 samples (T1,Q=75 daN, ξ=10%) : a).-the initial stade(Δt=0),b)-after one hour of wear process(Δt=1 h);c)-after two hours of wear process(Δt=2h);d)-after three hour of wear process (Δt=3h) , at the same conditions*

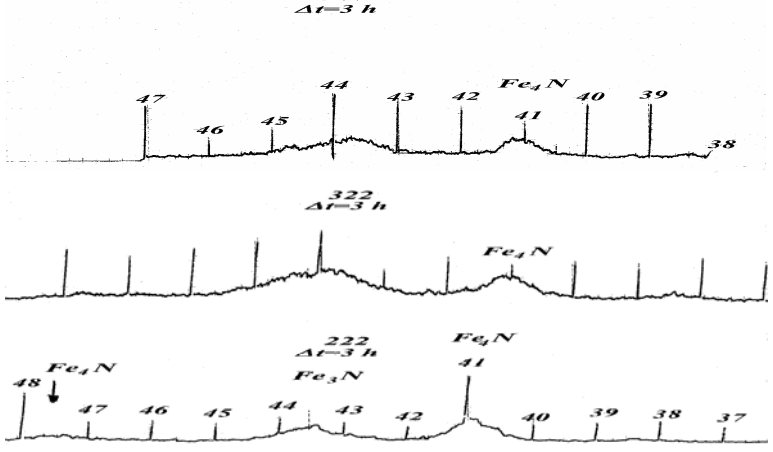

Fig. 5. *Diffractometry aspects for:222 samples (T1,Q=150 daN, ξ=10%), 322 samples (T1,Q=150 daN, ξ=20%), 422 samples(T1,Q=190 daN, ξ=20%)*

In figure 5 are presented some difractometry aspects for 222 samples, 322 samples and 422 samples, after three hours of wear process.

The Fe_4N phase quantity is aproximatelly equal in all the three situations. At 322 sample we can observe the greatest quantity of Martensite. All the samples suffered the same treatment: T1 (Classic treatment), the difference between them is the different value of each sliding degrees (ξ). For example, 322 sample was concerned at three hours with Q=150 daN (as the 222 sample) but the sliding degrees was double then 222 sample case. Between 422 sample and 322 sample, the only difference is the increase of the effort value (Q).

In figures 6 ...11 are presented graphic evolutions for layer characteristics (parameters) during the wear process.

For example, these parameters as: internal tensions of second order vs. test time or, the evolution of the martensite thetragonality grade (c/a) vs. test time, discover the influence of the tribological aspects on the superficial treated layers.

The tests were done to detect the sustainability to the material, the evolution of the superficial layer through different tests and to establish the influence of these tribological factors (operating parameters) on the superficial layers.

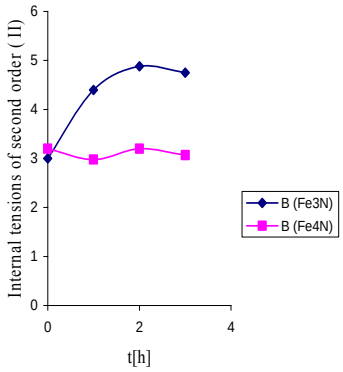

Fig. 6. *The evolution of the internal tensions of second order (B211~σ_{II}) vs.wear test time; (122 sample, Q=75 daN ξ=10%).*

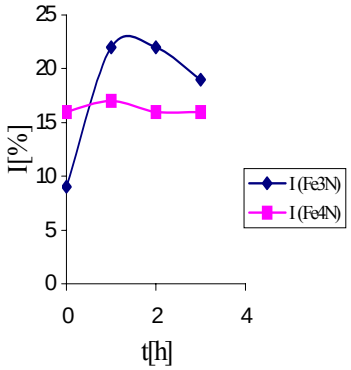

Fig. 7. *Fe_4CN and Fe_3CN phase distribution vs.wear test time (122 sample, Q=75 daN, ξ=10%).*

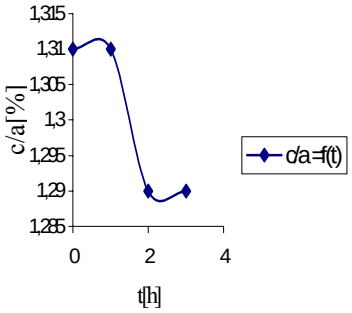

Fig. 8. *The evolution of the martensite thetragonality grade (c/a) vs wear. test time; (122 sample, Q=75 daN, ξ=10%)*

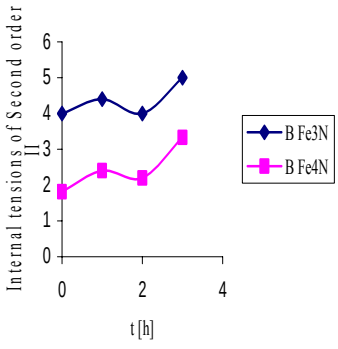

Fig. 9. *The evolution of the internal tensions of second order (B211~σ_{II}) vs.wear test time; (322 sample, Q=150daN ξ=20%).*

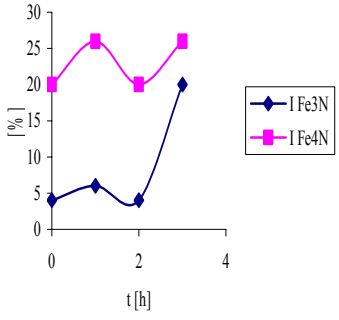

Fig. 10. *Fe_4CN and Fe_3CN phase distribution vs.wear test time (322 sample, Q=150 daN, ξ=20%).*

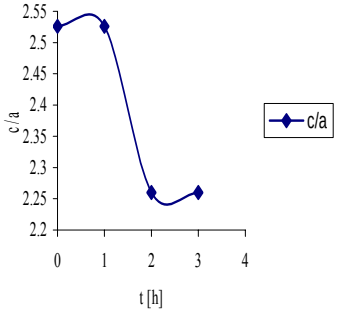

Fig. 11. *The evolution of the martensite thetragonality grade (c/a) vs wear. test time; (322 sample, Q=150 daN, ξ=20%)*

Diffractometric analysis was performed by the help of a Dron 3 system [12,13]. The curves of variation for phases distribution and other characteristics within superficial layers show the evolution of the superficial layer during the wear process.

4. Conclusions

The Diffusion and the interaction of the nitrogen with the basic material lead to structural constituents whose nature determines a major hardness of the nitrided layer.

The friction and wear processes are complex,being of physical, chemical, mechanical or metallurgical nature. These processes appear during dynamic or static contact between surfaces of two solid bodies where may be or not be in a gaseous atmosphere, liquid or solid lubricant. The depth of the superficial layer varies between some of atomic layers, in case of wear or chemical processes, and can attain up to 50-100 μm – in case of dry friction.

In the analyse of the diffractometric aspects presented in fig.4 (a ,b, c, d), it were observed: the evolution of residual Austenite –Arez.- (38º÷ 47º), the evolution of Marthensite -M- (81º ÷ 92º and 44º÷45º), the evolutions of Fe_3N(43º÷44º) and Fe_4N (41º).

In the case of 122 sample, the applied force (strenght) was constant (Q=75 daN) in all three hours with tests of wear and the tribological factor (ξ= sliding degrees = 10%) was constant, too.

It was studied the variation of the phases quantities after each hour of wear process.

In 122 sample case, after each hour of wear process, it couldn't be observed sesizable modifications for the quantities of the phases from superficial layer.

Exists one exception: the quantity of Fe_α(M) which increase simultaneous with the increase of the wear process length. The width of the dimension for the quantity of phase Fe3N increase constantly following three hours of wear process.

In fig. 5, in the case of sample 122 and in the case of sample 322, were applied: the same force (Q=150 daN), the same heat treatment (T_1) but, the tribological factor (ξ) was modified (it is double, through comparing with the fig.4 case).

It was observed that, the increase of the tribological factor (ξ) and the quantity of the phase Fe3N decreases, after three hours of wear process. The quantity of the Fe_4N phase it is aprox. equal, in the presented cases.

Following the evolution of the characteristics from the figures: 6÷8, it was observed that the internal tensions of second order (B211~σ_{II}) increases uniform, until at maximum (corresponding to Δt=2h) and after that, they decrease until Δt=3h.

For the case of B_{Fe4N}, the evolution is cyclic (increase-decrease) for the each 0,5 hour length. This evolution is constant for all the wear process length (Δt =3h).

I_{Fe3N} decrease, although the force applied (Q=150 daN) is constant and the tribological factor (ξ = 20%) is constant, too.

In the case of 322 sample (see figs. 9 ÷ 11), simultaneous with the double values for the applied force (Q= 150 daN) and for triblological factor (ξ = 20%), it was observed a cyclic evolution, constantly, for B_{Fe3N} and I_{Fe3N} , which lead at the material tiredness, inside in the superficial layer.

References

[1]. Gheorghies, C., Papadatu, C.P., Ştefănescu, I. - *Study on the model of behaviour of some non-conventional treated steels, during friction process,* CENTIMFE, Marinha Grande, Portugal, (2004).

[2]. Papadatu, C.P. - *Aspects regarding tribological behaviour of nitrocarburized superficial layer applied after thermo-magnetic treatments, using X-ray diffractometry*, Buletinul Institutului Politehnic din IASI, Tomul L, Fasc. 6A; (2008).

[3]. Ma Shi-Ning, s.a. – *Study on the friction and Wear Characteristics and Structure of Compound Layer from Combined Treatment of Ion Nitrocarburizing-Ion Sulphurizing of CrMoCu Alloy Cast Iron,* Transactions of materials and heat treatment proceedings of The 14-Th. IFHTSE Congress, Vol.25, N0.5, Shanghai, China, (2004).

[4]. Papadatu, C.P. - *Cercetări privind ameliorarea proprietăţilor şi creşterea fiabilităţii unor oţeluri folosite în construcţia utilajelor metalurgice*, PhD Thesis, University "Dunarea de Jos" of Galati, (2005).

[5]. Preda, A., Levcovici, S., Papadatu, C.- *Research works regarding the influence of the nitrided layer structural properties on the wear behaviour of the turbo-blowers pinions and gear wheels*, ROTRIB 2003, Galati.

[6]. Crudu, I., Palaghian, L., Gheorghies, C. - *Structural modifications in the superficial layer of metallic material in wear and fatigue process*, Japan International Tribology Conference, Nagoya; (1990).

[7]. Popescu, N. et al. - *Tratamente termice neconvenţionale,* Ed. Tehnica, Bucureşti, (1990).

[8]. Bursuc I., Gheorghies C. - *Influence of the internal stresses on the physico-mechanical properties of metal*, *Analele Stiintifice ale Universitatii Al .I. Cuza din Iasi*, Fizica Solidelor, Tomul XXXVIII-XXXIX, 1992-1993.

[9]. Crudu I., Gheorghies C. - *Incercarea materialelor*, Editura Tehnică, Bucuresti; (1986).

[10]. Crudu I. et al., , "Structural modification in the superficial layer of the material in wear and fatigue processes", Nagoya, Japan. (1990).
[11]. Gheorghieş C., Crudu I. - *A Cybernetic Structural Model Applied to the Study of Friction Process*, NORDTRIB 2000, Porvoo, Finland. (2000).
[12]. Gheorghies C. - *Modificari structurale in procese de uzura si oboseala*, Editura Tehnica, Bucuresti. (1999).
[13]. Gheorghieş C. - *Metode fizice de control nedistructiv*, Editura Porto-Franco, Galati. (1999).
[14]. Bucşă M., Crudu I., Gheorghies C. - *Experimental study of the failure processes within some metallic and ceramic coatings*, Thesaloniki, Greece; (1999).
[15]. **Papadatu, C.-P**., **Bordei, M. -** *Changes in Tribological Behaviour of Thermo-Chemical Treated Steels after Thermo-Magnetic Treatments*, Metalurgia International Revue, vol. XV, Special Issue no. 8, ISSN 1582-2214 , pag..41 – 49. (2010).

MANUSCRISELE, CARŢILE ŞI REVISTELE PENTRU SCHIMB, PRECUM SI ORICE CORESPONDENTE SE VOR TRIMITE PE ADRESA:

MANUSCRIPTS, REVIEWS AND BOOKS FOR EXCHANGE COOPERATION, AS WELL AS ANY CORRESPONDANCE WILL BE MAILED TO:

LES MANUSCRIPTS, LES REVUES ET LES LIVRES POUR L'ECHANGE, TOUT AUSSI QUE LA CORRESPONDANCE SERONT ENVOYES A L'ADRESSE:

MANUSCKRIPTEN, ZIETSCHRITFTEN UND BUCHER FUR AUSTAUCH SOWIE DIE KORRESPONDENZ SID AN FOLGENDE ANSCHRIFT ZU SEDEN:

After the latest evaluation of the journals achieved by National Center for the Science and Scientometry Politics (**CENAPOSS**), as recognition of its quality and impact at national level, the journal is included in B^+ category, 215 code (http://www.cncsis.ro/2006_evaluare_rev.php).

The journal is indexed in:
CSA: http://www.csa.com/ids70/serials_source_list.php?db=mechtrans-set-c
EBSCO: http://www.ebscohost.com/titleLists/a9h-journals.pdf
Copernicus: http://journals.indexcopernicus.com/karta.php

The papers published in this journal can be visualized on the "Dunarea de Jos" University of Galati site, the Faculty of Metallurgy, Material Science and Environment, page: www.fimm.ugal.ro.

Publisher's Name and Address:
Contact person: Antoaneta Căpraru
Galati University Press - GUP
47 Domneasca St., 800008 - Galati, Romania
Phone:+40 336 130139, Fax: +40 236 461353
Email: gup@ugal.ro

Editor's Name and Address:
Prof. Dr. Eng. Marian BORDEI
Dunarea de Jos University of Galati, Faculty of Metallurgy, Materials Science and Environment
111 Domneasca St., 800201 - Galati, Romania
Phone: +40 336 130223, Phone/Fax: +40 236 460750
Email: mbordei@ugal.ro

AFFILIATED WITH:

- *ROMANIAN SOCIETY FOR METALLURGY*
- *ROMANIAN SOCIETY FOR CHEMISTRY*
- *ROMANIAN SOCIETY FOR BIOMATERIALS*
- *ROMANIAN TECHNICAL FOUNDRY SOCIETY*
- *THE MATERIALS INFORMATION SOCIETY (ASM INTERNATIONAL)*

Annual subscription (4 issues per year)

Edited under the care of
Faculty of
METALLURGY, MATERIALS SCIENCE AND ENVIRONMENT
and
Center for Nanostructures and Functional Materials (CNMF)

Edited date: 30.12.2012
Issues number: 200
Printed by
Galati University Press
accredited CNCSIS
47 Domnească Street, 800036
Galati, Romania